Automation of pedicle screw placement by coupling distal bone bio-impedance measurements and robotics

Jimmy Da Silva

To cite this version:

Jimmy Da Silva. Automation of pedicle screw placement by coupling distal bone bio-impedance measurements and robotics. Robotics [cs.RO]. Sorbonne Université, 2022. English. NNT : 2022SORUS313 . tel-03900424

HAL Id: tel-03900424
https://theses.hal.science/tel-03900424

Submitted on 15 Dec 2022

THÈSE

présentée à

SORBONNE UNIVERSITÉ

par

Jimmy DA SILVA

pour obtenir le grade de

DOCTEUR
Spécialité: ***ROBOTIQUE***

Automation of pedicle screw placement by coupling distal bone bio-impedance measurements and robotics

---

Soutenue publiquement le 9 Septembre 2022 devant le jury composé de:

Quentin GRIMAL	Professeur à Sorbonne Université	*Président du jury*
Philippe FRAISSE	Professeur à l'Université de Montpellier	*Rapporteur*
Gérard POISSON	Professeur à l'Université d'Orléans	*Rapporteur*
Vincent PADOIS	Directeur de recherche à l'INRIA Bordeaux	*Examinateur*
Emmanuel VANDER POORTEN	Maître de Conférence à KU Leuven	*Examinateur*
Raphaël VIALLE	Professeur et chirurgien orthopédique à l'hôpital Trousseau	*Examinateur*
Thibault CHANDANSON	Responsable R&D, SpineGuard	*Invité*
Guillaume MOREL	Professeur à Sorbonne Université	*Directeur de thèse*

Institut des Systèmes Intelligents et de Robotique (ISIR)
Pyramide Tour 55, 4 place Jussieu
UMR CNRS 7222, Paris, France

Résumé

Les récentes avancées en matière de robotique médicale ont permis de voir l'émergence de robots dans les blocs opératoires pour aider les chirurgiens à accomplir des tâches de plus en plus complexes. En particulier, des systèmes robotisés développés pour la chirurgie du rachis permettent de placer automatiquement un guide de perçage au-dessus du patient (à l'aide de scanners pré et/ou peropératoire). Cependant, la tâche de perçage de la colonne vertébrale (via les pédicules), nécessaire pour la pose d'implants, est délicate et encore aujourd'hui réalisée par le chirurgien. Cette tâche n'est pas encore robotisée car le robot n'a possibilité de valider en temps réel que l'instrument est correctement positionné par rapport à la vertèbre.

Les travaux présentés dans cette thèse cherche à investiguer la possibilité d'augmenter le niveau d'automatisation de la pose de vis pédiculaires en intégrant des moyens de mesure adaptés. Plus précisément, nous avons utilisé la mesure d'impédance électrique des tissus osseux pour développer un algorithme de détection de brèche osseuse. Ce dernier permet d'arrêter immédiatement le perçage à l'approche de la moelle épinière ou d'autre tissus mous.

Puisque la tâche de perçage nécessite l'application d'une force sur le corps du patient qui est déformable, nous avons aussi travaillé sur des algorithmes de contrôle-commande. Un contrôleur en force a été développé dans le but de suivre automatiquement les déplacements du patient tout en réalisant la tâche de perçage. Un signal de pseudo-force, construit à partir des mesures de position du robot, a été utilisé dans la boucle de rétroaction pour réguler de façon robuste la force d'interaction appliquée à l'os par le contrôleur en impédance présent dans le robot.

Une étude de stabilité, des simulations, ainsi que des résultats expérimentaux ont montré la supériorité de notre approche en terme de stabilité aux incertitudes liés à l'environnement, par rapport aux méthodes conventionnelles utilisant un capteur d'effort.

Des expériences de perçage ont été réalisées ex-vivo sur des vertèbres d'agneaux pour étalonner nos algorithmes. Suite à une étude quantitative réalisée sur ces vertèbres ex-vivo, la méthode a aussi été validée in-vivo lors d'une expérience sur cochon vivant. Les résultats obtenus démontrent que le contrôleur ainsi que l'algorithme de détection de brèche pourrait permettre d'améliorer la sécurité des opérations du rachis assistés par robot.

Mots clés: Robotique chirurgicale, Chirurgie rachidienne, Impédance électrique, Commande en force.

Abstract

In recent years, advancements in medical robotics have led to the emergence of robots in the operating room to assist surgeons in performing complex surgical tasks. In particular, robots used for robotic-assisted spine surgery are currently employed to position physical guides thanks to pre-operative planning and per-operative image-based registration. However, the risky task of drilling the pedicles to insert screw implants is still left entirely to the surgeon alone. One of the main reasons is that there is no way for the robot to validate, through a direct real-time measure, the correct positioning of the instrument tip with respect to the bone.

In this context, the work of this thesis investigates the possibility of pushing further the robotic assistance in spine surgery, towards automatic gesture execution, by integrating adequate sensory feedback. More specifically, we consider the measurements of the bony tissue bio-electrical impedance during drilling. The focus has been put on developing an algorithm able to detect a bone breach to immediately stop the robot and prevent damaging the spine or any other surrounding soft tissues.

Since bone drilling during spine surgery is a task that involves force application on a moving rigid body, we also worked on force control. A force controller has been developed to track the patient's motion while performing the drilling automatically. A pseudo-force signal, built from the position measurements, was used as feedback above an inner impedance controller to regulate robustly the interaction force applied to the bone. A stability analysis, simulations, and experimental results show improved experimental robustness to environment dynamics uncertainties, as compared to conventional sensor-based force feedback.

Bone drilling experiments have been performed *ex-vivo* on lamb vertebrae to test and tune the algorithms. In addition to a successful quantitative *ex-vivo* study, the approach was also validated *in-vivo* on a pig model. The obtained results demonstrated that the developed controller and bone breach detection offer plausible perspectives to improve safety in robotically-assisted spine surgery.

Keywords: Surgical Robotics, Spine Surgery, Electrical Impedance, Force Control.

Remerciements

La thèse présentée dans ce document n'aurait sans doute pas aboutit à de tels résultats si je n'avais pas été si bien entouré, à la fois au travail par mes collègues, mais aussi par mes amis et ma famille. Les quelques mots qui suivent sont dédiés à tous ceux qui m'ont soutenu pendant ces trois années de thèse.

Tout d'abord je tiens à remercier mes deux encadrants, Guillaume et Thibault. Merci Guillaume de m'avoir convaincu de faire cette thèse avec toi (pourtant après deux ans de travail avec moi, tu savais que j'allais finir par te casser les pieds...). Tu m'as un peu menti à ce moment-là en me disant que ça serait du gâteau, mais finalement tu as bien fait! J'ai appris énormément à tes côtés et tu as toujours su trouver du temps pour moi dans les moments critiques, malgré ton agenda de ministre. Thibault, merci de m'avoir pousser à faire toujours plus et à tenter l'impossible. Je n'aurais jamais pu aboutir à de tels résultats sans ta motivation, ton positivisme et ton envie de tout essayer.

Je tiens à remercier chaleureusement l'ensemble de mon jury de soutenance, qui, grâce à nos échanges m'a permis de me rendre compte de l'impact concret de mes travaux de thèse, et de tout ce que nous pourrions encore accomplir. Vous avez fait de la soutenance, que j'appréhendais énormément, un moment appréciable, intellectuellement riche et constructif.

Merci à toute l'équipe de SpineGuard qui m'a accueilli à bras ouverts. Ces quelques jours par semaine dans vos locaux étaient toujours remplis d'entrain et de joie de vivre. Comme par hasard, à chaque fois que je venais il y avait toujours une bonne raison pour se faire une bouffe. Même si certaines sources douteuses disaient plutôt que c'est la nourriture qui m'appâtait. Vous avez appris de moi, mais j'ai surtout appris de vous. Nos réunions en interne, les conférences, les meetings avec des chirurgiens expert du domaine, m'ont fait monter en compétence et ont transformé cette thèse en une application concrète et motivante, et, en somme, en une très bonne première expérience de la vie en entreprise.

Je dois dire maintenant au revoir et merci à l'ISIR qui m'a accueilli pendant ces 7 belles années. Tout d'abord merci aux membres des équipes administrative et technique qui portent (ou ont porté) le laboratoire au quotidien : Michèle, Awatef, Sylvie, Yves, Adela, Anne-Claire, Ludovic, Florian, David, Philppe, Lolo, Loïc, Younes. Sans votre support, commandes à la dernière minute, conseils, et j'en passe, la vie au laboratoire ne serait pas la même.

Merci à l'équipe SYROCO (Vincent, Frédo, Faïz, Antoine, Lucas, Ryan, Philipp, Alex, ...) qui m'a accueillie fraîchement sorti d'école d'ingé et accompagnée par la

suite malgré mon changement d'équipe. Plus particulièrement, merci Vincent pour ta pédagogie, ton franc-parler et ton humanité qui m'ont donné goût à la recherche.

Et bien sûr, il m'est impossible d'oublier la géniale équipe AGATHE. Equipe qui m'a séduite avec un premier projet médical, pour ensuite me proposer une thèse. Merci à tous ses permanents (Guillaume, Nath, Emmanuel, Fabien, Ludo, Wael, Jérôme, Brahim, MAV) et à tous ses doctorants et ingés croisés sur la route : Lilyan, Guillaume, Madhi, Océane, Charlélie, Félix, Etienne, Charlotte, Mathilde, Alexis, Omar, Delphine, Mario, Rémi, Angélina, Ninon, Solène x2, Lucas x2, Thomas x2. Tant de personnalités, tant de belles personnes, qui ont fait que j'étais content de me lever le matin malgré les galères de la thèse. Je vous dis merci, et à très vite, car je sais que nous nous reverrons.

Un immense merci à tous les membres du projet FAROS et plus particulièrement à mes collègues de l'extrême qui m'ont énormément aidé lors des expériences sur animal: Antoine, Elie, Saman, Célia. Ces héros de l'ombre sont souvent trop peu félicité mais pourtant cruciaux dans des travaux de thèse.

Last but not the least..., gros cœur avec les doigts à mes amis du J05 (Jésus, Mégane, Clémence, Josh, Ousmane, Eléonore) qui ont essuyé mes pleurs dans les moments les plus difficiles.

Il est important de pouvoir compter sur ses collègues, mais aussi sur ses amis. Et encore une fois j'ai été gâté. Entre les copains des Mines, de Gatech, des chorales (et oui je chante, et j'adore ça !), et tant d'autres encore que je ne saurais classer dans des groupes... On peut vraiment dire que j'étais très bien entouré pendant cette thèse. Pour être sûr de n'oublier personne je ne vous listerai pas tous ici, mais globalement tu te reconnaitras ici facilement: si tu as reçu un câlin de moi ses dernières années c'est que tu comptes beaucoup pour moi ! Sachez tous que je suis énormément reconnaissant de pouvoir partager des petits bouts de vie avec chacun d'entre vous. Et que maintenant que je suis enfin libre, je suis prêt à en profiter et vous rendre la pareille.

Finalement, je remercie de tout mon cœur ma famille pour son soutien inconditionnel pendant cette période compliquée, où je n'ai pas toujours été très présent, ou de bonne humeur... Merci, à mes parents, qui par leur amour et sacrifices m'ont porté toutes ces années ! C'est grâce à vous tous que j'en suis arrivé jusqu'ici, mais surtout que je suis fier d'être l'homme que je suis aujourd'hui.

Un immense MERCI à vous tous !

Contents

List of Figures

List of Tables

Chapter 1

Context & objectives

Over the past decades, there has been a significant interest in using robots for surgical applications. This thesis mainly focuses on robotic assistance for spine surgery.

The first robotic assistance for spine surgery started to be developed in the 1990s [Sautot et al., 1992]. Due to the high risks of operating close to the spinal cord, surgeons looked for intelligent systems to help them perform complex procedures with more precision and reliability. Among those, pedicle screw placement, which is the procedure of interest in this thesis, is used on various spine symptoms such as deformities (i.e., scoliosis), infections, or fractures.

Thanks to significant advancements in medical robotics [Troccaz, 2013], spine robots are now available on the market and provide assistance. However, as for many surgical applications, robotic functions are limited to positioning a tool with respect to the patient by means of pre-operative planning and per-operative registration. In that sense, clinically available robots are mostly viewed as peripherals for navigation systems and do not exploit any advanced robot control feature. This thesis aims to explore alternative robot control approaches to bring advanced functions and improved safety to the operating room (OR).

The following sections present the clinical background along with the main challenges related to spine surgery, the devices currently available on the market, and the proposed contributions to improving robotic-assisted pedicle screw placement.

1.1 Clinical context

1.1.1 Anatomy of the spine

The spinal column comprises a set of bones (vertebrae), discs, and ligaments. The human spine contains 32 to 34 vertebrae: seven cervical (C1 to C7), twelve thoracic (T1 to T12), five lumbar (L1 to L5), five forming the Sacrum, and three to five in the Coccyx (Figure 1.1). Flexible intervertebral discs separate each vertebra, mainly constituted of water and collagen, giving mobility to the entire spine.

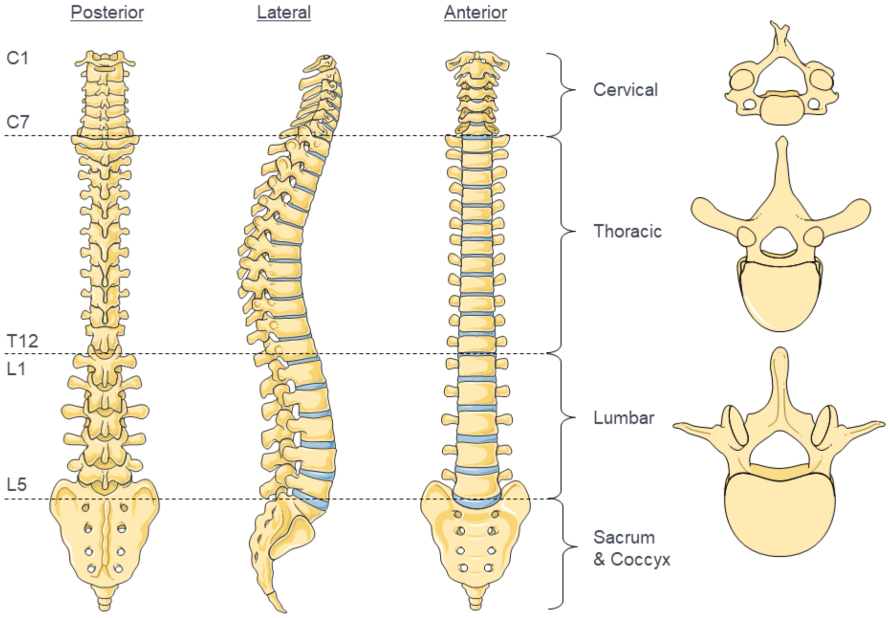

Figure 1.1: Anatomy of the spine. Vertebrae in yellow, disks in blue.
Illustration adapted from Servier Medical Art under CC attribution license 3.0.

The anatomy of the vertebrae varies in shape and size depending on the level (cervical, thoracic or lumbar). Still, all possess the same elemental parts: a vertebral body, two transverse processes, one spinous process separated by the laminas, and two pedicles (Figure 1.2). Together they shape the spinal canal protecting the spinal cord running from the head down to the Sacrum.

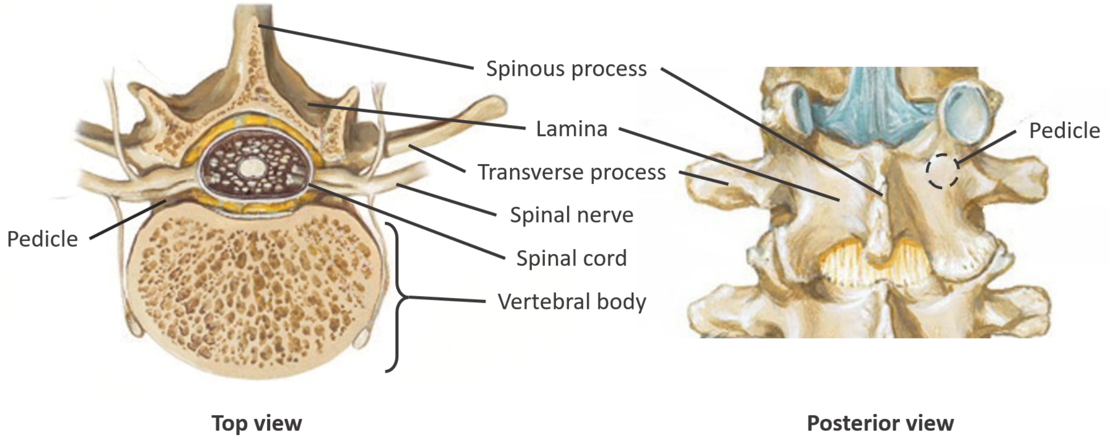

FIGURE 1.2: Anatomy of a lumbar vertebra.
Illustration adapted from [Thompson, 2010].

The bone structure itself is also variable inside a vertebra and evolves with time. The bone surface, called the cortical bone, is much more dense and strong than the spongious (or cancellous) bone. Figure 1.3 shows the difference between these two bone layers on a lumbar vertebra.

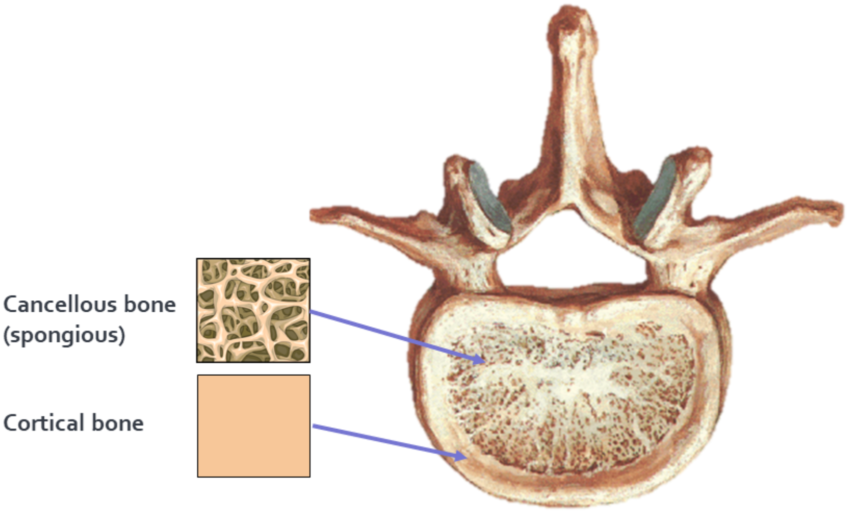

FIGURE 1.3: Cortical and spongious bone in a lumbar vertebra.
Illustration adapted from [Thompson, 2010].

1.1.2 Pedicle screw placement

Several procedures in spine surgery, *e.g.*, scoliosis correction, require inserting screws in vertebrae to immobilize two or more of them together with metallic rods. The *pedicles* are the strongest accessible parts of the vertebral arch via a posterior approach (from the back). These narrow spaces are used to insert so-called *pedicle screws*, as illustrated in Figure 1.4, with appropriate stability.

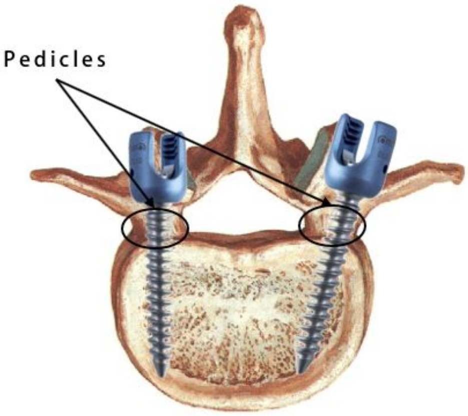

FIGURE 1.4: Top view of a lumbar vertebra with two pedicle screws inserted.

Depending on the patient's anatomy, the width of the pedicles varies from up to 18mm down to 3.5mm for thoracic and lumbar vertebrae [Lien et al., 2007]. The diameter of the screws inserted can be chosen with respect to the estimated pedicle width from pre-operative images. Surgeons tend to select the largest possible screw so that its threads can be fixed in the cortical layers of the pedicle. However, if chosen too large, they may damage the vertebra. The optimal diameter is around 80% of the available width according to [Solitro et al., 2019]. The screw length can also be customized to maximize the screw purchase for optimizing fixation [Karami et al., 2015].

Inserting screws in this tight spot of the bone is a major issue in spine surgery. Indeed, as shown in Figure 1.2, pedicles are in close proximity to critical anatomical regions (i.e., spinal cord and nerves), so misplaced screws can induce severe complications to the patient [Lonstein et al., 1999]. Meanwhile, estimating the correct position and orientation of the screw is quite challenging.

1.2 Non-assisted procedure

During the free-handed procedure, the surgeon drills a pre-hole before inserting the screw. This non-assisted medical procedure is made of three different tasks:

1. A bone awl (Figure 1.5), or a burr, is used to penetrate the outer cortical layer, resulting in a small hole called the entry point.

FIGURE 1.5: Bone awl.

2. A pedicle probe (Figure 1.6) is used to dig a path for the screw through the pedicle down to the outer cortical bone of the vertebral body.

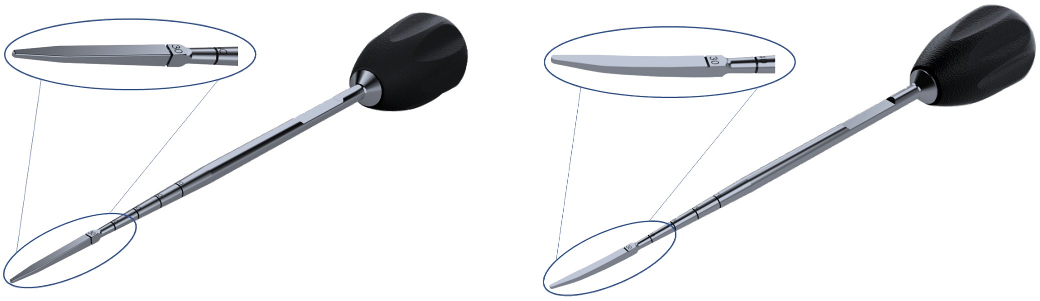

(A) Straight probe

(B) Curved probe

FIGURE 1.6: Available pedicle probe form factors.

3. The integrity of the path is checked with a ball-tip feeler (Figure 1.7) to make sure there are no bone breaches, either medial or lateral.

FIGURE 1.7: Ball-tip feeler (or tester).

The edges at the tip of the probe allow for cutting the bone via a back-and-forth rotating motion coupled with an axial thrust force. This, depending on the patient's anatomy, can require a significant amount of force. The curved version of the probe (Figure 1.6B) simplifies the path's redirection and leads to lesser medial breaches [Espejo, 2006; Pithwa and Venkatesh, 2014].

To better understand the surgical site, X-ray images of the patient are usually taken prior to the operation. Looking at the images, like the ones in Figure 1.8, the clinical staff can plan in advance the position, the diameter, and the length of the screws with respect to the patient's anatomy.

---

[1] `www.hss.edu/images/articles/eos-imaging-scoliosis-2d-anteroposterior-lateral-views-3d-anteroposterior-view.jpg`

Figure 1.8: EOS images of a patient with scoliosis: 2D anteroposterior (frontal) and lateral (outer side) X-ray views[1].

The major difficulty with the manual procedure is that the precise location of the tip of the instrument with respect to the pedicle is hard to estimate during the surgery. The pre-operative scan is only a one-time photograph of the patient and is usually taken in a standing or sitting position, whereas during surgery, patients are placed in the prone position (lying down, dorsal side up). Moreover, the spine being relatively deformable thanks to the articulations of the vertebral disks, this shot can differ from the reality of the operating theater. Visual estimation of the desired screw orientation is difficult because only a tiny part of the bone is visible (see Figure 1.9).

Figure 1.9: Posterior approach for a scoliosis correction shows only the upper parts of the whole vertebrae.

1.3 Intra-operative navigation and guidance

Free-handed positioning of pedicle screws can lead to low accuracy, and thus some misplaced pedicle screws. For instance, a 5-year study on 116 patients at the Skåne University Hospital in Sweden reported an average of 14% of misplaced screws for the conventional non-assisted pedicle screw placement in idiopathic scoliosis surgery [Abul-Kasim and Ohlin, 2011].

Several solutions emerged in the last few years to assist practicians with complex spine surgeries [Shweikeh et al., 2014; Khalsa et al., 2021]. The proposed solutions described hereafter can be classified into four different groups: imaging, navigation, robotic guidance, and tissue sensing systems.

1.3.1 Imaging systems

Intra-operative medical imaging systems can be used to evaluate a tool or a screw's position in the patient during surgery. Two modalities are available for clinicians, computed tomography (CT) or fluoroscopy. Both rely on X-ray radiations. Fluoroscopy gives a less precise picture than CT but can be retrieved in real-time. Those types of equipment come in the form of an O-arm or a C-arm, as shown in Figure 1.10, and can either provide 2D or 3D imaging. The O-arm systems appear to be more accurate for pedicle screw placement but require a longer preparation time and a higher radiation exposure than the C-arms [Liu et al., 2017; Feng et al., 2020; Sans Merce, M. et al., 2020]. This is due to the fact that the conventional C-arm systems mainly provide two-dimensional fluoroscopic images. In contrast, the O-arm technology can offer real-time three-dimensional surgical imaging.

(A) O-arm[2]

(B) C-arm[3]

Figure 1.10: Example of X-ray-based per-operative imaging systems.

Both imaging technologies (CT, fluoroscopy) use ionizing radiation to create images of the body. These radiations have enough energy to potentially cause damage to DNA and may elevate the risk of developing cancer. Reducing the patient's exposure to radiation is thus important as the dose can be quite significant during surgery, depending on the system used. The dose received by surgeons is also of great concern [Bratschitsch et al., 2019] as the cumulative radiation exposure of a spine surgeon during a working life can reach a dangerous value in the long run.

Some recent works on non-ionizing imaging technologies, such as ultrasound and magnetic resonance imaging (MRI), have great potential and could provide new X-ray-free approaches to spine surgery. For instance, deep-learning techniques applied to MRI images have shown to be able to generate synthetic CT images of the spine [Staartjes et al., 2021]. In spine surgery, ultrasound imaging is still most often employed as an aid for procedures involving injection or the introduction of needles [Ahmed et al., 2018]. Although its use for spine surgery has fallen out of favor, ultrasound could be helpful in several surgical scenarios [Vasudeva et al., 2017]. Recent works [Zhou et al., 2020; Li et al., 2021] tend to modernize its practice for a future robotic application of ultrasound for minimally-invasive spine interventions.

1.3.2 Navigation systems

To reduce the number of radiations used during surgery, imaging systems have been coupled to marker-based optical tracking devices to provide a real-time estimation of the tool position. These combined devices, commonly called navigation systems, can superpose the image of a virtual instrument on a pre-operative or intra-operative scan. This is done so that the surgeon can see a visual feedback of the instrument's position inside the patient on a screen, like shown in Figure 1.11, or now even in a Virtual or Augmented Reality (VR or AR) environment [Müller et al., 2020].

Most navigation systems rely on reflective marker clusters fixed on the tool and on a distinctive anatomical part of the patient's spine. The marker fiducials are then tracked with multiple infrared cameras. To minimize registration errors, the patient marker is usually placed on an adjacent vertebra to the currently drilled one. Moreover, many of the available systems provide a planning software enabling the surgeon to plan in advance the desired size, length, and position of the screws from pre-operative 3D images of the patient, as shown in Figure 1.12. However, frequent criticism arose from the surgical community against navigation platforms' cost and installation duration.

---

[2] `https://news.medtronic.com/O-Arm-2D-3D-Imaging-System`

[3] `https://www.gehealthcare.fr/products/interventional-image-guided-systems/igs-for-hybrid-or/discovery-igs-7`

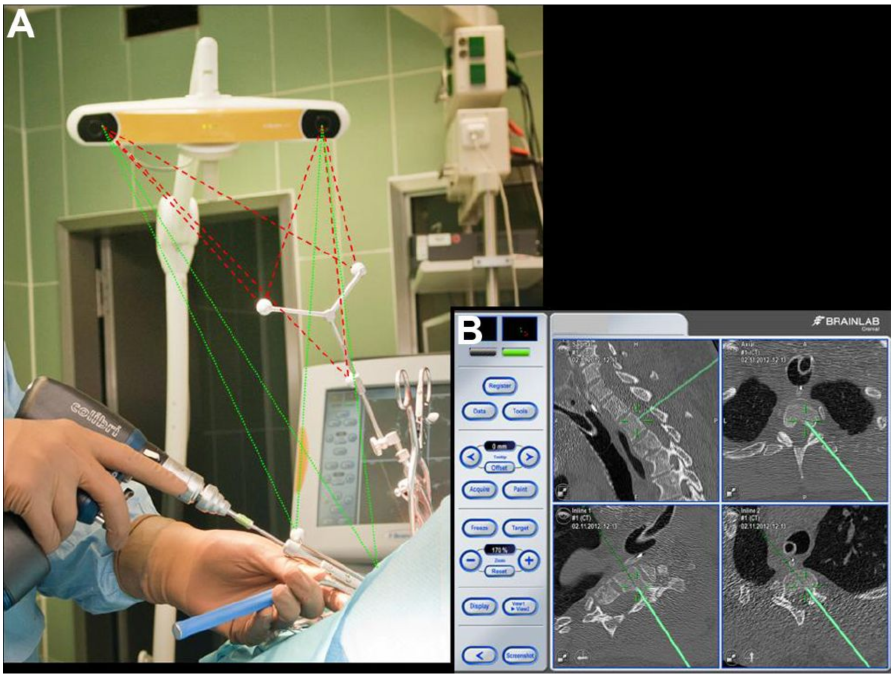

FIGURE 1.11: [Kantelhardt et al., 2014] Brainlab's Kolibri navigation system. (A) intraoperative setup, featuring a stereo camera, which simultaneously tracks the reference-marker array (red lines) and a registered drill guide (green lines). (B) The navigation-system screen displays the current position of a tracked instrument on sagittal, axial, and in-line view reconstructions of the pre-operative CT.

Indeed, their use is relatively recent since only 3.3% of spine surgeries were navigated in the United States in 2014 [Kelley et al., 2021]. With the technologies improving, computer-assisted navigation utilization is increasing, but further innovation is necessary to improve performance and cost-effectiveness [Rawicki et al., 2021].

Navigation systems can not yet display images acquired in real-time since the radiation dose would be too high. However, recent research studies show that live ultrasound guidance for spine surgery is under development [Zettinig et al., 2017].

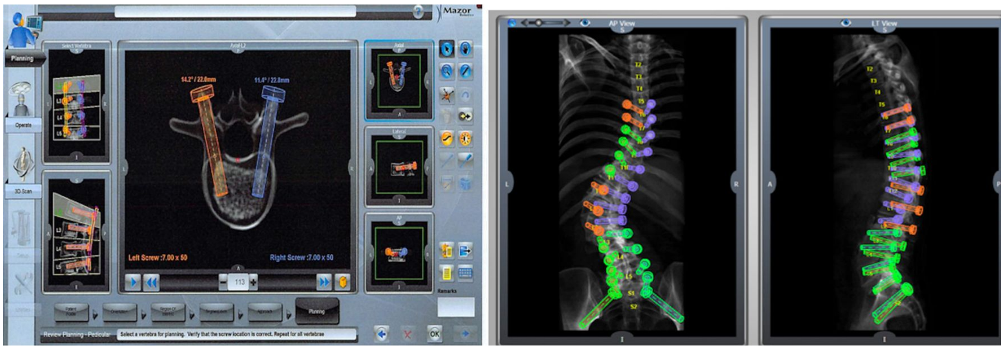

FIGURE 1.12: [Kochanski et al., 2019] Preoperative planning for screw trajectories based on preoperative CT scan.

1.3.3 Robotic guidance

Navigation systems have been associated with robotic arms to provide physical gesture guidance. The arm is only used in order to maintain a drill guide rigidly along the surgeon's preplanned trajectory, right above the patient (Figure 1.13). The surgeon then only has to drill through the guide without having to look for the entrypoint and orientation. Still, nothing controls the depth of insertion of the drilling. Although, the surgeon can get an estimation thanks to the navigation's system visual feedback.

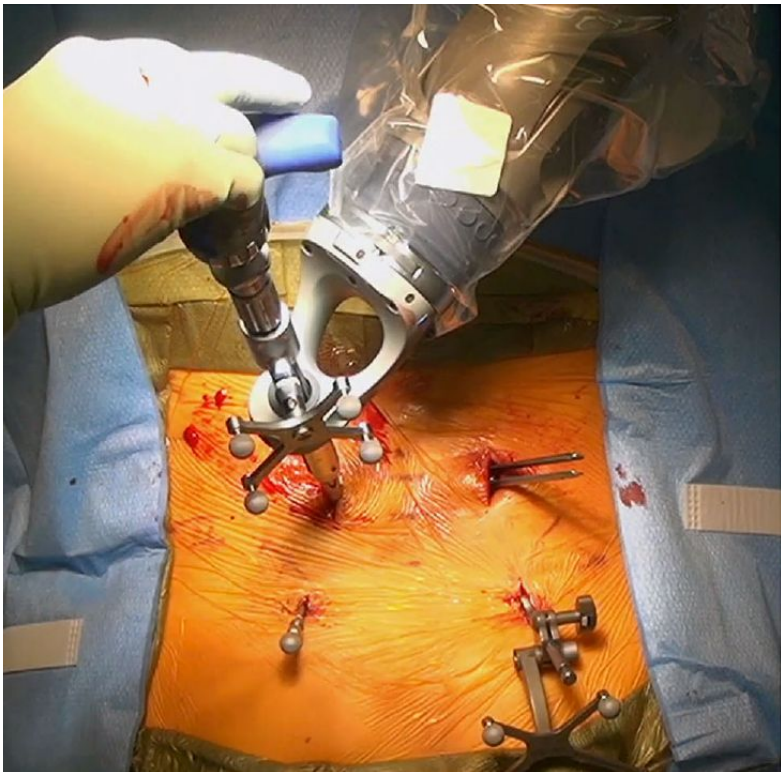

FIGURE 1.13: Robotically-assisted minimally invasive pedicle screw placement [Farber et al., 2021].

Many spine robots are available for clinical use, such as the Mazor X Stealth Edition[4], the ROSA ONE Spine from Zimmer Biomet[5], or the Cirq robot from Brainlab[6]. All these robots place a guide thanks to a navigation system. Additional features (patient tracking, intra-operative CT, rod-bending, etc.) vary from one system to the other. Overall, the goal of these robotic systems is to reduce human errors, operative time, and radiation exposure compared to when using a navigation system alone. Also, this allows the surgeon to focus on the drilling action. Using robotic systems offers several other

---

[4] `www.medtronic.com/us-en/healthcare-professionals/products/spinal-orthopaedic/spine-robotics/mazor-x-stealth-edition.html`

[5] `www.zimmerbiomet.lat/en/medical-professionals/robotic-solutions/rosa-spine.html`

[6] `www.brainlab.com/surgery-products/digital-spine-surgery/cirq-robotics-spinal/`

benefits, including eliminating hand tremors, reducing surgeon fatigue, and decreasing incision size thanks to minimally-invasive capabilities.

Unfortunately, even with rigid, powerful robots, errors may still happen since the surgeon cannot know for sure what is the real position of the tool inside the patient's vertebra. Here is a non-exhaustive list of issues that can lead to positioning errors:

- the patient model coming from the pre-operative scan differs from the real live model in the operating room since the spine is flexible.
- the registration between the scan and the patient markers contains errors
- the camera sensors have errors
- the markers calibration contains errors
- the patient's breathing during anesthesia can induce a motion of the spine up to 2mm for thoracic vertebrae [Liu et al., 2016].
- the markers on the tool or the patient can be occluded, leading to a wrong real-time visualization in the augmented images.

These errors can be accumulated and may quickly induce a screw tip positioning error of a few millimeters [Arico, 2020].

1.3.4 Local tissue sensing technologies

To consider the previously stated issues, many research laboratories and companies are working toward finding alternatives to X-ray-based guidance for orthopedic surgery. The research seen in the literature can be grouped into two different approaches.

The first approach consists in using non-radiative imaging modalities that could be used for real-time navigation in spine surgery, such as ultrasound ([Zhang et al., 2021]) or Optical Coherence Tomography (OCT) ([Zaffino et al., 2020]) to improve the live estimation of the tool's position with respect to the patient anatomy.

Another approach taken in this thesis consists in, rather than estimating a position, focusing on providing local real-time tissue characterization that can be used as information by the surgeon or the robot controlling the instrument. This utterly different methodology consists of trying to differentiate the type of tissue currently drilled by embedding sensors in spine surgery instruments. Then, this knowledge can be used for detecting and stopping errors happening during the procedure, like a bone breakthrough.

The first development of bone breakthrough detection for orthopedics surgery used the derivative of the thrust force to stop drillings on femurs [Allotta et al., 1996]. Automatic bone drilling is now an active research field with several contributions using a wide variety of signals, such as sound, electrical or mechanical impedance, or spectroscopy.

1.3.4.1 Mechanical impedance

The outer bone layer, also known as the cortical bone, is usually harder than the inner spongious bone. Thus, the mechanical energy required for drilling, or inserting a screw, increases when approaching the outer bone layers, and decreases when breaching out of a vertebra. Several state-of-the-art articles use an image of the mechanical bone impedance (or hardness) obtained from thrust force, cutting torque, or associated energy to distinguish between the different bone drilling states.

Thrust force

- While controlling the feed rate at 0.5 mm.s^{-1} with a 6-DoF robot, [Tian et al., 2014] used thresholding on the thrust force error to automatically stop pedicle drillings on sheep lumbar vertebrae. This required the use of a dedicated F/T sensor.
- [Accini et al., 2016] limited the thrust force thanks to an admittance-based control scheme and a force saturation. Although a significant drawback of the admittance approach is that the tool velocity increases outside the cortical walls, their controller succeeded in stopping on several animal ex-vivo drillings thanks to a simple threshold on the position error derivative.
- Using load cells, [Vadalà et al., 2020] estimated the mechanical impedance from force and speed measurements on human lumbar vertebrae experiments and compared its variations to those of the bone mineral density. Several limitations have been exposed. More perforations need to be performed in future studies, as well as stopping experiments.

Cutting torque & force

- [Sui et al., 2014] proposed a 3-phase model of the thrust force and cutting torque signal for bovine cortical bone drilling. Experiments show the validity of the model, but none exploit it for automatic breach detection.

- With data fusion, [Torun and Öztürk, 2020] proposed a successful machine-learning approach using KNN fed with motor (current, power) and robot (force, feed rate) signals to identify between 9 different bone drilling states (see Figure 1.14) with a 99% accuracy.

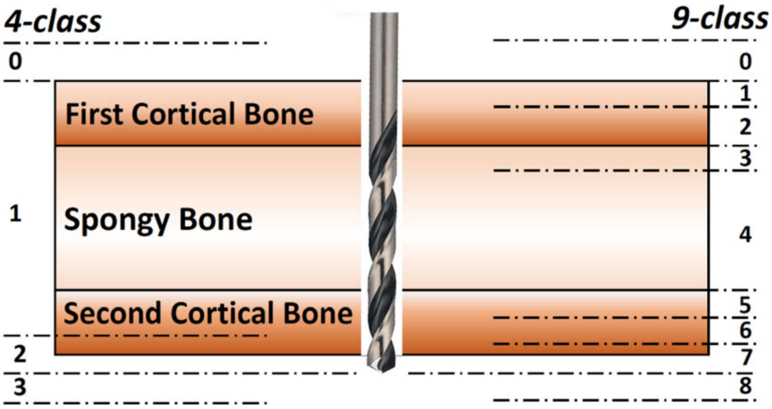

FIGURE 1.14: 4-class and 9-class drill bit state approaches [Torun and Öztürk, 2020].

- [Ho et al., 2018] proposed a novel removal energy density signal based on motor current, rotation speed, drill bit radius, and feed rate. This method has the advantage of taking into account the drilling parameters and thus simplifies the detection threshold tuning. However, no experiment using the energy to stop the drilling has been shown.

The recent studies using both force and torque sensing show good performance results. This indicates that it is a viable approach to be investigated for autonomous spine drilling. A drawback is that adding a force and torque sensor to a robot is quite expensive.

1.3.4.2 Contact and sound vibrations

Some research groups tackled tissue differentiation with airborne or contact vibration signals to detect bone density variations during drillings.

Sound

- [Sun et al., 2014] demonstrated that basic signal processing could discriminate cortical and cancellous bone tissue by analyzing the power spectral density. But the recognition rate presented is 88% for an experiment and 65% for another. Moreover, the sounds were not recorded in a real complex clinical environment.

- Another study ([Zakeri and Hodgson, 2017]) used short-time Fourier transform and SVM machine learning algorithms and showed a promising performance of 83%.
- In [Torun et al., 2018] is studied a novel method with feature extraction from power spectral density. The total time required to detect a breakthrough is around 0.6s but was not tested on real bone tissue.

Vibro-acoustic [Seibold et al., 2021] reported self-made shielded piezo contact microphones to be sufficiently sensitive to detect the cancellous, cortical bone drilling as well as the breakthrough event (transition from cortical to cancellous bone). Their proposed deep learning architecture used the acoustic signals captured on human cadaveric hip samples as an input for a ResNet18 network and showed a breakthrough detection sensitivity of 93.64%.

Several studies proposed to capture acoustic signals using different types of microphones or sound recorders. These works are pretty recent and promising but are not mature enough to be used in pedicle drilling yet. The main advantage of vibration sensing is that the sensors do not have to be inside the drill bit and are much cheaper than force or torque sensors. On the other hand, these methods have not been tested in real clinical environments yet, which are usually quite noisy because of the different machines used in the operating room. Similarly, many potential sources of vibrations and contacts could impact the system.

1.3.4.3 Diffuse reflectance spectroscopy (DRS)

Diffuse reflectance spectroscopy is a non-invasive technique used to study tissues' spectral characteristics. It consists in measuring the reflectance spectrum of light when it interacts with a medium.

In [Burström et al., 2019], Burstrom and Swamy inserted a fiber optic into a pedicle screwdriver to analyze the reflectance spectrum in cancellous, pre-cortical, and cortical, as well as after breach, in the wavelength range of 400-1600 nm. By classifying tissues by their percentage of fat, blood, and collagen for each bone phase, they managed to reliably identify the area of transition from cancellous to cortical with a sensitivity of 98-99% and a specificity of 98-99% on a 6-cadavers study. The method was also validated on a live porcine model [Swamy et al., 2020] with various probe-handling conditions.

The results of these works are promising as obtained on actual ex-vivo human and live porcine pedicle drillings. Nonetheless, a quantitative study showing automatic stops at the bone interface still needs to be performed. Also, it is not clear yet if this technology could be used in real-time in continuous drillings to prevent breaches.

1.3.4.4 Electrical bio-impedance (EBI)

Electrical bio-impedance, which is the signal of interest in this thesis, is the tissues' electrical resistivity, or the inverse of electrical conductivity. Osseous tissue can be considered an inhomogeneous and highly anisotropic material containing less conductive bone minerals and more conductive soft tissue such as blood vessels and other bodily fluids [Balmer et al., 2018]. The bone conductivity is thus mostly linked to the amount of blood present in the bone, which evolves relatively to its density/porosity. So cortical bone has a higher EBI than spongious bone, *i.e.,* a lower conductivity.

Pedicle probes embedding a bipolar conductivity sensor at their tip have been developed to provide local electrical conductivity measurements for spine surgery [Bolger et al., 2007]. The embedded sensor measures the electrical conductivity in the surrounding tissues thanks to two separate electrodes, allowing relative differentiation of tissue conductivity.

This technology is relatively mature in spine surgery as it has been available from SpineGuard[7] medical devices since 2003. Figure 1.15 shows the implementation of its bipolar sensor on a straight pedicle probe, the Pediguard® [Betz et al., 2010].

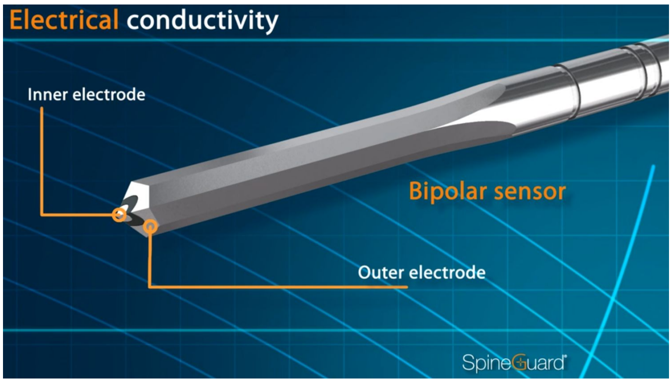

FIGURE 1.15: Electrical conductivity sensor inside a straight pedicle probe.

The electrical conductivity measurement is enabled here by an isolated inner electrode in the instrument's shaft [Bourlion and Vanquaethem, 2003]. When a tissue is in contact with both electrodes, a part of the current sent via the inner electrode is collected on the outer electrode. This current measurement is a direct image of bone conductivity.

---

[7] `www.spineguard.com`

The conductivity measurement is delivered to the surgeon via audio feedback. Like car parking sensors, the cadence and pitch of the audio signal increase when getting closer to dangerous anatomical parts, *e.g.*, soft tissues. In SpineGuard's most recent instrument, the *PediGuard DSG Connect*, presented in Figure 1.16, the signal is also transmitted wirelessly and displayed on a tablet. This enables to better visualize the conductivity variations during surgery.

FIGURE 1.16: The PediGuard DSG Connect.

SpineGuard's DSG® technology (for "Dynamic Surgical Guidance") is based on the principle that the electrical conductivity of tissue varies along the pedicle perforation. Indeed, as seen previously in Figure 1.3, the outer bone layer (cortical bone) is denser than the inner cancellous (spongious) bone. Figure 1.17 shows the expected signal variation with respect to the different anatomical parts encountered during a breaching pedicle preparation. When reaching the cortical outer bone layer, the conductivity should drop. Then, if the outer layer is broken and the tip approaches the outside of the bone, the conductivity will increase drastically because of the proximity to conductive tissues (blood, muscles, veins, etc.).

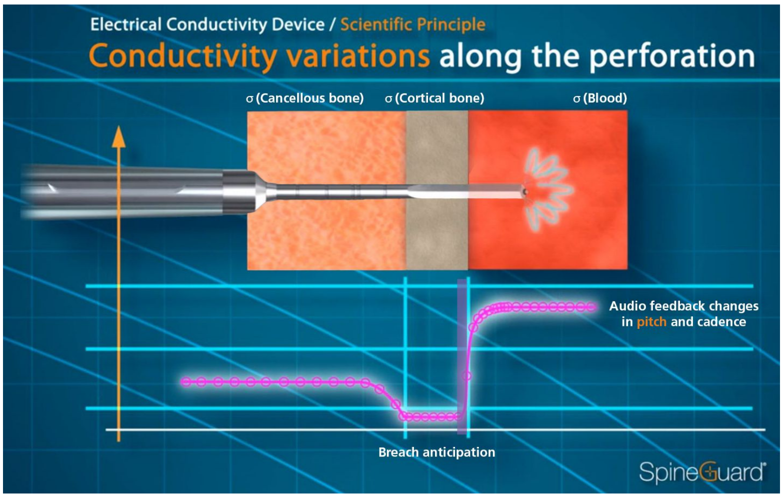

FIGURE 1.17: Electrical conductivity variations during a pedicle perforation leading to a bone breach.

When manipulating a pedicle preparation with a tool equipped with the DSG technology, a surgeon can distinguish between bone tissues and be alerted prior to an imminent cortical breach [Williams et al., 2014; Suess and Schomacher, 2016; Allaoui et al., 2018]. For instance, in a study on 8 patients diagnosed with a degenerative lumbar spine, using the PediGuard instrument has been proven to reduce the need for fluoroscopy use by 30% while maintaining a 97.5% accuracy [Chaput et al., 2013].

1.3.4.5 Overview

All the sensors mentioned above show promising results and a high potential for the automation of pedicle screw insertion. Some of them have even already been experimented on ex-vivo or in-vivo spine procedures and/or used on a robotic system. In many cases, simple signal thresholding was enough to distinguish between cancellous and cortical bone. In others, machine learning techniques were exploited for real-time tissue classification to predict bone breakthroughs.

The best result for each type of sensor has been reported in Table 1.1. The categories of sensors are compared in terms of sensitivity, real-time capabilities, and maturity – measured by the pertinence of the experimental model used in the study.

	Detection sensitivity	Real-time capability	Maturity (test model)
Mechanical impedance [Torun and Öztürk, 2020]	+ 99%	++ 100 Hz	– – sheep femur
Acoustics [Seibold et al., 2021]	– 94%	+ 10 Hz	– cadaver hip
Spectroscopy [Burström et al., 2019]	+ 98-99%	? not sure	+ cadaver spine
Electrical impedance [Bolger et al., 2007]	+ 98%	+ 5 Hz	++ human spine

TABLE 1.1: Comparison of the best local tissue sensing technologies found in the literature.

Recent studies using mechanical energy and spectroscopy show great sensitivity results. However, from all the modalities for local tissue sensing seen in the literature, EBI is the only one that is already used in real spine clinical procedures. Surgeons already use the audio feedback of SpineGuard's devices to gain additional information, but their sensor has never been used for automation prior to this research, which started in 2017.

A preliminary Proof Of Concept (POC) was first developed in 2017 by Florian Richer, leading to a first patent co-owned by SpineGuard & Sorbonne University [Bourlion et al., 2021].

A comparative study using several sensors on the same drillings would be interesting for comparing clearly the advantages of the different available modalities. Also, combining the signals into a multi-modal approach could prevent wrongful detections. Thanks to the newly FAROS European project (see details in Section 1.5.2), this should happen in the next two years.

1.4 Vision

Recent studies ([Kalidindi et al., 2020]) show that robots for spine surgery provide increased accuracy of pedicle screws and reduce radiation exposure. However, to date, clinically meaningful differences between traditional techniques and robot-assisted spine surgery have not been clearly demonstrated [Galetta et al., 2019]. One main concern of robotic surgery is the possible intra-operative discrepancy between pre-operative CT imaging and intraoperative registration. This error can arise from poor image quality, excessive amounts of soft tissue in the patient hindering proper robotic arm positioning, surgeon error during registration, or a combination of all the above [Tian et al., 2014].

Indeed, surgical plans are generally only an ideal sketch of the intraoperative reality and cannot account for all physiological movements (*i.e.*, physical deformation of tissues, heart pulsations, or respiratory movements), bleeding, and the like. Also, pre-operative images are reconstructed from the measurement of X-ray absorption and do not represent the anatomical truth. Therefore, pre-operative planning helps extract a rough global roadmap, but surgeons need to update it with the reality of the operating theater. Moreover, checking the internal tool position in the vertebra for security requires irradiative imaging systems (fluoroscopy or CT), creating long-term risks for the patient and the clinical staff.

Modern medical robotic approaches target absolute geometric precision, but in the context of surgery, functional accuracy, *i.e.,* relative to target anatomic and functional structures, is what matters. Surgeons do not let pure geometric objectives dictate their gestures; instead, they rely on their proprioception and exteroception, such as tactile feedback, even when using a navigation system. Rather than thinking of robots as tools used to rigidly and precisely position an instrument according to a plan, the vision of this thesis tends towards using robotics to enhance the senses and the gestures of the surgeon to help him/her do risky surgical tasks more securely. It is also the vision proposed in the FAROS European project (see Section 1.5.2). That way, we want to enable young surgeons using robotics to do what experienced surgeons already know how to do free-handedly. We believe that this radical mindset change is necessary to improve further the functional outcomes for spine surgery patients, which will later make partial automation of spine procedures possible.

This work focuses on developing an imageless autonomous robotic system thanks to electrical impedance measurements and advanced robot control. Instead of adjusting geometric relationships as indirect means of impacting the functional outcome, we want to leave the surgeon in control of the positioning and then provide assistance with the drilling gesture and security features. To that end, two main contributions are treated in this thesis and can be summarized as:

- A robust control system that can replace the free-hand bone drilling clinical gesture while enabling cooperation between the clinical staff and the robot.
- A X-ray-free real-time functional sensing system that can be used as a safety criterion for pedicle screw placement.

1.5 Context

The work presented in this document is the product of a collaboration between SpineGuard and Sorbonne University, thanks to the CIFRE Progam. This collaboration was extended to a larger consortium in 2021, through an H2020-EU funded collaborative project called FAROS.

1.5.1 The CIFRE program

The CIFRE (Conventions Industrielles de Formation par la REcherche) program allows French companies to entrust a doctoral candidate with an assignment in the framework of a research collaboration with an academic research laboratory affiliated with a doctoral school. This thesis was supervised both by the "Institut des Systèmes Intelligents et de Robotique" (ISIR) research lab and the SpineGuard company.

1.5.2 The FAROS European project

During the third year of the thesis (2021), SpineGuard and Sorbonne University teamed up with Balgrist University Hospital, King's College London, and KU Leuven to launch a European project called FAROS[8] for "Functionally Accurate RObotic Spine surgery". This project aims at improving functional accuracy through embedding physical intelligence in spine surgical robotics.

To do so, FAROS uses a multi-disciplinary approach by building up robotic controllers that will ensure practical, functional outcomes rather than pursuing geometrical goals based on imaging sensors. The consortium intends to efficiently embody surgeon-like autonomous behavior at different levels of granularity by exploring the use of several types of sensors. This new concept is applied to two spine surgery procedures (pedicle screw placement and endoscopic lumbar discectomy), with a platform embedding two robotic arms and a plurality of state-of-the-art sensors.

1.6 Structure of this dissertation

Chapter 2 presents the materials and methods that have been developed throughout the thesis to realize meaningful experiments on bone tissues.

Chapter 3 details the control method developed for providing an imageless robust drilling system. A developed force control outer loop takes advantage of an inner impedance controller to create robust mechanical interactions with the patient and cooperation with the clinical staff. The force control outer loop is done without force measurements; instead, an approximate interaction force induced by the mechanical behavior of impedance control is computed from the position measurements.

Chapter 4 exploits the DSG technology and SpineGuard's medical devices to create a safety feature for pedicle screw placement. A significant number of drillings have been performed to develop a breach detection algorithm, that was then validated on ex-vivo pieces and in an in-vivo setup to stop spine drillings autonomously.

Chapter 5 conludes this work by summarizing the contributions in their context objective. Then some research perspectives to extend the work presented in this manuscript are discussed.

---

[8] `https://h2020faros.eu/`

1.7 Related publications and patents

1.7.1 Publications

The preliminary automated breach detection experiments based on electrical conductivity were published and presented at the Hamlyn Symposium in 2019:

[Da Silva et al., 2019] *J. Da Silva, T. Chandanson, and G. Morel, "Robot-assisted spine surgery guided by conductivity sensing: first preclinical experiments demonstrate X-ray free breach detection," in The Hamlyn Symposium on Medical Robotics, 2019, pp. 75–76.* **Best Paper Award.**

The major results of the ex-vivo study presented in Chapter 4 have been presented (video available online[9]) to the medical community at the annual forum of the Society for Minimally Invasive Spine Surgery (SMISS) by the surgeon L. T. Khoo:

[Da Silva et al., 2021] *J. Da Silva, E. Saghbiny, T. Chandanson, S. Bette, M. Bourlion, R. Assaker, R. Betz, C. Bolger, H. Defino, A. Kaelin, L.T. Khoo, J.I. Williams, H.K. Wong, and G. Morel. "Using an electrical conductivity loop control system for automated breach prevention during robotic powered drilling of bone," In Annual Forum '21 Society for Minimally Invasive Spine Surgery, 2021.*,

and will be published at the Conference on New Technologies for Computer and Robot-Assisted Surgery (CRAS):

[Da Silva et al., 2022a] *J. Da Silva, E. Saghbiny, T. Chandanson, S. Bette, M. Bourlion and G. Morel. "Automatic bone breach detection for spine surgery based on bio-electrical conductivity sensing: Ex-vivo experimental validation," In 11th Conference on New Technologies for Computer and Robot-Assisted Surgery (CRAS), pages 86-87.*

The robust force control approach, described in Chapter 3 and used for the experimental autonomous drillings of Chapter 4, has been published at CRAS:

[Da Silva et al., 2022b] *J. Da Silva, S. Vafadar, T. Chandanson, and G. Morel, "Force control of the KUKA LBR Med without external force sensor." In 11th Conference on New Technologies for Computer and Robot-Assisted Surgery (CRAS), pages 88-89.*

A clinical study realized with real scoliosis patient data collected at the hospital Trousseau will be presented at CRAS 2022:

[Saghbiny et al., 2022] *E. Saghbiny, J. Da Silva, C. Chaimi, T. Chandanson, G. Morel, and R. Vialle. "Toward automatic bone breach detection for spine surgery using*

---

[9] `www.vumedi.com/video/using-an-electrical-conductivity-loop-control-system-for-automated-breach-prevention-during-robotic-/`

tissue bio-electrical conductivity sensing." In 11th Conference on New Technologies for Computer and Robot-Assisted Surgery (CRAS), pages 94-95.

1.7.2 Patent

A patent has been issued conjointly with SpineGuard, Sorbonne University, CNRS, and INSERM to protect the breach detection algorithms using electrical impedance presented in Chapter 4:

S. Bette, J. Da Silva, T. Chandanson, G.Morel and M. Bourlion (2021), "Dispositif médical de pénétration d'une structure anatomique et système médical comprenantun tel dispositif médical" (in French), FR Patent 2104761, May 5, 2021.

Chapter 2

A robotic system for autonomous bone drilling in the spine

This chapter details the hardware (robot, sensors, tools) used and the developments made to improve the robotic experimental setup throughout the thesis. The preliminary setup used for the first experiments (presented in Sections 4.1.3 and 4.2) is briefly presented in Appendix A.

2.1 Hardware

2.1.1 IIWA LBR Med 7

The robot used in this thesis is an LBR Med 7 R800 robotic arm manufactured by KUKA. This manipulator is the fifth iteration of the DLR robot [Albu-Schäffer et al., 2007], now known as the "IIWA" – for Intelligent Industrial Work Assistant. The specific "LBR Med" version, shown in Figure 2.1, is a version adapted to meet medical requirements and respect the international standards IEC 60601-1 and IEC 62304. It is sold as a robotic component that can easily be used for creating a medical device – meaning it cannot be used as is in the operating room by clinicians.

FIGURE 2.1: The KUKA LBR Med 7 R800[1]

This jointed-arm robot is classified as a "cobot," meaning it is intended for human-robot collaboration in a shared environment. The cooperation is made possible thanks to built-in joint torque sensors. They enable the detection of collisions and the implementation of powerful low-level torque control loops that can cancel joint friction.

Furthermore, this robot has the advantage of having 7 joints. This type of robot is called a "redundant" robotic manipulator. These arms have extra degrees of mobility from the 6 required DoFs to completely position and orient the end-effector in space. They allow internal movements while keeping a specific desired Cartesian pose (position and orientation) of the end-effector, like the motion depicted in Figure 2.2.

FIGURE 2.2: Null-space motion on the LBR Med robot.

The KUKA Sunrise cabinet hosts several internal controllers for the robot that already compensate for the gravity of the arm. In this work, we either use the Joint Impedance Controller (in Section 3.1.1) or the Cartesian Impedance Controller (in Section 3.1.2). An external computer running on a Linux-based real-time system communicates with the cabinet and its internal controller in real-time via the KUKA Fast Robot

---

[1] www.kuka.com/industries/health-care/kuka-medical-robotics/lbr-med

Interface (FRI). A homemade C++ program running at 1 kHz on the PC receives joint position and torque measurements and sends back joint position commands; But only measured positions are used for control purposes.

2.1.2 Robotic surgical tools with conductivity sensing

SpineGuard's medical instruments presented in Section 1.3.4.4 were designed initially to be handled manually by the surgeon. Therefore, they were not meant to be easily attached to a robot. In the context of this project, SpineGuard created several prototypes during the thesis that could be directly inserted into the drill chuck of the power drill. The two prototypes that were used during the experiments are presented below.

The first instrument tested was a classic drill bit of 3mm in diameter embedding a conductivity sensor. It is shown in Figure 2.3 along with the attached casing of the electronic card used to measure the electrical conductivity and send the signal wirelessly to the main computer at 5Hz. This tool was used during the first half of the thesis and then replaced by a second prototype with a threaded shaft.

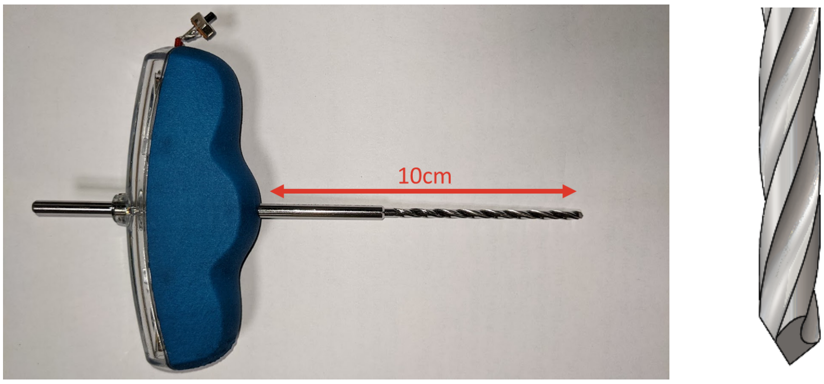

FIGURE 2.3: "Standard" robotic drill bit prototype.

The threads create a helical relationship between the bone and the drill bit. Thus, it converts the previous drilling task into a screwing task. The mechanical work is then function only of the screwing torque – as opposed to thrust force and cutting torque before. Similarly, controlling the rotation speed controls the insertion speed directly once the threads are engaged inside the bone.

Taking example from SpineGuard's tap instrument, this second prototype shown in Figure 2.4also has a pyramidal tip like the standard drill bit prototype for cutting purposes and a threaded shaft like a screw. Using this model, we also make sure that the drill is always in contact with the bone, meaning that the tool cannot be retracted unintentionally. The electronics on this model were also upgraded to get measurements at a higher frequency, *i.e.*, 25Hz.

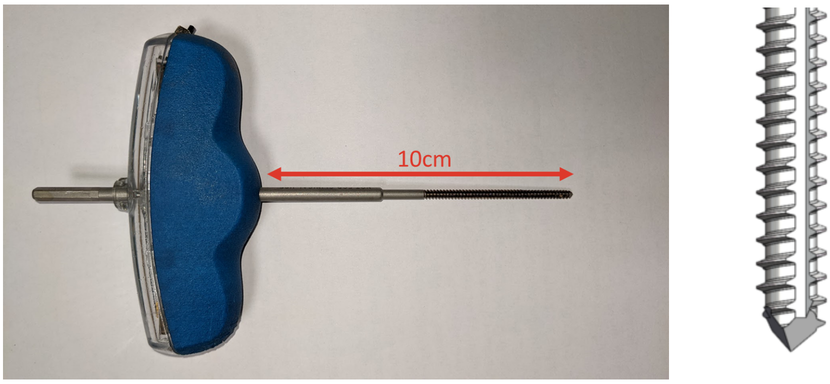

FIGURE 2.4: "Threaded" robotic drill bit prototype.

2.1.3 Power drill

The rotation of the 7th axis of the robot being too slow and limited in range, we had to add an infinite rotation joint to the robot to perform the drilling task. We chose a geared motor from Maxon with a 1.5 Nm nominal torque and a maximum speed of 922 rpm to be able to perform both drilling and screwing tasks. The motor is a brushless DC motor with built-in Hall sensors and encoders, which enables to get precise control of the drilling speed and also to estimate the cutting torque from the current measurements.

To rigidly fix the instrument with respect to the robot's flange, several parts have been manufactured by Laurent Fabre at the ISIR lab. Figure 2.5 shows the coupling part linking the motor's and the chuck's axes. The other parts (spacer and attachment piece), shown in Figure 2.6A, were made to position the power drill with a 30° angle with respect to the last robot axis while minimizing the distance between the tool's tip and the seventh joint. A roller bearing was placed between the spacer and the coupling to reduce the off-center from the axis of rotation. The motor and electronic components are protected

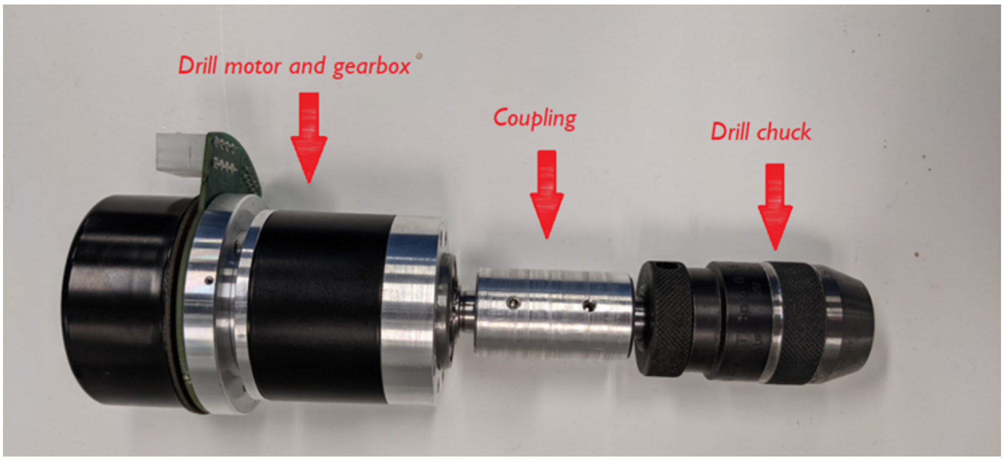

FIGURE 2.5: Assembly of the geared motor with the chuck

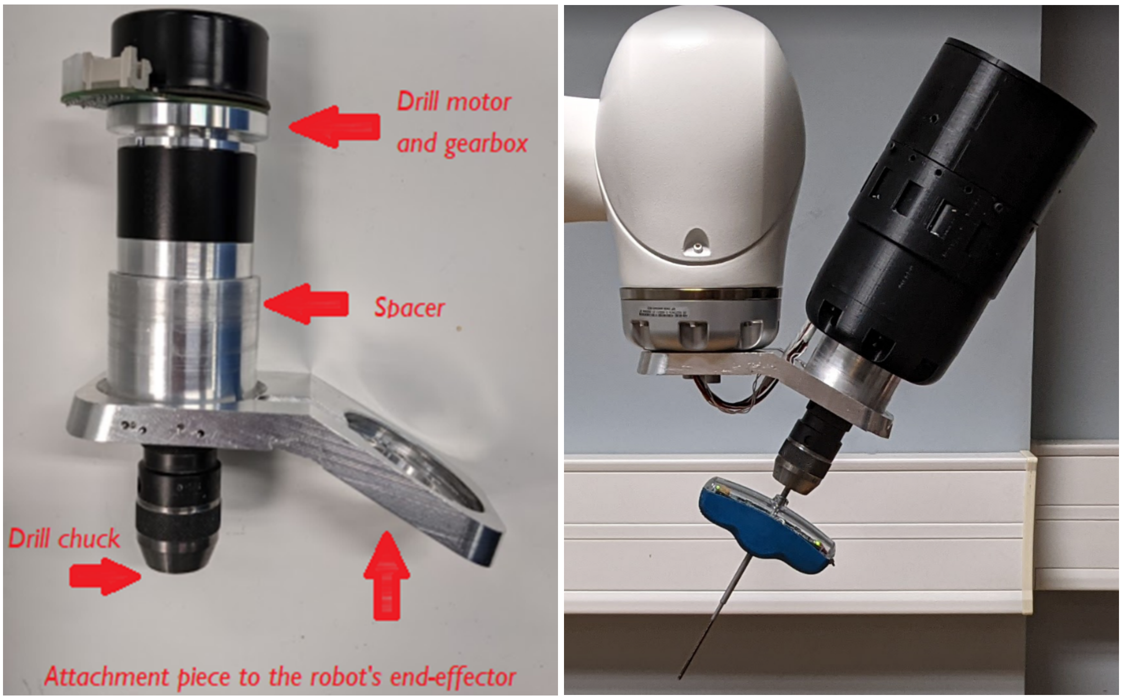

(A) Power drill fixation (B) Power drill mounted

FIGURE 2.6: Final version of the power drill conceived at the ISIR lab.

by a 3D-printed cover – black casing in Figure 2.6B. Sketches of the manufactured parts are provided in Appendix B.

The velocity control is performed by an EPOS4 Compact 50/5 controller from Maxon, which returns via USB the motor position, speed, and current to the main computer. The geared motor torque τ_{gm} is then estimated from the motor current i_m measurement with:

$$\tau_{gm} = k_{red} k_m i_m \ , \tag{2.1}$$

where k_{red} and k_m are the reduction and torque constants respectively.

The validity of this estimation has been assessed by Saman Vafadar and Antoine Harlé (as part of the FAROS project) using the experimental setup shown in Figure 2.7. A F/T sensor, ATI mini 40 (ATI Industrial Automation, USA), was rigidly fixed on the robot's table. A custom-designed 3D printed part was screwed to the F/T sensor. A wooden plate was inserted into a recess hollowed out in the plastic rapidly prototyped part. The threaded drill bit, mounted in the robot's drill, was placed on the wooden part while applying a constant force vertically. Then, the drilling was performed for different drilling speeds and vertical forces.

Figure 2.8 shows the results of the performed experiments with a 10 N vertically applied force with a 20 or 40 rpm rotation speed. As can be highlighted by these plots, as the threaded dill bit moves inside the wooden part, more threads become engaged,

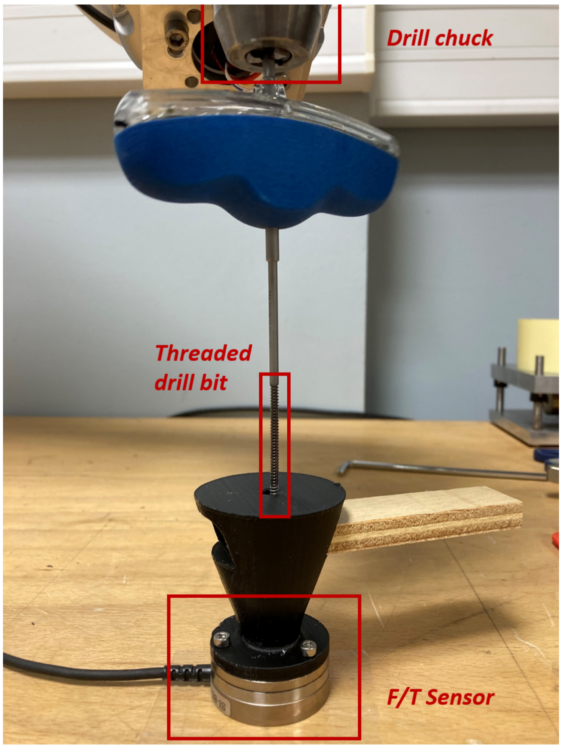

FIGURE 2.7: Experimental setup for the assessment of the drilling torque estimation. A 3D printed part fixed on an F/T sensor holds a wooden piece drilled with the threaded drill bit prototype.

frictional forces increase, and the drilling torque increases as well. The measured torque on the F/T sensor and the estimated torque from the drill's current follow the same trend. There is a mean constant bias of 31 mNm (for both experiments) between them. The 95% confidence intervals (2STD) are 22 mNm and 18 mNm, which corresponds to the amplitude of the noise on the estimated torque signal.

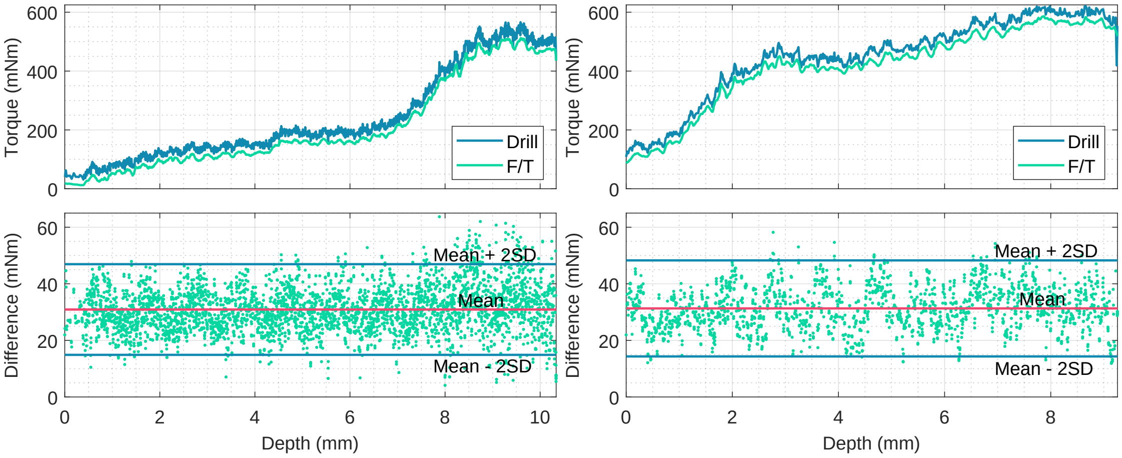

(A) 20 rpm (B) 40 rpm

FIGURE 2.8: Difference between the drill torque estimated from the drill's current and the measured torque from the F/T sensor at two different speeds.

2.2 Experimental environments used in the thesis

Reproducing the mechanical and electrical impedance of vertebrae simultaneously is not easy. Several spine anatomical phantoms exist with bio-realistic mechanical characteristics, but most cannot reproduce the bio-electrical conductivity of living tissues. Consequently, the breach detection algorithms presented in Chapter 4 had to be tested on real fresh bone material. To reduce as much as possible the number of animal sacrifices, an ex-vivo setup using butchery pieces has been developed. But, some experiments have also been run on living pigs with the control of veterinary surgeons to be in real operating room conditions.

2.2.1 Ex-vivo experiments

Vertebrae electrical and mechanical impedances are not constant during bone drilling. Also, the variability between each specimen, vertebrae, and bone segment is quite important and cannot be predicted. Hence, many drillings were required to verify the robustness to bone variability of the breach detection algorithm. In order to limit animal sacrifice, an ex-vivo setup was developed.

2.2.1.1 Lamb vertebrae

Many studies in literature compare the sizes and shapes of human vertebrae to other vertebrate species [F. McLain et al., 2002; Sheng et al., 2010]. When comparing animals to humans, the pig is one of the animals with the closest spinal system [Busscher et al., 2010], and so was chosen for the in-vivo experiments.

Unfortunately, complete porcine vertebrae were not available from the butcher's shop – mainly because they are cut in halves in slaughterhouses for sanitary reasons. Thus, the ex-vivo experiments were conducted on the second closest model to humans, sheep [Wilke et al., 1997; Mageed et al., 2013]. So, freshly bought lamb lumbar vertebrae (see Figure 2.9A) from the butcher shop were used as a substitute for living pigs.

2.2.1.2 Saline bath

To reproduce the electrical conductivity of the cerebrospinal fluid present in the vertebral canal during in-vivo experiments, the spinal cord was removed for ex-vivo trials, and the vertebral canal was submerged under saline water. The setup, shown in Figure 2.9B, consisting of a clamping device attached inside a hermetic and transparent box facilitated

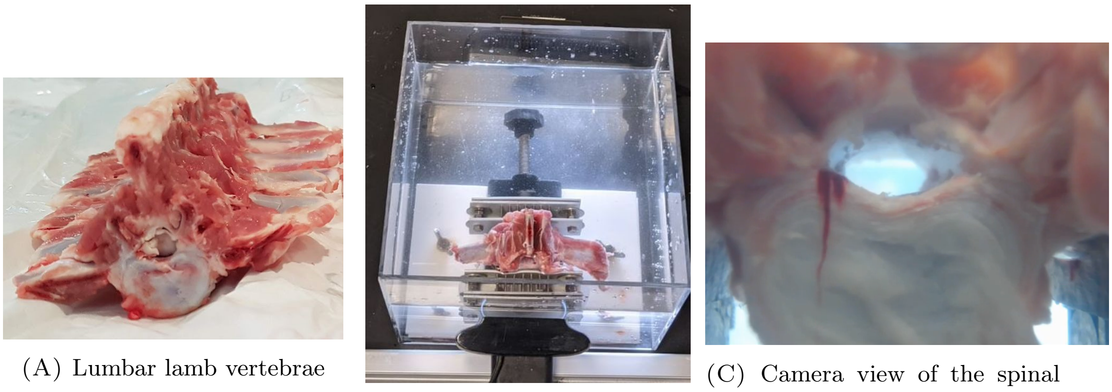

(A) Lumbar lamb vertebrae

(B) Homemade box with clamping device and camera

(C) Camera view of the spinal canal

Figure 2.9: Ex-vivo experimental model.

the repetition of experiments. Moreover, this allowed getting a direct visualization (e.g., Figure 2.9C) of what is happening inside the vertebral canal during a bone breach with a standard camera placed right outside the box.

2.2.1.3 Breathing simulator

To simulate the motion of the patient induced by the breathing process, a breathing simulator machine, shown in Figure 2.10A, was conceived in the ISIR lab to simulate a periodic displacement of a few millimeters. A camshaft mechanism imposes a translation motion from the rotation of an irregular cylinder with a δr eccentricity, as depicted in Figure 2.10B. The translation is then guided thanks to rods and bearings.

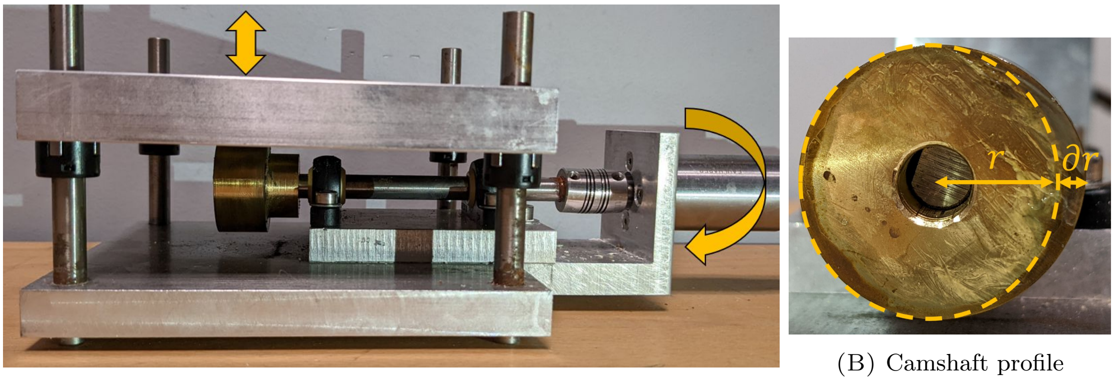

(A) Translation induced by the rotating cam

(B) Camshaft profile

Figure 2.10: Breathing simulator made from a motor, a camshaft, rods, and bearings.

This device was not only used for the ex-vivo experiments in Section 4.2, but also for some experiments evaluating the performance of the force controller in Section 3.4.4.2.

2.2.2 In-vivo experiments

To validate the usability and performance of our experimental system and algorithms in real operating conditions, some drillings have been performed on an *in-vivo* setup.

The animal experimentations were conducted under the supervision of veterinary surgeons at the National Veterinary school of Alfort (French: École Nationale Vétérinaire d'Alfort or ENVA) with the ethical approval of the French Ministry of Higher Education and Research. The official document is available in Appendix C.

The pigs were anesthetized during the whole operation. A breathing machine controlled the airflow insufflated into the subjects with a five-second period. The animals were placed in the supine position (horizontal with dorso up). The pigs' backs were opened to provide direct visibility and access to the lumbar and thoracic vertebrae, as shown in Figure 2.11.

FIGURE 2.11: Dorsal opening of a pig specimen.

After the experiments, the pigs were euthanized and cremated after the extraction of the operated spine segment for post-operative CT scanning.

2.2.3 Chosen drilling path

As seen in Section 1.1.2, the clinical relevant trajectory consists of drilling via the vertebral pedicles. Unfortunately, the young pigs used for the *in-vivo* experiments present growth cartilages in their vertebral bodies, contrary to humans. As can be seen on the CT scan in Figure 2.12, these growth cartilages are in the way of the pedicle path.

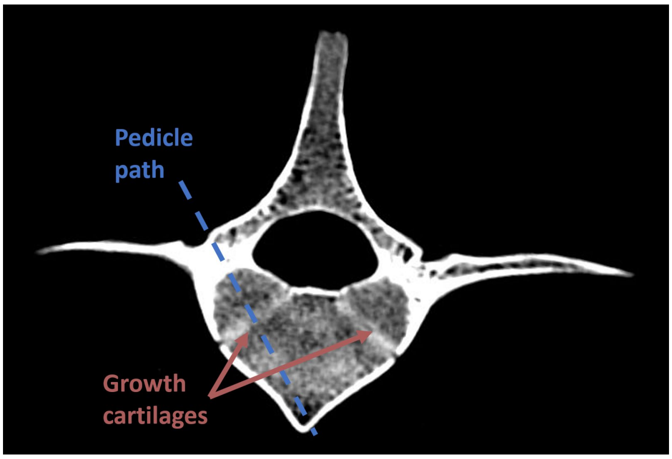

FIGURE 2.12: CT scan of a young pig showing two visible growth cartilages in the vertebral body.

This is not a problem mechanically speaking, but in the context of this thesis, it is. Indeed, these cartilages are highly conductive and can be misinterpreted with a breach in the spinal canal on the EBI signals.

To avoid misleading peaks in the conductivity signals, we chose to drill the spinous process instead. On top of avoiding growth cartilages, this path also ensures that we will be hitting the spinal canal at some point. The corresponding trajectory, shown in Figure 2.13, is also much more straightforward to visualize than the pedicle trajectory, as it is simply vertical and parallel to the spinous process itself and so more reproducible.

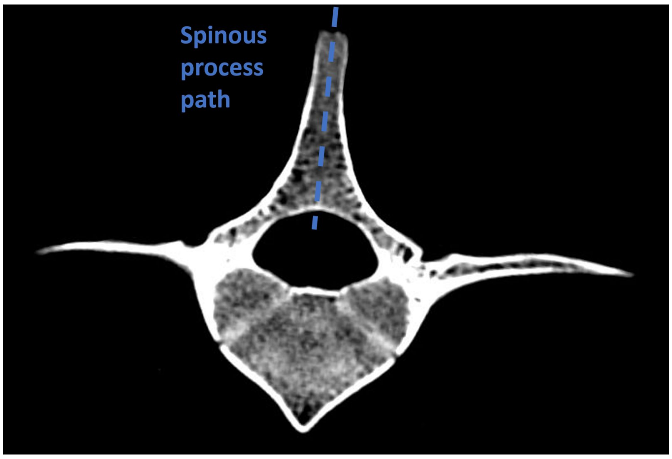

FIGURE 2.13: Considered drilling path for the thesis.

All the experiments presented in Chapter 4 correspond to drilling via the spinous process.

Chapter 3

Position and force control for safe cooperative bone drilling

Chapter 1 explained the interest of having a force controller to regulate the amount of pressure during vertebra drilling and to follow the patient's physiological movements. Due to the context of our application and the potential interactions between the robot and the clinical staff, the designed force controller needs to be robust to any perturbations.

In this Chapter is detailed a contribution to the Force Control field to propose a robust hybrid position and force control method that could be used for several medical robotics applications.

Force control is a field that has been studied a lot in the last decades [Siciliano and Khatib, 2008; Villani and De Schutter, 2016; Haddadin and Croft, 2016]. From a general perspective, controlling forces requires a trade-off between stability, bandwidth, accuracy, and robustness. To ensure stability, force control approaches often require a reasonable estimation of the environment's model (position and stiffness [Wijayarathne and Hammond, 2020]) to account for contact dynamics.

However, when dealing with patients, tracking their position can be practically uneasy, and knowing beforehand the stiffness of contact seems not feasible. Nonetheless, when using robotic assistance, like with any other tool, surgeons will expect 100% reliability, whatever its conditions of use. Consequently, interactions with any unknown environment must not destabilize the system to ensure the patient's and the clinical staff's safety, and be accepted in the OR.

The work presented in this chapter does not require any *a priori* knowledge of the environment –such as position or stiffness–, nor any online estimation of those parameters. Instead, the proposed method greatly relies on the inherent stability of impedance control and on the performance of a fast low-level torque controller, enabled thanks to internal torque sensors. Note that these two conditions are commonly available in most recent collaborative robots.

3.1 Impedance control

We will consider the robotic arm as a rigid manipulator; Thus, neglecting the joint flexibility between the motors and the links, which corresponds to an infinite joint stiffness hypothesis. The dynamics of the n-joint robotic arm can be written:

$$\boldsymbol{M}(\boldsymbol{q})\ddot{\boldsymbol{q}} + \boldsymbol{C}(\boldsymbol{q}, \dot{\boldsymbol{q}})\dot{\boldsymbol{q}} + \boldsymbol{g}(\boldsymbol{q}) = \boldsymbol{\tau}_a - \boldsymbol{\tau}_f - \boldsymbol{\tau}_e \tag{3.1}$$

where $\boldsymbol{q}, \dot{\boldsymbol{q}}, \ddot{\boldsymbol{q}} \in \mathbb{R}^n$ are the joint positions, velocities and accelerations, respectively, $\boldsymbol{M}(\boldsymbol{q}) \in \mathbb{R}^{n\times n}$ the joint inertia matrix, $\boldsymbol{C}(\boldsymbol{q}, \dot{\boldsymbol{q}}) \in \mathbb{R}^n$ the combined Coriolis/Centrifugal matrix and $\boldsymbol{g}(\boldsymbol{q}) \in \mathbb{R}^n$ the gravity torque. Vectors, $\boldsymbol{\tau}_a$, $\boldsymbol{\tau}_f$ and $\boldsymbol{\tau}_e \in \mathbb{R}^n$ represent respectively the joint torque produced by the actuator, the joint friction torque and the so-called *external* torques, resulting from mechanical action of the robot on external agents, such as a physical environment or a human operator, through contacts occurring either on the robot bodies or at the level of the end-effector.

The work presented here is based on the assumption that a low-level internal torque controller ensures the servoing of the torques applied to the robot's rigid bodies to the commanded torques, $\boldsymbol{\tau}_c$, thanks to the measured torques, $\boldsymbol{\tau}_m$, obtained from built-in torque sensors. It is also assumed that these torque sensors are placed at the very end of the power transmission of the robot's body links [Albu-Schäffer et al., 2007], in such a way that all the friction $\boldsymbol{\tau}_f$ can be compensated with an integrator placed in the torque error compensator. In other words,

$$\boldsymbol{\tau}_m = \boldsymbol{\tau}_a - \boldsymbol{\tau}_f \ . \tag{3.2}$$

Further, neglecting the response time of the torque loop, we can write $\boldsymbol{\tau}_m \approx \boldsymbol{\tau}_c$, which in turns leads to $\boldsymbol{\tau}_c \approx \boldsymbol{\tau}_a - \boldsymbol{\tau}_f$, and to the simplification of the robot's model Equation (3.1) to:

$$\boldsymbol{M}(\boldsymbol{q})\ddot{\boldsymbol{q}} + \boldsymbol{C}(\boldsymbol{q}, \dot{\boldsymbol{q}})\dot{\boldsymbol{q}} + \boldsymbol{g}(\boldsymbol{q}) = \boldsymbol{\tau}_c - \boldsymbol{\tau}_e \ . \tag{3.3}$$

Impedance control is a widely used approach to enable safe interactions for human-robot cooperative tasks. Its goal is to realize the same dynamical relationship as a mass-spring-damper system with desired inertia, stiffness, and damping. A high impedance assimilates the system to a stiff spring, meaning errors *w.r.t* the target position will generate strong forces to correct the deviation. In comparison, low impedances allow for more significant position errors before inducing heavy forces.

This control method is now implemented internally on most recent collaborative robots, such as the LBR Med used in this project (presented in Section 2.1.1). This principle, first introduced by Hogan in [Hogan, 1984], can either be implemented in the articular or the operational space.

The exact implementation of the impedance controllers provided by the KUKA control cabinet is unknown. Thereafter, we will assume that the control laws used internally are the ones presented in this section.

3.1.1 Joint Impedance control

The implementation to the articular space is rather straightforward, but does require good estimations of the dynamical model of the robot. Joint impedance control is implemented via the joint torques $\boldsymbol{\tau}_d$ on top of the internal torque loop as follows:

$$\boldsymbol{\tau}_c = \boldsymbol{\tau}_e + \hat{\boldsymbol{M}}\boldsymbol{M}_d^{-1}(\boldsymbol{K}_{qd}(\boldsymbol{q}_d - \boldsymbol{q}) + \boldsymbol{B}_{qd}(\dot{\boldsymbol{q}}_d - \dot{\boldsymbol{q}}) - \boldsymbol{\tau}_e) + \hat{\boldsymbol{C}}\dot{\boldsymbol{q}} + \hat{\boldsymbol{g}} \ , \tag{3.4}$$

where $\hat{\boldsymbol{M}}$, $\hat{\boldsymbol{C}}$, $\hat{\boldsymbol{g}}$ are estimates of the robot dynamical matrices and gravity torques, and $\boldsymbol{K}_{qd}$, $\boldsymbol{B}_{qd}$, $\boldsymbol{M}_d$ are the desired joint stiffness, damping, and apparent mass matrices, respectively, for each articulation.

If the dynamical model is perfectly estimated, then, by combining Equations (3.3) and (3.4), one gets the expected behavior:

$$\boldsymbol{K}_{qd}(\boldsymbol{q}_d - \boldsymbol{q}) + \boldsymbol{B}_{qd}(\dot{\boldsymbol{q}}_d - \dot{\boldsymbol{q}}) - \boldsymbol{M}_d\ddot{\boldsymbol{q}} = \boldsymbol{\tau}_e \ . \tag{3.5}$$

Most often, diagonal matrices are used for $\boldsymbol{K}_{qd}$, $\boldsymbol{B}_{qd}$ and $\boldsymbol{M}_d$, leading to n independent 1-DoF dynamic equations. The lowest order gives the static relationship between input displacement, stiffness, and output interaction torques.

3.1.2 Cartesian Impedance control

The same methodology can also be applied to the operational space in order to link F/T interactions of the end-effector to the Cartesian displacements. This means creating, between $\boldsymbol{x} \in \mathbb{R}^6$ the Cartesian 6-dimensional pose (position and orientation) and $\boldsymbol{F}_e \in \mathbb{R}^6$ the end-effector generalized interaction forces, the following the dynamical relationship:

$$\boldsymbol{K}_d(\boldsymbol{x}_d - \boldsymbol{x}) + \boldsymbol{B}_d(\dot{\boldsymbol{x}}_d - \dot{\boldsymbol{x}}) - \boldsymbol{\Lambda}_d\ddot{\boldsymbol{x}} = \boldsymbol{F}_e \ , \tag{3.6}$$

where $\boldsymbol{x}_d$ is the virtual desired position, $\boldsymbol{K}_d$, $\boldsymbol{B}_d$, $\boldsymbol{\Lambda}_d$ are the symmetric and positive definite matrices of the desired stiffness, damping, and inertia, respectively.

Implementing this Cartesian behavior to the redundant manipulator while controlling the joint torques in the articular space is a little bit more challenging but has been meticulously treated in literature in [Khatib, 1987], and [Ott, 2012]. The method consists in writing an equivalent robot model in the Cartesian space:

$$\boldsymbol{\Lambda}(\boldsymbol{x})\ddot{\boldsymbol{x}} + \boldsymbol{\mu}(\boldsymbol{x}, \dot{\boldsymbol{x}})\dot{\boldsymbol{x}} + \boldsymbol{F}_g(\boldsymbol{x}) = \boldsymbol{F}_c + \boldsymbol{F}_\mathrm{e} \tag{3.7}$$

where $\boldsymbol{F}_c$, $\boldsymbol{F}_g$, $\boldsymbol{F}_e \in \mathbb{R}^6$ are the equivalent task space input, gravity and generalized external forces vectors, and $\boldsymbol{\Lambda}(\boldsymbol{x})$, $\boldsymbol{\mu}(\boldsymbol{x}, \dot{\boldsymbol{x}})$ are given by:

$$\boldsymbol{\Lambda}(\boldsymbol{x}) = \boldsymbol{J}(\boldsymbol{q})^{-T}\boldsymbol{M}(\boldsymbol{q})\boldsymbol{J}(\boldsymbol{q})^{-1} \ , \tag{3.8}$$

$$\boldsymbol{\mu}(\boldsymbol{x}, \dot{\boldsymbol{x}}) = \boldsymbol{J}(\boldsymbol{q})^{-T}\left(\boldsymbol{C}(\boldsymbol{q}, \dot{\boldsymbol{q}}) - \boldsymbol{M}(\boldsymbol{q})\boldsymbol{J}(\boldsymbol{q})^{-1}\dot{\boldsymbol{J}}(\boldsymbol{q})\right)\boldsymbol{J}(\boldsymbol{q})^{-1} \ . \tag{3.9}$$

thanks to the robot Jacobian $\boldsymbol{J} \in \mathbb{R}^{6\times n}$.

Several implementations for impedance control have been proposed in the literature [Song et al., 2019]. With Hogan's classical formulation [Hogan, 1985], the Cartesian impedance control law is given by:

$$\boldsymbol{F}_c = \hat{\boldsymbol{F}}_{\boldsymbol{g}}(\boldsymbol{x}) + \boldsymbol{F}_e + \hat{\boldsymbol{\mu}}(\boldsymbol{x}, \dot{\boldsymbol{x}})\dot{\boldsymbol{x}}_d + \hat{\boldsymbol{\Lambda}}(\boldsymbol{x})\boldsymbol{\Lambda}_d^{-1}(\boldsymbol{K}_d(\boldsymbol{x}_d - \boldsymbol{x}) + \boldsymbol{B}_d(\dot{\boldsymbol{x}}_d - \dot{\boldsymbol{x}}) - \boldsymbol{F}_e) \ . \tag{3.10}$$

To avoid a feedback of the external forces $\boldsymbol{F}_{\mathrm{e}}$ in the control loop, a simplification consists in setting the desired inertia to the robot inertia ([Ott, 2012]), *i.e.*, $\boldsymbol{\Lambda}_d = \hat{\boldsymbol{\Lambda}}(\boldsymbol{x})$, leading to the following desired torque output :

$$\begin{aligned} \boldsymbol{\tau_c} &= \boldsymbol{J}(\boldsymbol{q})^T \boldsymbol{F}_c \\ &= \boldsymbol{g}(\boldsymbol{q}) + \boldsymbol{J}(\boldsymbol{q})^T \left(\hat{\boldsymbol{\mu}}(\boldsymbol{x}, \dot{\boldsymbol{x}})\dot{\boldsymbol{x}}_d + \boldsymbol{K}_d(\boldsymbol{x}_d - \boldsymbol{x}) + \boldsymbol{B}_d(\dot{\boldsymbol{x}}_d - \dot{\boldsymbol{x}})\right) \end{aligned} \tag{3.11}$$

3.2 State of the art of force regulation in impedance control

Within the classical impedance control framework, a reference force cannot be directly specified as command input. To regulate interaction forces while benefiting from the robustness of the impedance control framework, researchers proposed various modifications to impedance control or additional external control loops.

Lasky and Hsia [Lasky and Hsia, 1991] proposed a simple inner-outer loop control scheme. The inner loop consisted of an impedance controller; The outer loop, an integral force controller, generated a proper position command based on the force error. Following this work, Almeida et al. [Almeida et al., 1999] proposed a force-limited impedance control, meaning that the contact force was limited to a maximum reference force value using saturation blocks. Meanwhile, the robot was only impedance-controlled with an inactive external force loop if the contact force was less than the reference value.

Seraji and Colbaugh [Seraji and Colbaugh, 1997] presented two adaptive inner-outer loop control schemes. In the first scheme, the adaptive force controller generated the position command based on the force error and the end-effector's velocity. The second scheme estimated the environment's parameters using the end-effector's position and contact force. Then, the position command was generated based on the environment's estimated parameters. Following this study, [Erickson et al., 2003] [Xu et al., 2012] [Komati et al., 2014] introduced force tracking adaptive impedance controllers in which different algorithms were implemented for identification of the environment's parameters. Most of these adaptive schemes require data on the end-effector's position, velocity, and contact force.

Jung et al. [Jung et al., 2004] proposed a two-phase control algorithm – contact-less space and contact space. After contact, a new impedance function was realized based on the desired force, the position error, and the environment stiffness. An adaptive technique was utilized to minimize the force error. Implementation of this control algorithm required switching between the control algorithms. Also, the contact force was measured by an F/T sensor.

Also, [Kronander and Billard, 2016] showed that modifying the robot's desired stiffness online can provoke internal energy production, leading to instability. Instead, following the works of [Ferraguti et al., 2013], K. Kronander et al. prone the use of energy tanks to prevent instability.

Force control without F/T sensors is also of value for various industrial applications because it would reduce the costs and complexities of implementation[Stolt et al., 2012] [Kuo et al., 2019] . In a recent study, Roveda and Piga [Roveda and Piga, 2021] presented an inner-outer loop control scheme in which the contact force was estimated using an extended Kalman filter. The main challenge was the accuracy of force estimation and, subsequently, the static force control error.

In the proposed scheme, detailed later in Section 3.3.3, we use an unmodified inner impedance loop and an outer force loop that neither needs to estimate the environment's parameters nor measure the external force.

3.3 Robust force regulation for impedance control

This section theoretically compares the works performed in [Lasky and Hsia, 1991; Almeida et al., 1999], hereafter referred to as the "direct force feedback" approach, to a "pseudo-force feedback" proposed approach that will be introduced in Section 3.3.3. Both methods use an inner classical implementation of impedance control coupled with an outer external force loop.

To compare theoritically the stability of the two different external force loops applied on top of the impedance controller, we will consider a one-dimensional problem and use lowercase letters to symbolize scalars:

$$m_d\ddot{x} = k_d(x_d - x) + b_d(\dot{x}_d - \dot{x}) - f_e \ . \tag{3.12}$$

This one DoF may be a robot joint from decoupled Equation (3.5), or an end-effector DoF from decoupled Equation (3.6). The following 1-DoF simulation study could have been done either with a translational degree or rotational degree. The stability analysis and step response simulations shown in this section are done on a 1-DoF translational system, but the same applies to joint articulations.

3.3.1 1-DoF environment model

When there is no contact between the robot and the environment ($f_e = 0$), the closed-loop behavior given by Equation (3.12) is stable for all the positive choices of m_d, b_d, and k_d. When contact occurs, the programmed impedance of the robot connects to the environment's own impedance. For completeness, we consider a second-order impedance for the model of the environment:

$$f_e = \begin{cases} k_e(x - x_e) + b_e\dot{x} + m_e\ddot{x} & \text{when in contact} \\ 0 & \text{otherwise} \end{cases} , \tag{3.13}$$

where k_e, b_e, m_e, and x_e are the stiffness, damping, mass and the environment position, respectively.

Once in contact, the closed-loop contact behavior of the combined mechanical system, depicted in Figure 3.1, can be obtained from Equations (3.12) and (3.13):

$$m_t\ddot{x} + b_t\dot{x} + k_t x = k_d x_d + k_e x_e + b_d\dot{x}_d , \tag{3.14}$$

where $\star_t$ stands for $\star_d + \star_e$. This combined system is still stable for all positive choices of k_d, b_d, and m_d, although the environment affects its convergence dynamics. Note that the stability of the two systems (contact / free-space) does not guarantee the overall system's stability due to non-linear switching between the two differential equations.

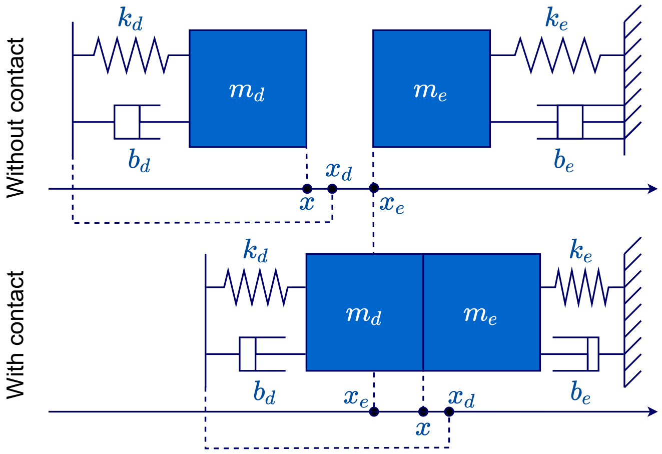

FIGURE 3.1: Impedance control principle: the desired robot impedance is programmed with m_d, b_d, and k_d resulting in a stable behavior in both free-space and contact situations. The interaction force f_e is not directly controlled. Instead, the desired position of the robot, x_d shall be chosen to adjust f_e, which requires knowledge of the environment's location and dynamics.

The equilibrium position x_{eq} of the combined system can be directly obtained from Equation 3.14:

$$x_{eq} = \frac{k_d x_d + k_e x_e}{k_d + k_e} \ . \tag{3.15}$$

Note that this position not only depends on the controlled stiffness of the robotic arm but also on the stiffness and position of the environment.

In the following simulations, for simplification and without any impact on the stability analysis, we will assume $x_e(t) = 0$. Moreover, we will assume permanent contact to study contact stability by removing potential instability coming from switching, which is a common approach in the force control community. The robustness to switching conditions (impacts) is evaluated experimentally in Section 3.5.2.

3.3.2 Direct measurement feedback

A common approach seen in the literature to regulate forces to a desired force input f_d while being under impedance control is to implement an external force loop based on F/T sensor measurements [Lasky and Hsia, 1991; Almeida et al., 1999]. The conversion from force errors to velocities is usually done via a proportional gain λ like so:

$$\dot{x}_d = \lambda(f_d - f_e) \ . \tag{3.16}$$

With this method, the sensor measurement explicitly creates a speed error that is then fed to the impedance controller, as shown in Figure 3.2. In doing so, all the environment dynamics are fed back to the external force loop and the impedance controller.

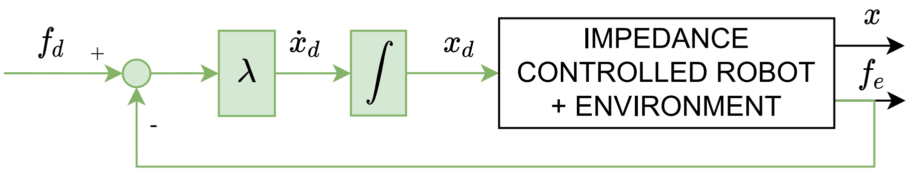

FIGURE 3.2: External force loop with measured force feedback.

3.3.2.1 Stability analysis

In the Laplace domain, if we consider F_e as the output and F_d as the input, by combining Equations (3.13), (3.14), and (3.16), the transfer function can be written as:

$$F_e = \frac{\lambda(k_d + b_d s) Z_e(s)}{D(s)} F_d \ , \tag{3.17}$$

where $Z_e(s) = m_e s^2 + b_e s + k_e$ is the environment's impedance, and $D(s)$ is a third-order polynomial given by:

$$D(s) = \lambda k_d k_e + [k_t + \lambda(k_d b_e + b_d k_e)]\, s + [b_t + \lambda(b_d b_e + k_d m_e)]\, s^2 + [m_t + \lambda b_d m_e] s^3 \ . \tag{3.18}$$

This third-order polynomial has roots whose values and signs depend on the robot's impedance, the environment's impedance, and the proportional gain λ. We applied the Routh-Hurwitz criterion to find the analytical stability conditions. The Routh table is:

s^3	$m_t + \lambda m_e b_d$	$k_t + \lambda k_d b_e$
s^2	$b_t + \lambda b_e b_d + \lambda k_d m_e$	$\lambda k_e k_d$
s^1	$\dfrac{(b_t + \lambda b_e b_d + \lambda k_d m_e)(k_t + \lambda k_e b_d + \lambda k_d b_e) - \lambda k_e k_d (m_t + \lambda m_e b_d)}{b_t + \lambda b_e b_d + \lambda k_d m_e}$	0
s^0	$\lambda k_e k_d$	0

So the system is stable if, and only if:

$$\begin{aligned} &(b_t + \lambda b_e b_d + \lambda k_d m_e)(k_t + \lambda k_e b_d + \lambda k_d b_e) - \lambda k_e k_d (m_t + \lambda m_e b_d) > 0 \\ &\Rightarrow k_t b_t + \lambda(k_e b_d b_t + k_d b_e b_t + k_t b_e b_d + k_d^2 m_e - k_e k_d m_d) \\ &\quad + \lambda^2 (k_e b_e b_d^2 + k_d b_d b_e^2 + k_d^2 m_e b_e) > 0 \ . \end{aligned}$$

For example, when $b_e = m_e = 0$ (environment being modeled as a pure spring), we find that the system is stable if: $\lambda > 0$ and $b_d > \sqrt{k_d m_d}$ or $b_d < \sqrt{k_d m_d}$ and $0 < \lambda < \lambda_{\text{lim}}$ where

$$\lambda_{\text{lim}} = \frac{b_d (1 + k_d / k_e)}{k_d m_d - b_d^2} \ . \tag{3.19}$$

In this configuration, the higher the environment stiffness, the lower the maximum limit for the external gain. This stability problem is also reported in several experiments in the literature [An and Hollerbach, 1987; Wilfinger et al., 1994]. To cope with this problem, authors often use low values of λ to ensure stability in contact with stiff environments, leading to slow convergence for softer environments. Alternatives include direct or indirect adaptive approaches [Seraji and Colbaugh, 1997].

3.3.2.2 Simulated step response

Several simulations have been performed to confirm the influence of the different variables on stability and performance. Table 3.1 provides the parameters which are common in the three simulation trials presented in this section.

k_d	4000 N.m^{-1}	b_d	50 N.s.m^{-1}	m_d	9 kg
k_e	20 000 N.m^{-1}	b_e	20 or 300 N.s.m^{-1}	m_e	0.5 kg

TABLE 3.1: Parameters used to obtain all the simulation results plotted in Figures 3.3, 3.4 and 3.6.

Figure 3.3 shows the step responses of the system for various values of the λ and b_e parameters.

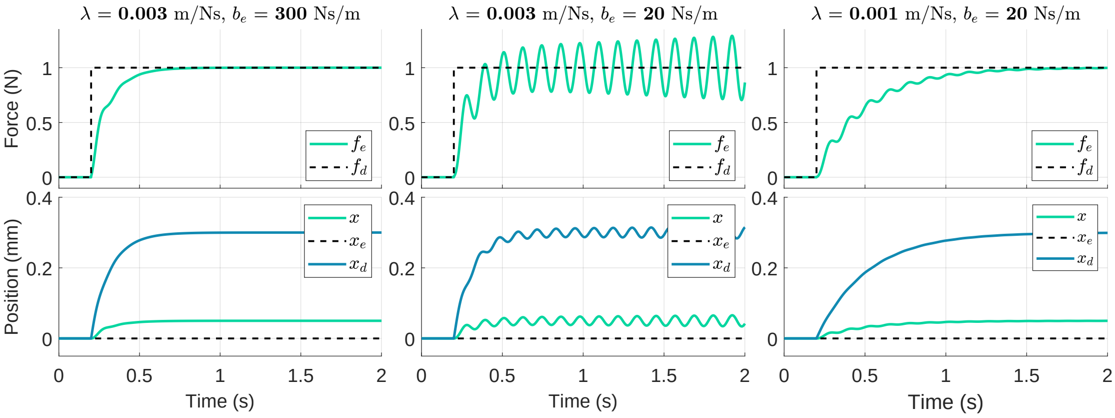

FIGURE 3.3: Step responses with an explicit external force loop.
Left: for a given environment dynamics, λ is tuned to obtain a well-damped behavior.
Middle: With the same λ, but a lower environment damping, instability occurs.
Right: Lowering λ allows retrieving stability while slowing down the step response.

In Figure 3.3-left, λ was manually tuned to 3 mm.s^{-1}.N^{-1} in order to obtain a well-damped force response, given an environment dynamics characterized by a high damping (b_e = 300 N.s.m^{-1}). This shows that, with the right tuning, the direct force feedback approach can lead to fast convergence on high-damped materials.

In Figure 3.3-middle, the damping is decreased (to b_e = 20 N.s.m^{-1}), corresponding to a low-damped environment dynamics, while the controller gain λ is unchanged. This demonstrates that the closed-loop behavior of the explicit approach is highly sensitive to change and can become unstable.

In Figure 3.3-right, we show how decreasing λ allows retrieving stability for the low-damped environment. However, this also slows down the dominant poles, leading to a lower convergence rate than in 3.3-left.

In practice, when the environment dynamics are unknown, a conservatively low value is selected for λ to ensure stability for a large set of environment dynamics at a price of low force tracking performance (slow response). Note that when x_e is not constant, this does not affect the closed-loop dynamics. In this case, having a slow response is detrimental to the capacity of the robot to follow environment movements with high-frequency contents.

As emphasized by the stability analysis and simulation results, the coupling of robot low-level impedance, and environment impedance, with an outer force feedback loop has a potentially negative effect on the overall system stability. A fundamental reason for this is that the outer loop re-injects the force output signal f_e and its high-frequency oscillatory components, see Figure 3.3. Filtering f_e to remove those high frequencies would delay the signal and impose reducing λ to maintain enough stability margins.

In the next section, a pseudo-force feedback is proposed, rejecting high-frequency components, while avoiding filtering.

3.3.3 Proposed pseudo-force feedback

From Equation (3.12) we noticed that thanks to the inner impedance controller, the low-frequency component of the interaction force can be approximated by the static elastic force. We take advantage of this fact to propose a new robust interaction force controller using a pseudo-force signal:

$$\tilde{f}_e = k_d(x_d - x) \ . \tag{3.20}$$

In Figure 3.4, we plotted for the previous simulation the total force f_e and the elastic contribution of the impedance controller to this force, $\tilde{f}_e$. As expected, at the equilibrium, the two forces are equal. More importantly, during the transient response, it can be observed that most of the high-frequency oscillation is largely smaller for the elastic component.

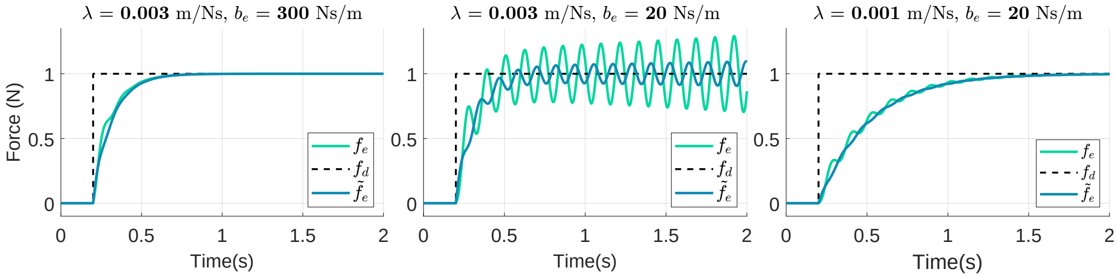

FIGURE 3.4: Reproduction of the step responses of Figure 3.3 with the superimposition of a pseudo-force signal $\tilde{f}_e = k_d(x_d - x)$.

This pseudo-force $\tilde{f}_e$ signal was firstly used in [Hacksel and Salcudean, 1994; Alcocer et al., 2003] to build force observers. More recently [Borghesan et al., 2012; Stolt et al., 2012], used the backdrivability of low-impedance robots (PR2 and ABB Frida) to regulate interaction forces. But, the influence of replacing f_e by $\tilde{f}_e$) has never been thoroughly studied in terms of control performance and robustness.

We then propose to use $\tilde{f}_e$ and use it as force feedback:

$$\dot{x}_d = \lambda(f_d - \tilde{f}_e) \ , \tag{3.21}$$

resulting in the control scheme depicted in Figure 3.5.

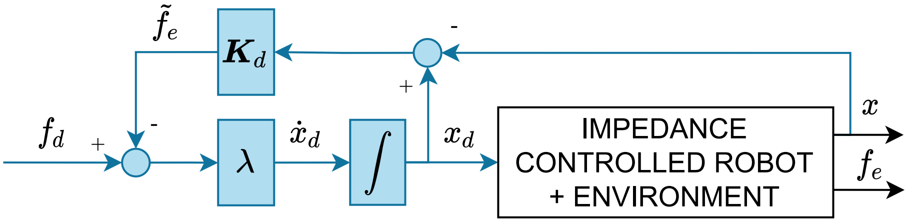

FIGURE 3.5: Proposed external loop with pseudo-force feedback.

One immediate advantage of this approach is that, as shown in Fig. 3.5, there is no direct feedback of $\boldsymbol{f}_e$ to the force loop. Also, this outer loop only requires position measurements and the stiffness gain K_d of the impedance controller.

3.3.3.1 Stability analysis

To evaluate the stability of the proposed approach, we can combine Equations (3.12), (3.13), (3.21) to get its equivalent transfer function:

$$F_e = \frac{\lambda(k_d + b_d s)Z_e(s)}{\lambda k_e k_d + (k_t + \lambda k_d b_e)s + (\lambda m_t k_d + b_t)s^2 + m_t s^3} F_d \ , \tag{3.22}$$

The Routh table for this system:

s^3	m_t	$k_t + \lambda k_d b_e$
s^2	$b_t + \lambda k_d m_t$	$\lambda k_e k_d$
s^1	$\frac{(b_t + \lambda k_d m_t)(k_t + \lambda k_d b_e) - \lambda k_e k_d m_t}{b_t + \lambda k_d m_t}$	0
s^0	$\lambda k_e k_d$	0

proves that the proposed approach is stable if:

$$\begin{gathered}(b_t + \lambda k_d m_t)(k_t + \lambda k_d b_e) - \lambda k_e k_d m_t > 0 \\ \Rightarrow k_t b_t + \lambda k_d b_t b_e + \lambda k_d^2 m_t + \lambda^2 k_d^2 b_e m_t > 0 \\ \Rightarrow \lambda > 0 \ .\end{gathered}$$

Hence, with the pseudo-force feedback, the theoretical stability of the controller is now ensured for all positive values of k_e, k_d, b_e, b_d, m_e, m_d, and λ.

3.3.3.2 Simulated step response

Unconditional stability has been confirmed via an extensive set of simulations, all leading to convergence of f_e towards f_d. As an example, we show in Figure 3.6 the simulation results for the same tuning as in Figure 3.3. In the most critical situation (middle column, with high λ and low environment damping), while the system exhibits small vibrations for f_e, the pseudo-force signal, which is used as feedback, rapidly converges towards the desired value with very few oscillations. Remarkably, the integral compensation output, x_d, stays perfectly smooth under all three conditions (blue signal of the bottom plots).

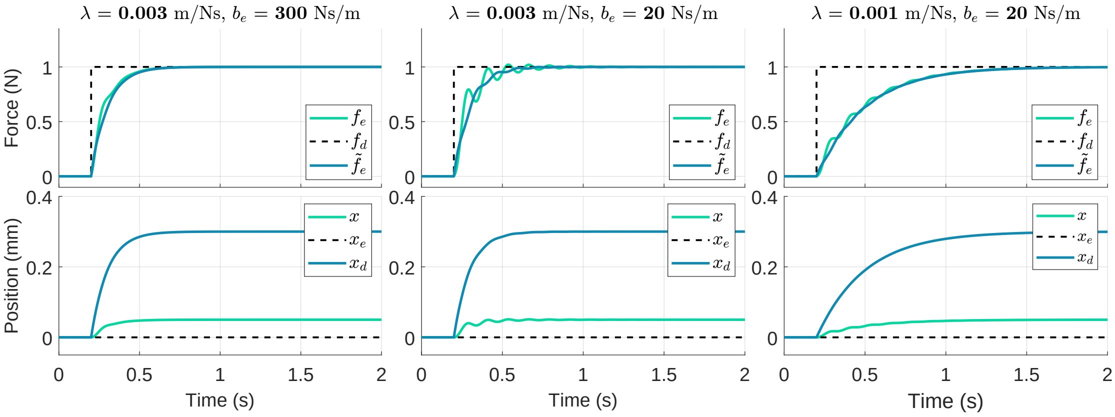

FIGURE 3.6: Step responses with the proposed external pseudo-force loop under the same conditions as in Figure 3.3.

To demonstrate the improvements obtained with this approach under real-life conditions, we present its application with joint impedance in Section 3.4, and with Cartesian impedance in Section 3.4 to regulate the force applied during the drilling task.

3.4 Application to joint impedance control

Due to the manipulator's inherent redundancy and the additional degree of freedom provided by the drill's motor, 8 DoFs are available in total on our robotic system (see Section 2.1 for details). In this section, to take full advantage of these two extra mobilities while accomplishing the drilling task, the proposed force control approach is applied to the inner joint impedance controller provided by the KUKA arm.

A robust hybrid position/force controller is implemented, as well as an interactive null-space control law – both exploiting the pseudo-force signal. The robustness of the controller is then tested in various experiments and evaluated in the context of our medical application.

3.4.1 Operational space force control with joint impedance

As the impedance control is done at the joint level, while the task is in the operational space, the proposed feedback, in Equation (3.20), is now applied to all articulations in a pseudo-torque signal

$$\tilde{\boldsymbol{\tau}}_e = \boldsymbol{K}_d(\boldsymbol{q}_d - \boldsymbol{q}) \ . \tag{3.23}$$

With the pseudo-torque signal $\tilde{\boldsymbol{\tau}}_e$ alone, it is not possible to distinguish between an action of the robot through contacts occurring on intermediate bodies or through a distal interaction at the end-effector level. To compute an equivalent pseudo-force from the pseudo-torque, we have to assume that all the external torque is due to an interaction at the end-effector level. With that hypothesis, a pseudo-force $\tilde{\boldsymbol{F}}_e$ can be computed from the pseudo-torque with

$$\tilde{\boldsymbol{F}}_e = (\boldsymbol{J}^{\dagger})^T \tilde{\boldsymbol{\tau}}_e \ , \tag{3.24}$$

where $\boldsymbol{J}^{\dagger} = \boldsymbol{J}^T(\boldsymbol{J}\boldsymbol{J}^T)^{-1}$ is the Moore-Penrose pseudo-inverse [Penrose, 1955] of the robot Jacobian.

By generalizing Equation (3.21) to all Cartesian axes with Equation (3.24), it is possible to control the end-effector Cartesian velocity to regulate the desired interaction F/T, $\boldsymbol{F}_d$, applied to an environment with

$$\dot{\boldsymbol{x}}_d = \boldsymbol{\lambda}(\boldsymbol{F}_d - (\boldsymbol{J}^{\dagger})^T \tilde{\boldsymbol{\tau}}_e) \ , \tag{3.25}$$

where $\boldsymbol{\lambda}$ is a diagonal matrix of proportional λ gains.

The robot Jacobian is then used to map back the Cartesian end-effector velocities $\dot{\boldsymbol{x}}_d$ into a desired joint velocities $\dot{\boldsymbol{q}}_d$, with:

$$\dot{\boldsymbol{q}}_d = \boldsymbol{J}^{\dagger} \dot{\boldsymbol{x}}_d \ . \tag{3.26}$$

3.4.2 Parallel hybrid position/force control

To fulfill the requirements of our drilling application, we need to be able to apply a constant force along the tool axis while maintaining the desired orientation and entry-point. This requires 1 DoF to apply the force along the drill axis, 2 DoFs to position the entry point, and 2 DoFs to control the drill orientation. The third rotation does not need to be controlled by the robot arm since a separate motor inside the power drill tool (presented in Section 2.1.3) handles the instrument's infinite rotation around its axis. The drilling task can then be separated into three parallel subtasks: force, orientation, and lateral displacement control.

By using selection matrices $\boldsymbol{S}_\star$ and their complementary $\boldsymbol{I} - \boldsymbol{S}_\star$, as introduced by [Mason, 1981] and directly applied by [Raibert and Craig, 1981], the control other the different axes can be parallelized to separate each subtask. We will use $\boldsymbol{S}_f$ to select the axes requiring the proposed pseudo-force regulation and $\boldsymbol{S}_p$ for position control, as the same controller will handle orientation and lateral displacement. Noting that some Cartesian axis might not need either position or force control, a second selection matrix $\boldsymbol{S}_p$ is introduced for the position tasks as well; $(\boldsymbol{I} - \boldsymbol{S}_p - \boldsymbol{S}_f)$ can be not null.

In our force control approach, the position of the environment is not taken into account. Unlike in the external hybrid force/position scheme in [Perdereau and Drouin, 1993], we do not feed position and force inputs to the same Cartesian axis and consider them as two different subtasks. Hence, an axis should not be selected for more than once subtask, meaning $\boldsymbol{S}_p \cdot \boldsymbol{S}_f = \boldsymbol{0}$. Then, the desired Cartesian input speed $\dot{\boldsymbol{x}}_d$ can be divided into three terms:

$$\dot{\boldsymbol{x}}_d = \dot{\boldsymbol{x}}_{d/f} + \dot{\boldsymbol{x}}_{d/p} \ , \tag{3.27}$$

where $\dot{\boldsymbol{x}}_{d/f} = \boldsymbol{S}_f \dot{\boldsymbol{x}}_d$ and $\dot{\boldsymbol{x}}_{d/p} = \boldsymbol{S}_p \dot{\boldsymbol{x}}_d$.

Nonetheless, to limit the maximum speed in case of loss of contact, we saturate the velocities controlled by the force controller with

$$\dot{\boldsymbol{x}}_{d/f} = \mathrm{sat}(\boldsymbol{\lambda} \boldsymbol{S}_f (\boldsymbol{F}_d - \tilde{\boldsymbol{F}}_e), v_{\max}) \ , \tag{3.28}$$

where $v_{\max}$ is the maximum allowed velocity and

$$\mathrm{sat}(\boldsymbol{a}, b) = \begin{cases} \boldsymbol{a}, \text{ if } \|\boldsymbol{a}\| \leq b \\ b \dfrac{\boldsymbol{a}}{\|\boldsymbol{a}\|}, \text{ otherwise,} \end{cases} \tag{3.29}$$

Note that, even if the primary task for the axes selected by $\boldsymbol{S}_f$ is to regulate desired F/T, motion in free-space can be induced by playing with $\boldsymbol{v}_{\max}$ and $\boldsymbol{F}_d$. Therefore, the speed is controlled in free space, or the force is controlled when in contact, without switching the controller.

Moreover, when setting $\boldsymbol{F}_d = 0$, the end-effector pseudo-forces $\tilde{\boldsymbol{F}}_e$ created from the manipulation of the robot by an operator will be regulated to zero by translating and rotating the end-effector away from contact; Creating thus a collaborative environment where the user can drag the robot in the workspace by pulling the end-effector. For that scenario, a deadzone function DZ for vectors is introduced:

$$DZ(\boldsymbol{a}, b) = \begin{cases} 0 & \text{if } \|\boldsymbol{a}\| \leq b \\ (\|\boldsymbol{a}\| - b) \dfrac{\boldsymbol{a}}{\|\boldsymbol{a}\|} & \text{otherwise.} \end{cases} \tag{3.30}$$

When applied before the force error $\Delta \boldsymbol{F} = \boldsymbol{F}_d - \tilde{\boldsymbol{F}}_e$ computation, the deadzone ensures that small force errors won't create unwanted movement of the end-effector, even in the presence of static torque errors (due *e.g.* to residual friction or gravity model errors). Equation (3.28) then becomes:

$$\dot{\boldsymbol{x}}_{d/f} = \mathrm{sat}(\boldsymbol{\lambda} \boldsymbol{S}_f (DZ(\boldsymbol{F}_d - \tilde{\boldsymbol{F}}_e, F_{th})), v_{\max}) \ , \tag{3.31}$$

where F_{th} is a force or torque threshold.

3.4.3 Null-space control

Within the 6 Cartesian DoFs to control, if $m \leq 6$ forces/torques are controlled, $p \leq 6-m$ positions/rotations can be regulated along the directions selected by $(\boldsymbol{I} - \boldsymbol{S}_f)$. Thanks to the selection matrices introduced earlier and the robot's inherent redundancy, this leaves $r = (7 - m - p)$ DoFs for internal motion.

To control only the $m + p$ DoFs required for Cartesian position or force control, the selection matrices can be used to create a reduced Jacobian matrice

$$\boldsymbol{J}_{red} = (\boldsymbol{S}_p + \boldsymbol{S}_f)\boldsymbol{J} \ . \tag{3.32}$$

Then, by using a null-space projector [Liégois, 1977], we can allow motions that won't affect the Cartesian tasks. Equation (3.26) then becomes:

$$\dot{\boldsymbol{q}}_d = \boldsymbol{J}_{red}^{\dagger} \dot{\boldsymbol{x}}_d + (\boldsymbol{I}_n - \boldsymbol{J}_{red}^{\dagger} \boldsymbol{J}_{red}) \dot{\boldsymbol{q}}_{null} \tag{3.33}$$

where $\dot{\boldsymbol{q}}_{null} \in \mathbb{R}^n$ is a joint velocity that can be used for any secondary tasks. This additional internal motion can be used, *e.g.*, to change the robot's configuration while maintaining force and orientation control over the tool.

We allowed human collaborators to interactively act on this kinematic null-space by implementing a parallel external joint admittance loop. Similarly to the approach seen in the previous section for the Cartesian velocities with Equation (3.31), equivalent joint speeds $\dot{\boldsymbol{q}}_{null}$ are created from torque errors by using a proportional gain, a deazone and a saturation with:

$$\dot{\boldsymbol{q}}_{null} = \mathrm{sat}\left(\beta \left(DZ\left(-\tilde{\boldsymbol{\tau}}_e, \tau_{th}\right)\right), \dot{q}_{\max}\right) \ , \tag{3.34}$$

where β is a second tunable scalar viscosity parameter, τ_{th} is a torque threshold, and $\dot{q}_{\max}$ is a maximal joint velocity.

The global control diagram used to control Cartesian positions and forces in parallel while allowing changes in the robot configuration is shown in Figure 3.7. The implementation inside KUKA's control box has not been released publically. Hence, the interior of the orange block displayed in this figure is just a guess from our user experience and might differ from reality.

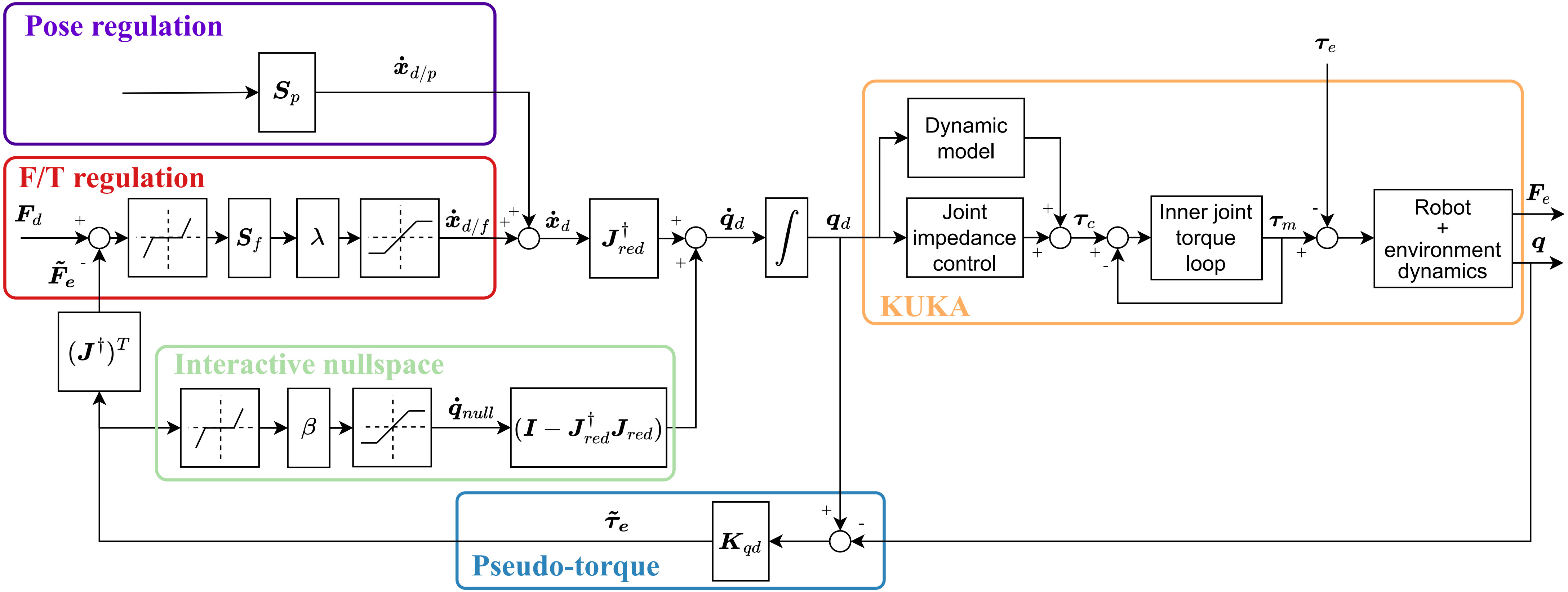

FIGURE 3.7: Overall proposed control diagram implemented with LBR Med's internal joint impedance controller for robust force/position control during bone drilling.

3.4.4 Experimental results

A series of experiments have been conducted to verify the behavior of the proposed force controller with KUKA's inner joint impedance controller in various conditions. Figure 3.8 shows the setup used, consisting of the robot arm, a hard-plastic tool with a rounded tip mounted on the flange, an F/T sensor, and the breathing platform (see Section 2.2.1.3).

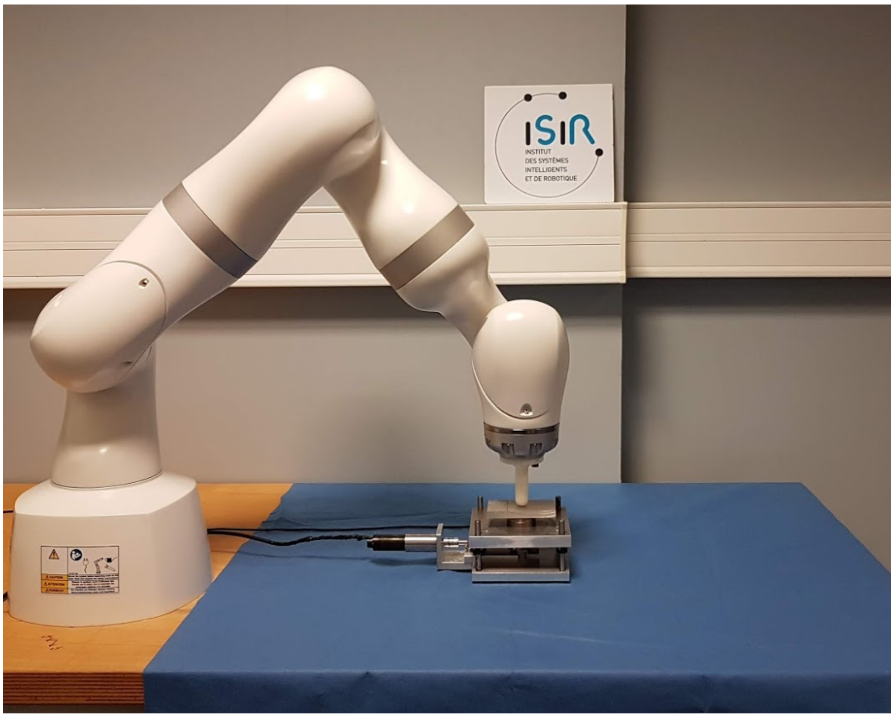

FIGURE 3.8: Setup used to experimentally evaluate the application of the proposed hybrid position/force controller to joint impedance.

Only the vertical component of the distal force is servoed, corresponding to all the elements of $\boldsymbol{S}_f$ being null apart from one diagonal term in the vertical translation direction equal to 1. The complete control diagram of Figure 3.7 is used with the parameters of Table 3.2.

$\boldsymbol{K}_{qd}$	1000 Nm.rad^{-1} for all joints	$\boldsymbol{B}_{qd}$	1 for all joints
λ	30 mm.s^{-1}.N^{-1}	$v_{\max}$	0.02 m.s^{-1}
$\boldsymbol{S}_f$	diag(0,0,1,0,0,0)	$\boldsymbol{S}_p$	diag(1,1,0,1,1,0)
β	0.2 rad.s^{-1}.Nm^{-1}	$\dot{q}_{\max}$	1.2 rad.s^{-1}
τ_{th}	0.2 Nm		

TABLE 3.2: Control parameters used for the joint impedance experiments.

3.4.4.1 Impact experiment

This experiment compares the robot's behavior when using pseudo or direct force feedback while impacting a surface.

The robot first starts above the contact surface. Then, thanks to Equation (3.28), the end-effector moves towards contact, with a max speed of $v_{max} = 2$ cm.s^{-1}. Then, instantly after contact (no switch function is required), the controller regulates the estimated interaction force to the desired value f_d =20N. The same experiment is performed four times: either on a highly rigid environment (an aluminum plate) or on a soft environment obtained by placing a 1cm thick silicon sample between the robot end-effector and the aluminum plate, and either with the direct or proposed feedback. The breathing machine placed under the force sensor is not actioned in this first experiment. All the results are available in Figure 3.9.

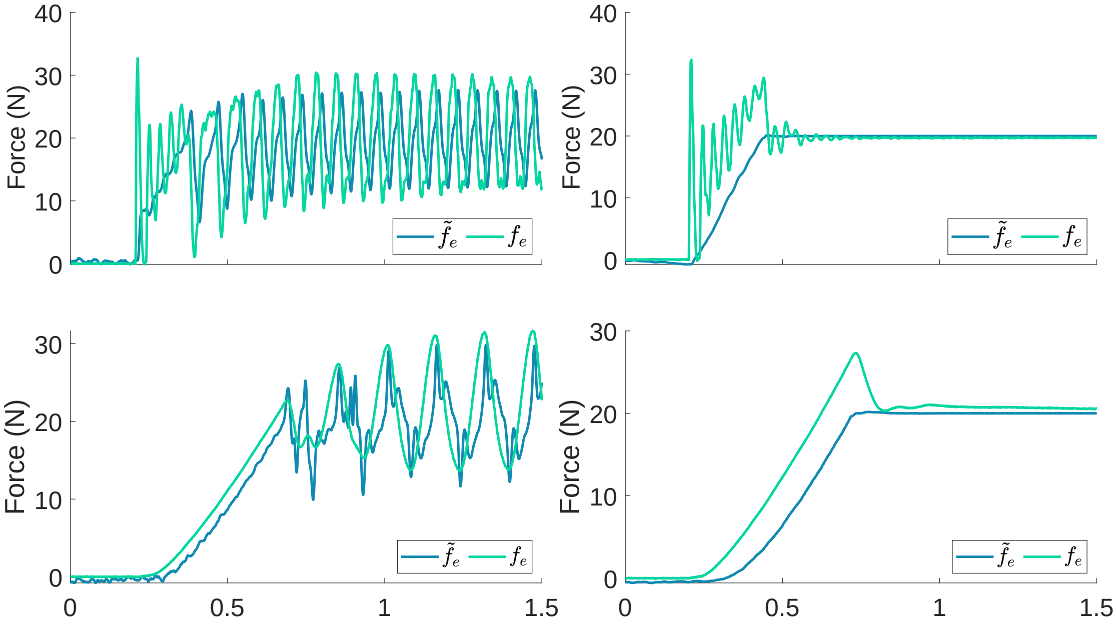

(A) With measured forces. (B) With pseudo-torques.

FIGURE 3.9: Comparison of the two force control approaches when impacting at $v_{max} = 2$ cm.s^{-1} two different environment material.
Top: hard aluminium. **Bottom**: soft silicon.

Figure 3.9A plots the force results when using real force measurements as feedback. Permanent oscillations appear on both soft and hard environments. Here, the speed saturation prevents the robot from diverging by inducing a limit cycle behavior [Liu and Michel, 1992]. Oscillations occur even if the theoretical stability criteria for the classical approach are respected. This can be due to the complexities that have been neglected in the model used for the 1-DoF stability analysis.

In Figure 3.9B, the same experiments are performed except that the pseudo-force signal is used instead for force regulation. A robust stable behavior is observed. The pseudo-force signal $\tilde{f}_e$ used in the external F/T loop is remarkably smooth and rapidly converges towards the desired value. The slope observed to reach the desired value corresponds to the saturation of $\dot{\boldsymbol{x}}_{d/f}$ by $v_{\max}$.

It can also be observed that the stability is robust to drastic changes in the environment stiffness. With the high stiffness environment (top plot), large vibrations are measured at the robot tip on the external F/T sensor. However, they are kept out of the regulation loop and thus do not affect the overall stability.

A small error can be observed between the pseudo-force signal and the external – ground truth – measurement. It is due to errors in the internal model estimation and residual friction that are not compensated for by the built-in torque loops used in the impedance loop.

Due to its clear superiority in terms of stability and robustness, only the pseudo-force approach is used in the following experiments.

3.4.4.2 Moving environment

To verify the robustness of the proposed force controller when servoing a force on moving environments, additional experiments have been performed while at contact on the breathing platform, moving back and forth along the vertical direction. Figure 3.10 shows the results of the outer loop when the contact moves towards the robot at an

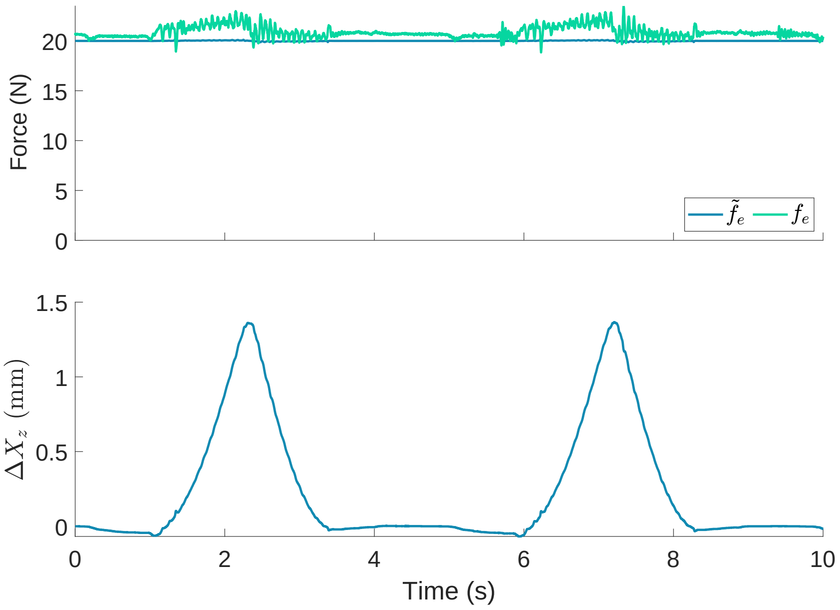

Figure 3.10: Servoing a constant force while in contact with a moving environment.

approximative frequency of 0.2Hz with a maximum amplitude of 1.4mm. The externally regulated force $\tilde{\boldsymbol{f}}_e$ smoothly remains very closed to the 20N desired value. The end-effector externally-measured force slightly differs from the estimates during movements due to dynamical and frictional effects. However, these errors are limited to 2N.

3.4.4.3 Null-space motion

In the two following experiments, the null-space configuration of the robot is changed while the robot is asked to apply a constant force of 20N on a fixed rigid environment.

In Figure 3.11, a desired motion is created computationally on the first joint – without any human interaction. This movement is then projected in the null-space. One can see that the results are similar to those obtained in the previous experiment, with small errors due to the torque loop dynamics and the errors in estimating the robot dynamics. However, these errors remain small, although large null-space joint movements are executed.

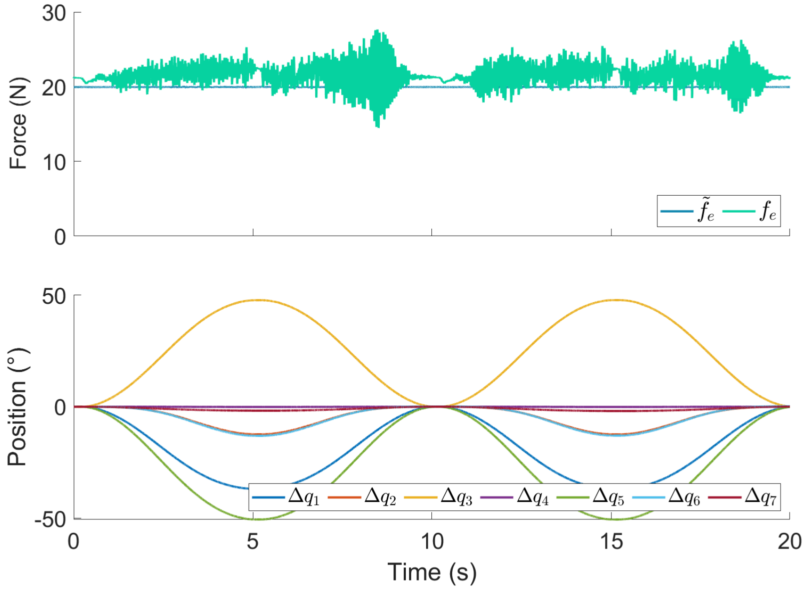

FIGURE 3.11: Controlling a distal force while a null-space motion is imposed by the controller, without any interaction between the robot intermediate bodies and external agents. In the bottom plot, $\Delta q_i(t) = q_i(t) - q_i(0)$.

In Figure 3.12, the null-space motion is provoked by the application of a force by a human collaborator on the robot's elbow thanks to the implementation of Equation (3.34). It can be noticed that the externally measured force differs from the estimated distal force by a significant amount during the motion. This is due to the fact that the hypothesis made for Equation (3.24), namely that all the external torque is due to a distal

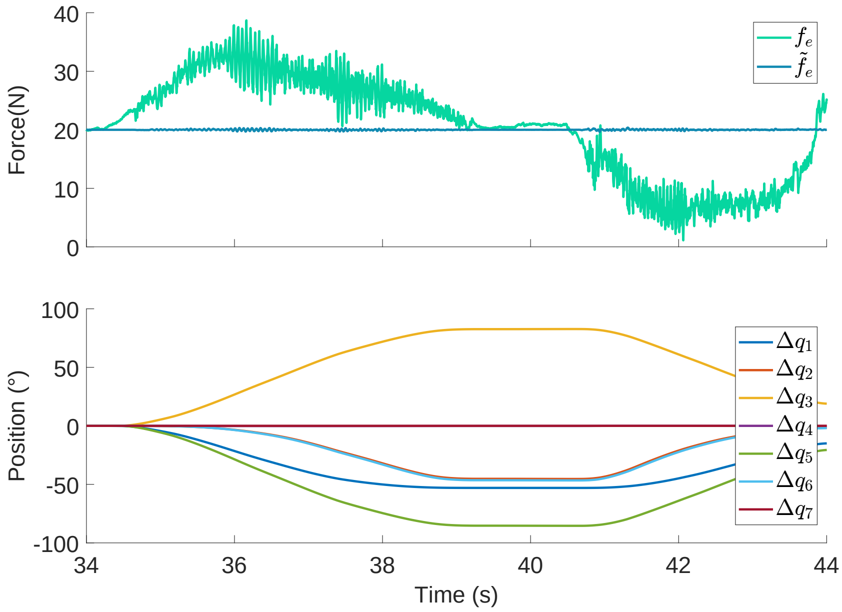

Figure 3.12: Controlling a distal force while a null-space motion is imposed by a human agent applying forces on the robot intermediate bodies

interaction only, is not valid anymore in this application because a force is applied by the agent on the elbow. As it can be observed on the plots, the practical consequence is that the distal force actually applied is a combination of the desired force and the human-applied force, without significant impact on the stability of the external F/T regulation loop (smooth blue signal). This provided additional experimental evidence of the proposed approach's robustness, *i.e.,* when $\tilde{f}_e$ is used as a feedback signal.

3.4.5 Task-oriented performances for bone drilling

The two following scenarios assess the proposed controller for our surgical drilling application. In the first case, we verify if it is possible to follow the patient's motion robustly. In the other one, we evaluate the precision of position control.

3.4.5.1 *In-vivo* patient motion following

The breathing of the patient lying down induces a motion of a few millimeters on the vertebrae. In order to verify that the proposed controller could follow this small periodic motion automatically, we recorded the robot's Cartesian position and pseudo-force signal while applying a constant force with the proposed controller on different vertebrae.

Figure 3.13 shows that the breathing induced to the animal is indeed periodic and that the robot does follow the contact smoothly. The amplitude of the breathing on the

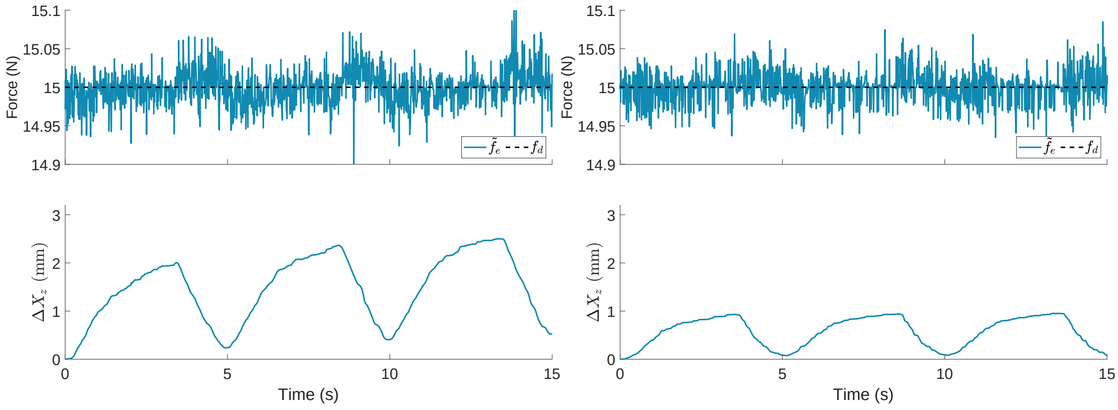

(A) L1. (B) L5.

FIGURE 3.13: Evaluation of the motion induced by the breathing of the animal when applying a fixed force of 15N with the proposed controller

L1 level is more significant than on L5 since L1 is closer to the thoracic cage, which is where the main part grows via the induced airflow.

The general controller of Figure 3.7 has been extensively used in the operating room on living animals (see Section 2.2.2), as it was used during all bone drilling experiments later presented in Chapter 4.

3.4.5.2 Coupling effect

One of the main characteristics of using an impedance controller is that the robot is programmed to be flexible. This impacts the precision of the position control. Having the impedance programmed at the joint level with the $\boldsymbol{K}_{qd}$ stiffness leads to an equivalent non-diagonal Cartesian stiffness matrix $\boldsymbol{K}_x$ that depends on the robot's joint configuration, but also on the external force [Chen and Kao, 2000]:

$$\boldsymbol{K}_x = (\boldsymbol{J}^\dagger)^T(\boldsymbol{K}_{qd} - \boldsymbol{K}_g)\boldsymbol{J}^\dagger \ , \tag{3.35}$$

where $\boldsymbol{K}_g$ is the complementary stiffness matrix defined in [Chen, 2003]:

$$\boldsymbol{K}_g = \begin{bmatrix} \frac{\partial \boldsymbol{J}^T}{\partial q_1}\boldsymbol{F_e} & \frac{\partial \boldsymbol{J}^T}{\partial q_2}\boldsymbol{F_e} & \frac{\partial \boldsymbol{J}^T}{\partial q_3}\boldsymbol{F_e} & \frac{\partial \boldsymbol{J}^T}{\partial q_4}\boldsymbol{F_e} & \frac{\partial \boldsymbol{J}^T}{\partial q_5}\boldsymbol{F_e} & \frac{\partial \boldsymbol{J}^T}{\partial q_6}\boldsymbol{F_e} & \frac{\partial \boldsymbol{J}^T}{\partial q_7}\boldsymbol{F_e} \end{bmatrix} . \tag{3.36}$$

Even if the joint stiffness is set to the maximum value allowed by the KUKA Sunrise cabinet (1000 Nm.rad^{-1} for all joints), the resulting Cartesian stiffness is not sufficient in many robot configurations of our application. To estimate the displacement error induced by the application of a force, we can use Equations (3.23), (3.24) and (3.26) for small displacements:

$$\delta \boldsymbol{x} = \boldsymbol{J}\delta\boldsymbol{q} = \boldsymbol{J}\boldsymbol{K}_{qd}^{-1}\delta\boldsymbol{\tau}_e = \boldsymbol{J}\boldsymbol{K}_{qd}^{-1}\boldsymbol{J}^T\delta\boldsymbol{F}_e \ . \tag{3.37}$$

In the robot configuration of Figure 3.8, with $F_e = 20$N in the z direction, the displacements predicted by the model given by Equation 3.37 are 3.3mm on the x-axis and 1.02° around the y-axis.

To verify experimentally this prediction, we measured the deviation from the trajectory when contacting a hard environment at high speed. Figure 3.14 shows the translation and rotation on the robot flange when contacting a hard surface at $v_{\max} = 0.1$ m.s^{-1} with the proposed controller implemented with the joint impedance controller. The low stiffness and impact create a deviation of 3.5mm along x and a rotation of 0.8 degrees around y, close from the theoretical model. Disprepancies may be due to joint friction.

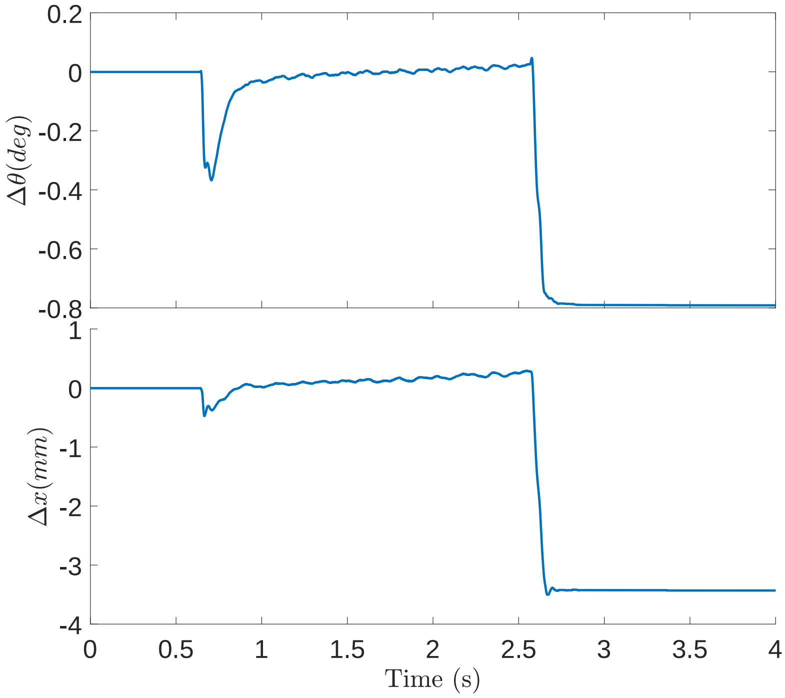

FIGURE 3.14: Position and orientation errors when contacting a hard surface at $v_{\max} = 0.1$ m.s^{-1} with $F_d = 20$N and the maximum joint stiffness.

3.4.5.3 Conclusion on the joint impedance implementation

With the experiments presented in this Section, we have seen that the proposed force control method allows following the patient smoothly while maintaining a constant interaction force. We have seen briefly that using a force sensor to do the same thing is not robust enough and is more expensive.

However, the coupling effect from articular impedance to cartesian control degrades the positioning accuracy along the directions perpendicular to the applied forces. In the next section, we'll use a Cartesian implementation of impedance control to remove this coupling effect. Moreover, the robustness is studied via experiments that compare the sensor's or the pseudo-force feedback more thoroughly.

3.5 Experiments with Cartesian impedance control

The model used in the previous section to conduct the theoretical stability analysis and the simulations was simplistic: the robot structural flexibility was neglected, the dynamic linearization performed by the low-level impedance controller was supposed to be perfect, the joint friction was neglected, the sampling effect was not considered, and the contact was supposed to be bilateral (, *i.e.* permanent, without switching between contact and free-space). In practice, these assumptions are never perfectly met and restrict the stability domain for the gain λ. Therefore, studying the real experimental behavior of the proposed approach is of primary importance.

Two sets of experiments have been conducted to compare the robustness of the two presented controllers. The first set evaluates the stability of both methods with respect to the proportional gain $experimentallylambda$. The second one evaluates the stability in case of impact between the robot and its environment at different velocities.

In order to simulate a 1-DoF robotic system, we will use the built-in Cartesian impedance controller provided by the KUKA LBR 7 Med robot (see Section 2.1.1) and servoed only the z-axis of the robot's end-effector. Meanwhile, the desired velocity inputs for the other axes were set to 0. All the axes were controlled by the internal Cartesian impedance controller with the maximum possible stiffness, *i.e.*, $k_d = 5000$ N/m for translational axes and $k_d = 300$ Nm/rad for rotational axes. The Lehr damping ratio was set to 1, meaning $b_d = 2\sqrt{k_d m_d}$ where m_d is unknown – not disclosed in KUKA's documentation.

Figure 3.15 shows the mechanical setup that was used for the two sets of experimental evaluations. A hard tip-rounded plastic tool was fixed on the robot's flange. An ATI Mini 40 F/T sensor was placed on the robot's wooden table to acquire the best possible interaction force measurement at 1kHz using a NI 6034E acquisition card. An aluminum plate is placed on the sensor to flatten the contact surface. Additionally, a low-stiffness spring can be added on top to simulate a soft contact. The end-effector's axis was then controlled with the classical or proposed method.

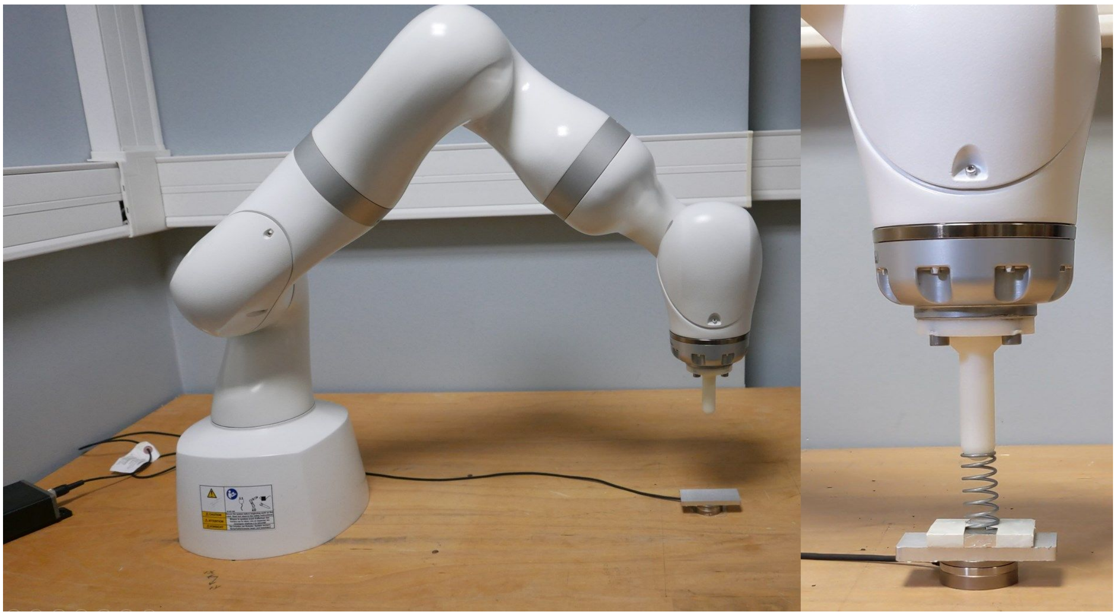

FIGURE 3.15: Setup used to experimentally evaluate both force control loops. A spring is placed between the force sensor and the robot to realize low stiffness environment experiments; it is removed for high stiffness environment experiments.

3.5.1 Experimental evaluation of λ on the stability

First, to evaluate the stability with respect to the λ gain and its influence on the behavior of both controllers, we conducted experiments where the robot was already in contact with the environment. Moreover, the speed saturation to $v_{\max}$ was disabled for these experiments. We then sent force step commands to f_d from 10N to 15N for the two possible controllers with increasing λ values until the system became unstable. The tests were performed on a soft environment and on a hard contact.

3.5.1.1 On a soft environment

A series of experiments have been conducted on a low-stiffness spring positioned between the force sensor and the robot's end-effector. The λ gain was increased incrementally with steps of 0.5 mm.s^{-1}.N^{-1}.

Figure 3.16 shows the step response of both methods with a low λ value. There is an approximate difference of 5 Newtons between f_e and $\tilde{f}_e$ due to an error in the gravity compensation model of the internal KUKA controller. Moreover, the real force amplitude is different from 5N (6N) when using the pseudo-force, which can be explained by the friction on the joints that affects the torque sensor measurement while not affecting the distal measurements. Apart from this shift, the behavior with a low gain is very similar for both controllers. The convergence rate is around 1.5 seconds.

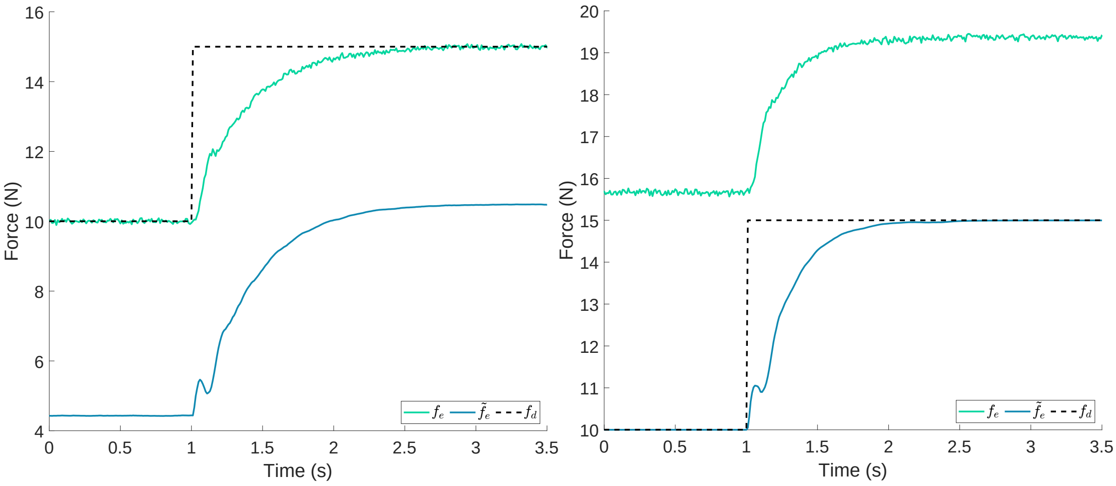

(A) With the direct force feedback (f_e).

(B) With the proposed pseudo-force ($\tilde{f}_e$).

FIGURE 3.16: Response to 5N steps with a low gain ($\lambda = 2$ mm.s^{-1}.N^{-1}) for both control approaches on a soft environment.

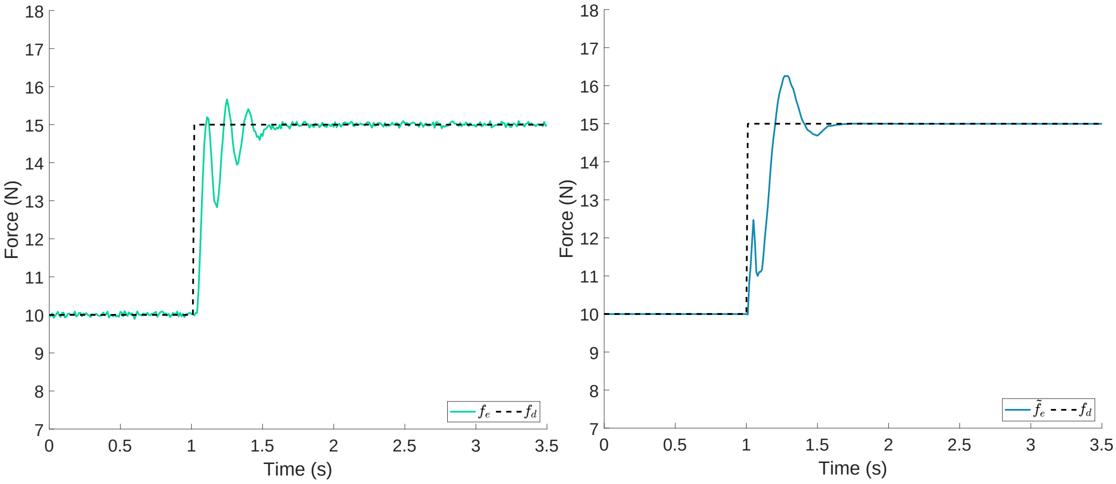

(A) With the direct force feedback (f_e)

(B) With the proposed pseudo-force ($\tilde{f}_e$)

FIGURE 3.17: Response to 5N steps with $\lambda = 8$ mm.s^{-1}.N^{-1} for both control approaches on a soft environment.

By increasing the gain, we can start to see apparent differences between the two control methods. For instance, in Figure 3.17, we observe that the frequency of the oscillations created by the direct force feedback is higher than with the pseudo-force signal with less damping. The response with $\tilde{f}_e$ exhibits higher overshoots but higher damping as well.

If we keep increasing λ we quickly reach the limits of stability with the direct force feedback. Indeed, Figure 3.18 shows the responses of both controllers with the highest possible λ before the system got unstable with the f_e feedback. With the same value of $\lambda = 10.5$ mm.s^{-1}.N^{-1}, we can see many oscillations when using the measured force signal

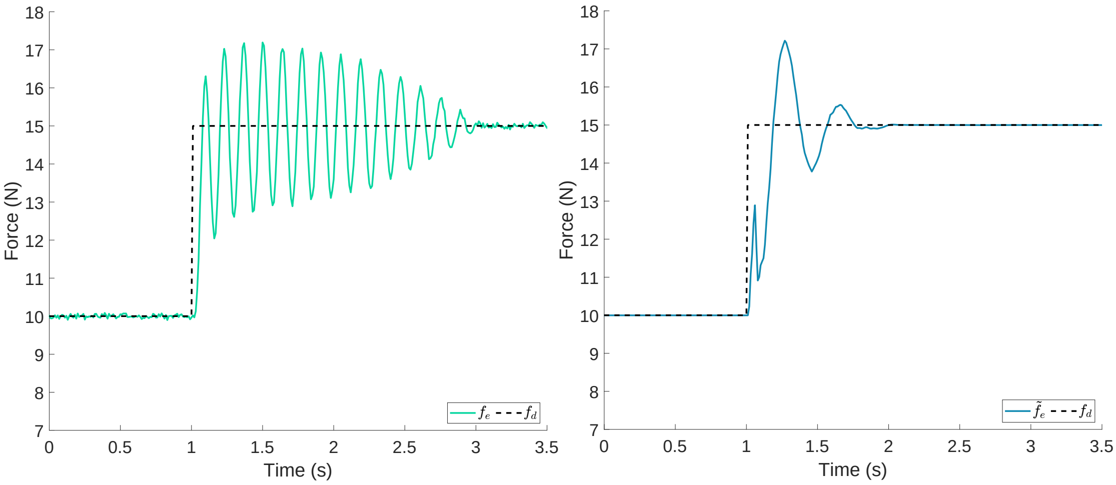

(A) With the direct force feedback (f_e)

(B) With the proposed pseudo-force ($\tilde{f}_e$)

FIGURE 3.18: Response to 5N steps with $\lambda = 10.5$ mm.s^{-1}.N^{-1}.

directly, but only two when using the pseudo-force. The overshoots are comparable for both approaches in this case.

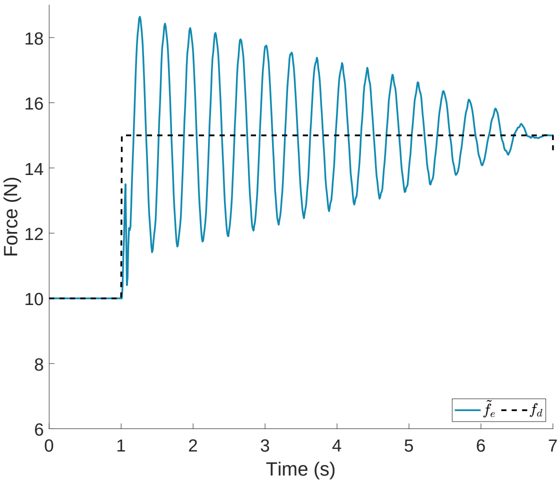

FIGURE 3.19: Behavior of the pseudo-force feedback at the limit of stability with $\lambda = 15.5$ mm.s^{-1}.N^{-1}.

Of course, the proposed method also has an experimental stability limit, even if stability is unconditional for a simplified model. Figure 3.19 shows the servoing of the pseudo-force signal at the limit of stability with $\lambda = 15.5$ mm.s^{-1}.N^{-1}.

3.5.1.2 On a hard contact

Similar experiments have been conducted on a hard contact case by removing the spring from the previous setup. This task is much more challenging in terms of stability compared to the soft contact case since the environment can no longer absorb vibrations.

Energy dissipation at contact is low while the feedback gain is higher due to the higher environment stiffness.

Figure 3.20 shows the step response of both methods with a low λ value. Like on the soft environment, both controllers have similar behaviors. Nonetheless, the pseudo-force control is slightly faster. The 2% settling time is 0.7s with the pseudo-force feedback versus 0.9s with the direct force measurement.

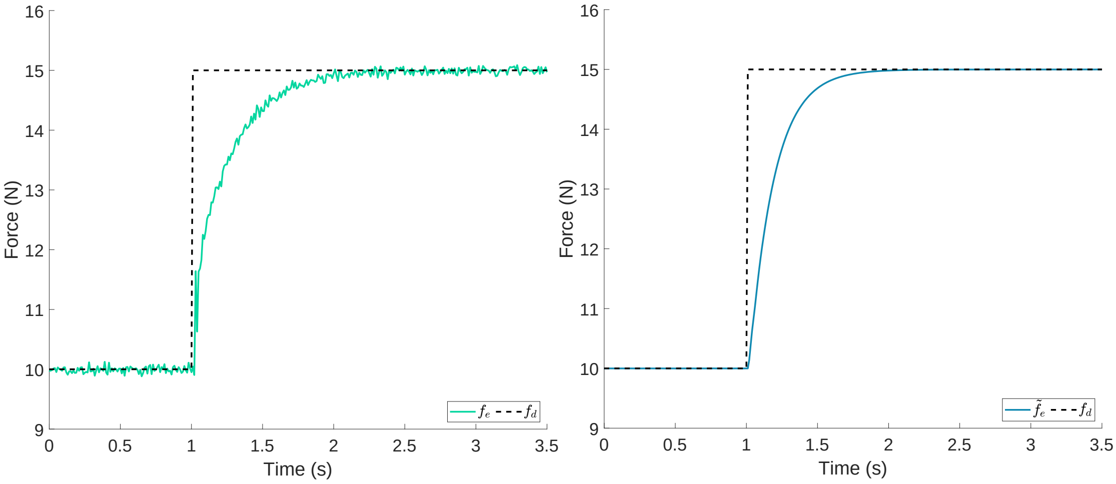

(A) With the direct force feedback (f_e).

(B) With the proposed pseudo-force ($\tilde{f}_e$).

FIGURE 3.20: Response to 5N steps with a low gain $\lambda = 1.2$ mm.s^{-1}.N^{-1} on a hard environment.

When increasing the gain with the direct force feedback, the control experimentally exhibited high sensitivity to noise and nonlinearities. Figure 3.21 shows that with $\lambda = 3.5$ mm.s^{-1}.N^{-1}, the system was stable for the upwards step but became unstable during the downwards step. This can be attributed to a non-linear effect in the torque transmission, due to friction. Indeed, around t=2.6s, while the pseudo-force decreases (meaning that the error $x_d - x$ decreases) the effectively transmitted force increases. Then, at $t \approx 2.8s$, when the non-linear friction has been compensated for, the force transmission is effective again; This switch in the transmission model destabilizes the loop. Moreover, around t=2.6s, we can see that the force measurement increases while $\tilde{f}_e$ decreases – meaning while the robot moves away from the sensor. This may be explained by a nonlinearity or residual friction in the robot or in the force sensor.

On the contrary, it was possible to select several tuning values for λ when using the pseudo-force signal. The limit gain when using $\tilde{f}_e$ was $\lambda = 19$ mm.s^{-1}.N^{-1}. This gain is five times higher than the maximum gain when using the direct force feedback. Figure 3.22, shows the step-response for three different values of λ. With $\lambda = 7$ mm.s^{-1}.N^{-1}, the 2% settling time is 0.08s.

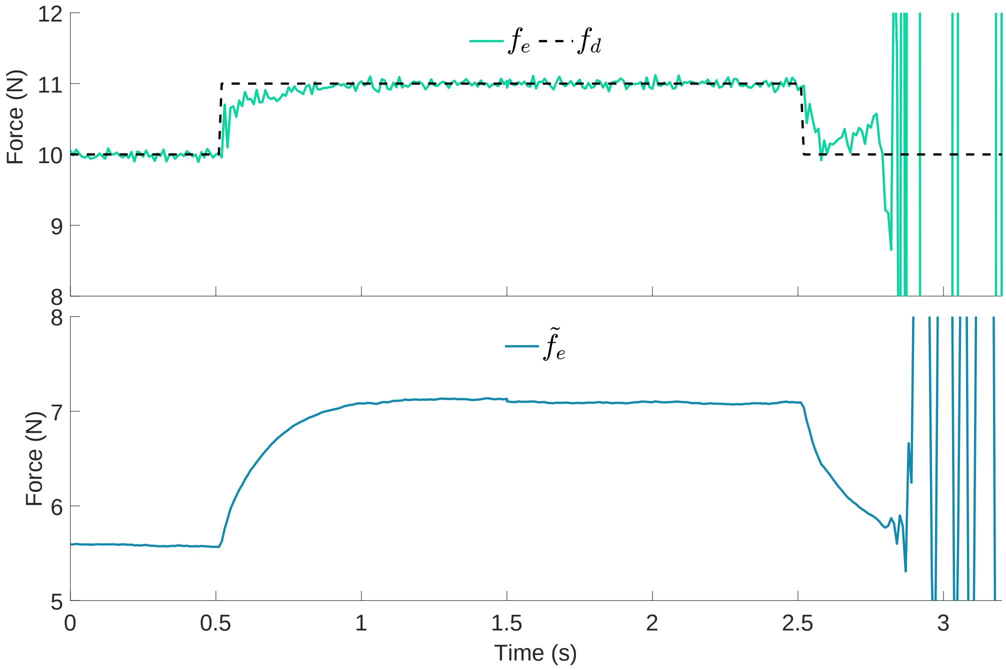

FIGURE 3.21: Direct force feedback becomes unstable with $\lambda = 3.5$ mm.s^{-1}.N^{-1} on a hard environment.

Moreover, Figure 3.22C shows that with $\lambda = 15$ mm.s^{-1}.N^{-1} the controller pushed the robot to bounce off contact since the measured force goes down to zero at t$\approx$ 0.28s. This does not create any problem for the pseudo-force regulation as they are no discontinuities in the pseudo-force signal.

3.5.2 Stability to impact

In this other experimental evaluation, the robot started above contact, in free space. The robot then moved towards impacting an environment whose location and dynamics were unknown at the controller level. The initial force error Δf and the saturation speed limit led the robot to reach the contact location at the impact speed $\dot{x} = \min(v_{\max}, \lambda\Delta f)$. Then, without the need for any switch function, the applied torque was regulated to f_d when reaching the contact. In the tests presented in this section, f_d was chosen high enough to make sure that $v_{\max}$ would be the saturated speed value. The experiments were conducted while modifying incrementally $v_{\max}$ for a fixed value of λ.

3.5.2.1 Gain tuning of lambda

The value of λ used for the impact experiments was identified thanks to the data gathered in the experiments of Section 3.5.1 in order to give the fastest response time while having

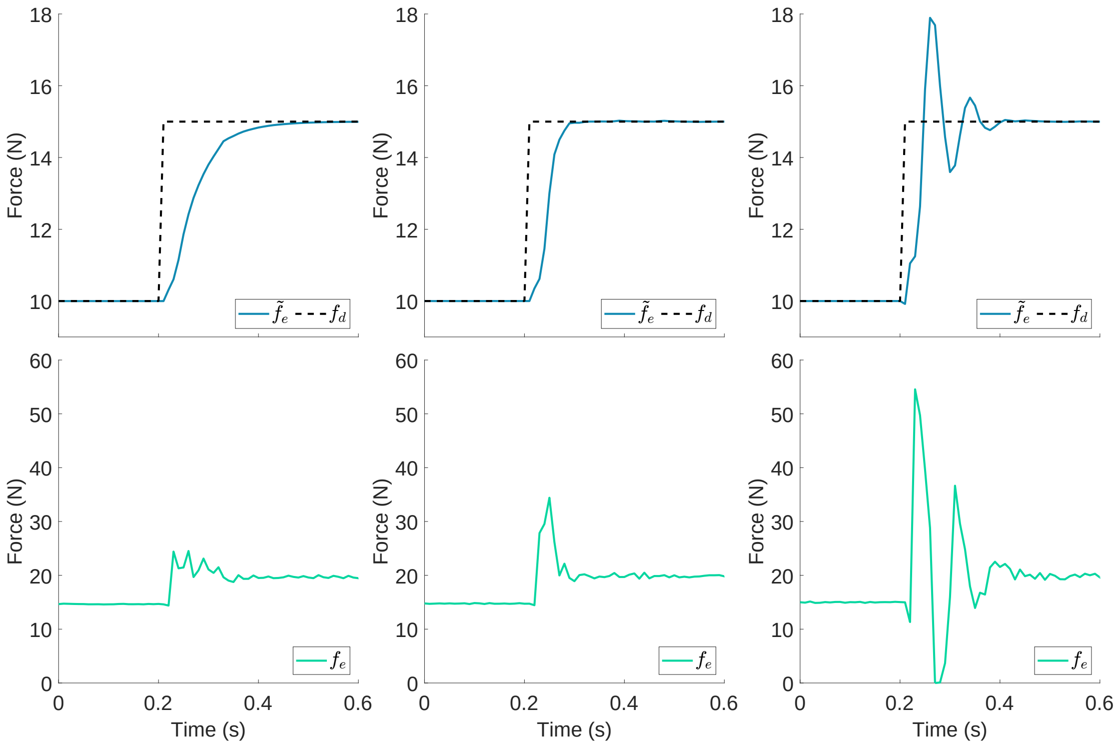

(A) $\lambda = 3.5$ mm.s^{-1}.N^{-1} (B) $\lambda = 7$ mm.s^{-1}.N^{-1} (C) $\lambda = 15$ mm.s^{-1}.N^{-1}

FIGURE 3.22: Step response with the pseudo-force feedback for different values of λ on a hard environment.

no overshoot for both controllers. This tuned lambda value is environment-dependent, so not the same for the soft or the hard environment.

For a soft environment For the soft environment, the proportional gain was tuned to $\lambda = 3.5$ mm.s^{-1}.N^{-1} because higher gains would start creating small overshoots with the pseudo-force feedback. Figures 3.23A and 3.23B show that with this value, both controllers respond in less than one second to a 5N step, with no overshoots.

For a hard environment For the hard contact on the aluminium plate, the proportional gain was tuned to $\lambda = 2$ mm.s^{-1}.N^{-1}. Figures 3.24A and 3.24B show the step responses with this value of λ.

3.5.2.2 Impacts on a soft environment

Figures 3.25A and 3.25B show the response of both controllers with this tuned $\lambda = 3.5$ mm.s^{-1}.N^{-1} when impacting the spring at $v_{\max} = 0.17$ m.s^{-1}. We can see that the f_e signal presents small oscillations while $\tilde{f}_e$ is much smoother. Also, overall, the

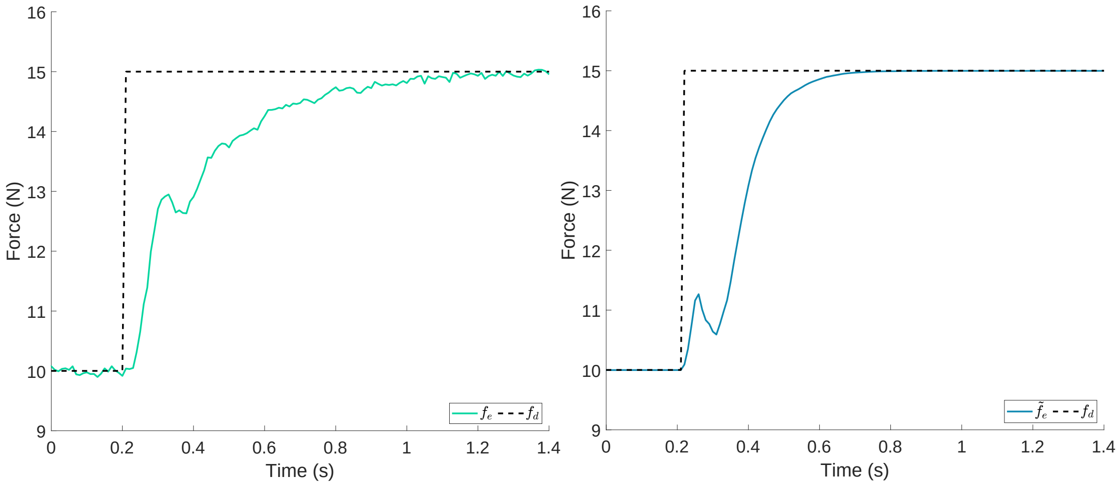

(A) Step response with f_e (B) Step response with $\tilde{f}_e$

FIGURE 3.23: Steps with the gain $\lambda = 3.5$ mm.s^{-1}.N^{-1} on a soft environment.

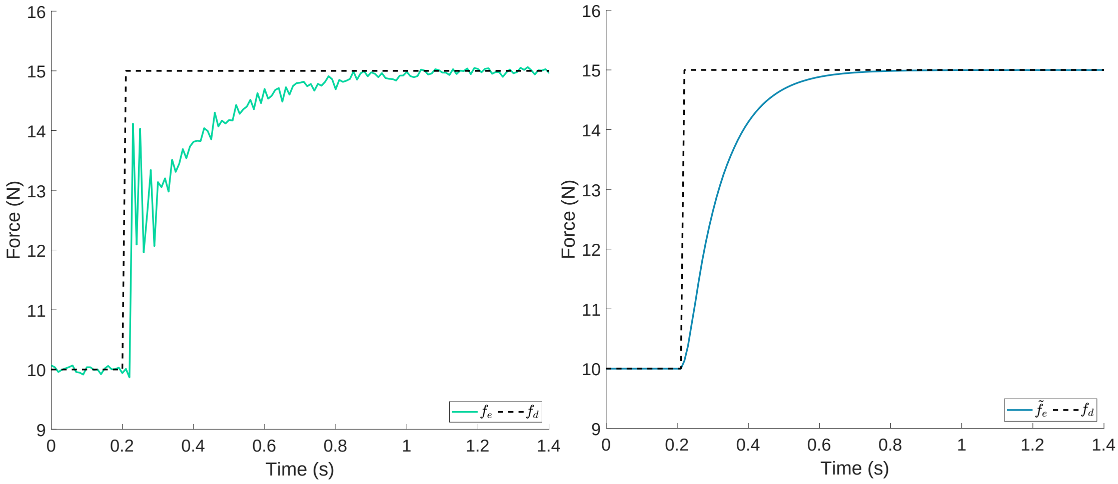

(A) Step response with f_e (B) Step response with $\tilde{f}_e$

FIGURE 3.24: Steps with $\lambda = 2$ mm.s^{-1}.N^{-1} on a hard environment.

regulation with the pseudo is again faster for the same λ gain: the 2% settling time is 0.8s with the direct feedback versus 0.5s with the pseudo-force feedback.

3.5.2.3 Impacts on a hard environment

Figure 3.27 shows the evolution of the convergence towards f_d for different impact speeds with the two considered regulation methods.

The moment of impact generates a peak in the f_e measurement. We can see the robot even starts bouncing over the contact surface since several null measurements are recorded for f_e after the impact. This phenomenon then generates high-frequency oscillations as it is forwarded to the command loop. Whereas the pseudo-force feedback is much

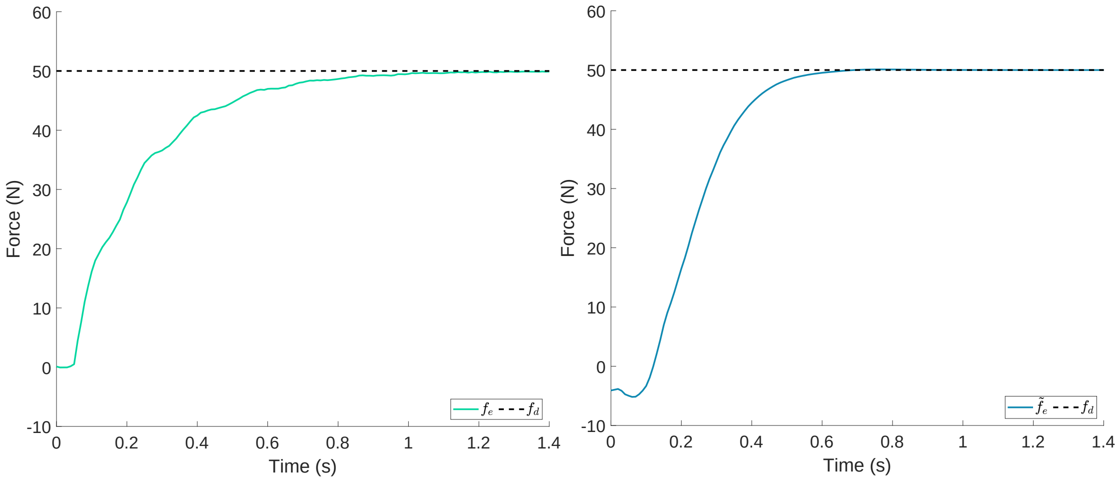

(A) Impact response with f_e

(B) Impact response with $\tilde{f}_e$

FIGURE 3.25: Behavior when impacting a soft environment at $v_{\max} = 0.17$ m.s^{-1}.

smoother since the nonlinearities provoked by the impact are not directly transmitted to the control loop.

So, in the end, the control with the pseudo-force feedback is faster as the 2% settling time is of 0.7s with the direct feedback, versus 0.6s with the pseudo-force feedback. But more importantly, $v_{\max}$ could not be increased further, as $v_{\max} = 0.007$ m.s^{-1} destabilizes the controller based on f_e.

Figure 3.26 shows a test with $v_{\max} = 0.210$ m.s^{-1} and $f_d = 30$N were the proposed pseudo-force controller was still stable and converged in 120 milli-seconds to the desired force input. The speed was not increased further to avoid damaging the force sensor or the robot arm.

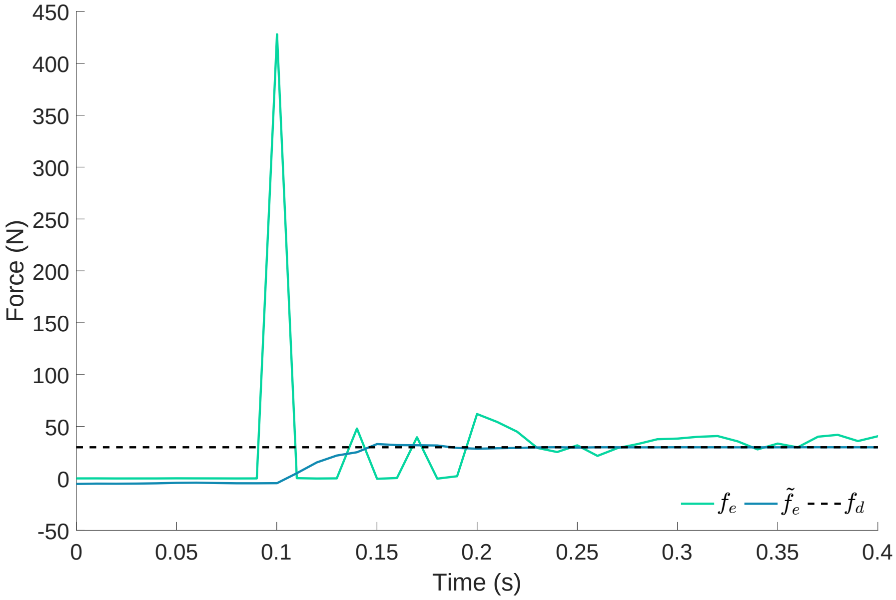

FIGURE 3.26: Behavior of the pseudo-force controller when impacting a hard environment at $v_{\max} = 0.210$ m.s^{-1} with $\lambda = 7$ mm.s^{-1}.N^{-1}.

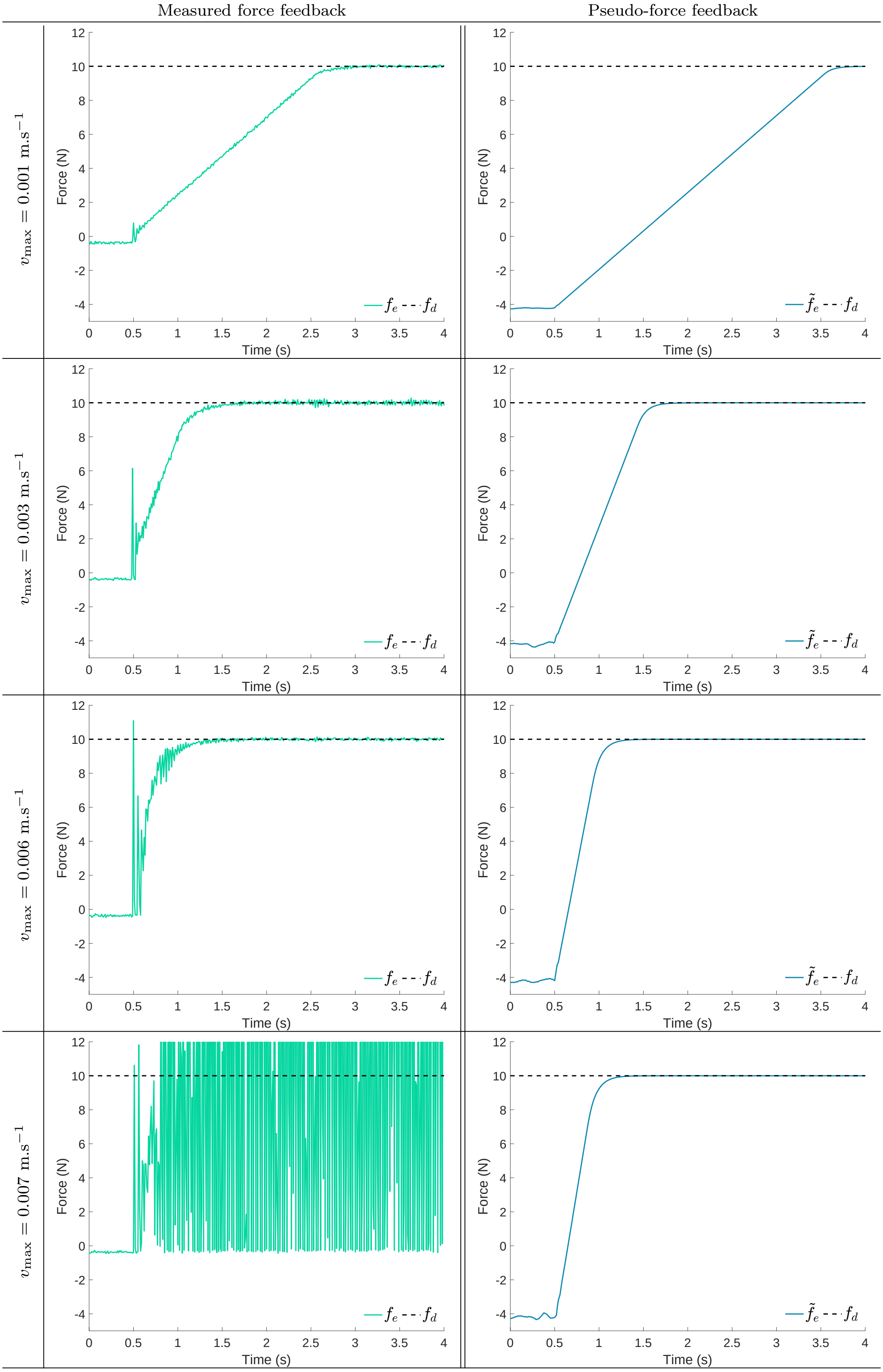

FIGURE 3.27: Behavior when impacting a hard environment with $\lambda = 2$ mm.s^{-1}.N^{-1} at different speeds.

3.5.3 Coupling effect

The experiment in Figure 3.14 (coupling effect evidenced under joint impedance control) has been reproduced to verify that the coupling effect does not appear with the Cartesian impedance implementation of the controller.

Figure 3.28 shows the deviation of the desired position and orientation with the joint and the Cartesian implementations. We can see that, because of the direct control at the Cartesian level, deviations induced by an impact are quickly corrected by the Cartesian impedance controller. After impact, the residual errors are 0.02 degrees and 0.44 millimeters, which is precise enough for our drilling application.

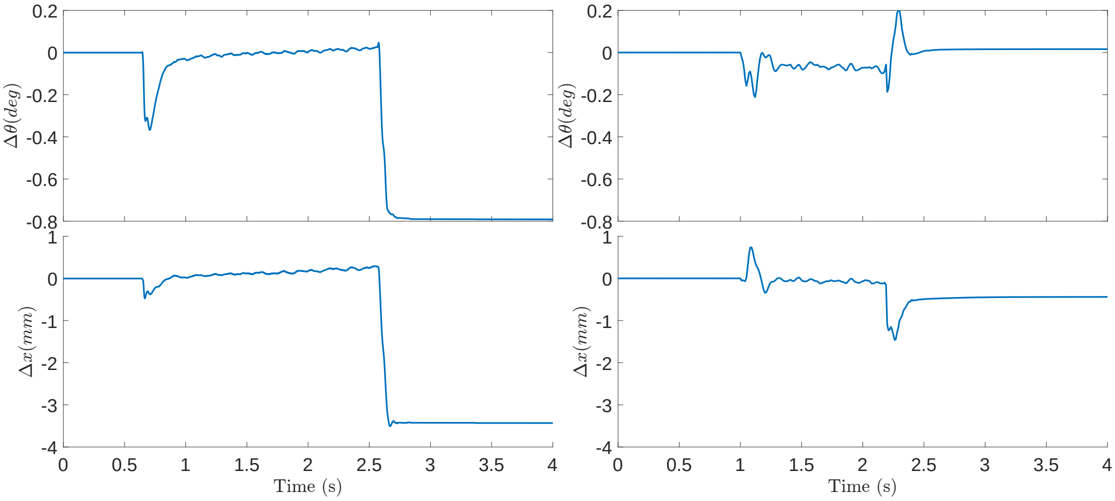

(A) With joint impedance

(B) With Cartesian impedance

FIGURE 3.28: Comparison of the deformation when contacting a hard surface at $v_{\max} = 0.1$ m.s^{-1} with impedance or Cartesian impedance. The deformation is greatly reduced with the Cartesian implementation.

3.5.4 Hybrid force/position

To verify that the proposed hybrid force/position controller would work when moving the point of contact, an experiment was done by my colleagues Saman Vafadar and Antoine Harlé with the experimental setup shown in Figure 3.29. A F/T was rigidly fixed to the robot's table (in the sole aim of measuring the contact force), and a piece of wood was attached to the F/T sensor thanks to a plastic adaptor piece. The proposed hybrid controller was then used to control the force along the z-axis to a desired F_d =10N, while the x and y axes were used for position control (So $\boldsymbol{S}_f = diag(0,0,1,0,0,0)$ and $\boldsymbol{S}_p = diag(1,1,0,1,1,1)$).s. The speed along the x-axis, $\dot{x}_{d/x}$, was set constant to 1 cm.s^{-1}, while the robot displacement on the y-axis drew a sine wave with an amplitude of 30mm at a frequency of 1Hz.

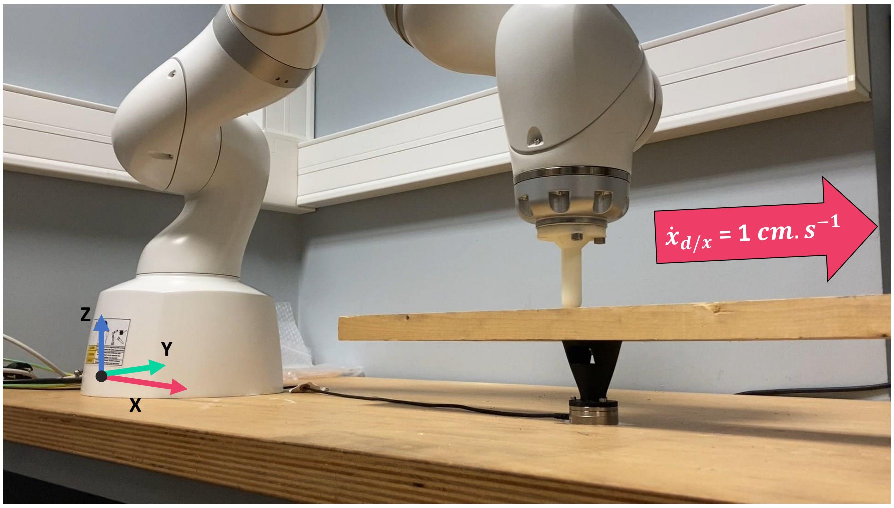

FIGURE 3.29: Experimental setup used for the hybrid force/position experiment. The tool moved normally to a wooden surface while regulating its normal interaction force.

The position-controlled movement did not disrupt the force control on the z-axis. The resulting plots in Figure 3.30 show that the contact between the plastic tool and the wooden piece during the sliding motion created high frequency noise on the force measurement f_e. This is due to the wooden surface texture. However the servoed signal $\tilde{f}_e$ remained smooth and the error between the $\tilde{f}_e$ and the desired force remained quite small (maximum error of 0.1N).

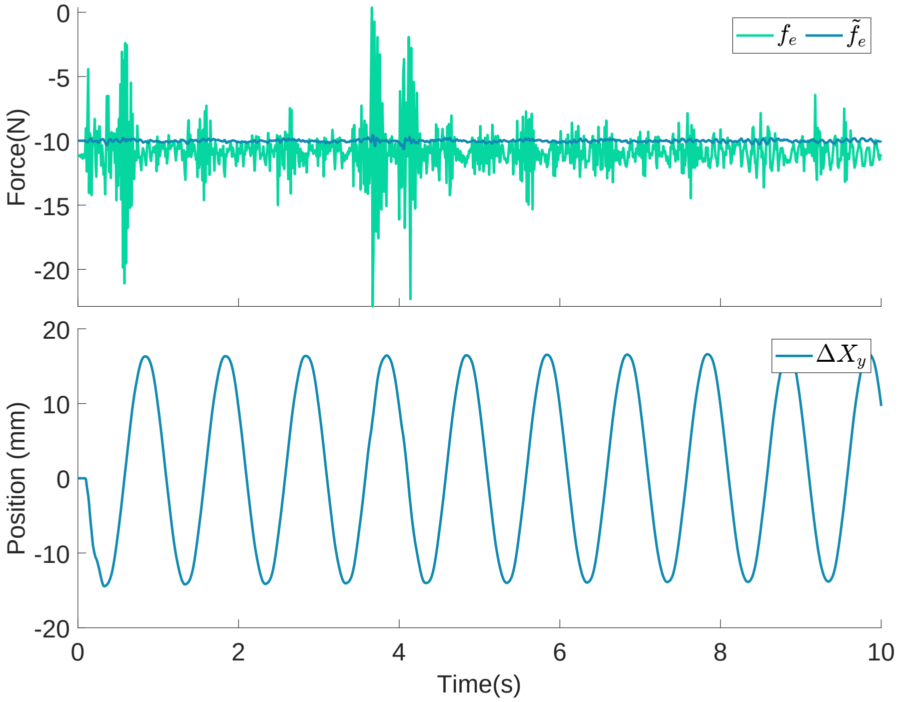

FIGURE 3.30: Behavior of the proposed hybrid position/force controller when sliding on a wooden surface while applying a constant force of $F_d = 10$N.

3.5.5 Conclusion on the Cartesian implementation

All the experiments presented in this section have demonstrated that using the pseudo-force feedback is more robust than using the conventional approach with F/T measurements. The system is stable for a wide range of the proportional gain λ. Moreover, the system is robust to the nonlinearities incoming with impacts on various environments even at high impact speeds. The tests realized prove that this controller will be stable both on soft and hard contacts.

In the case of our medical drilling application, $v_{\max}$ does not need to be as high as in the lab experiments and can be set to the max allowed drilling speed. Also, this approach allows to remove switches commonly used between force and position controllers, to first approach contact, and then regulate the interaction force.

Additionally, the implementation on the Cartesian controller corrects the coupling effect happening on the joint impedance application.

Another interesting fact coming from this approach is that the surgeon can interact directly on the tool or anywhere on the robot to lift the instrument or apply additional force if necessary. This is possible because what is regulated is only the force that the robot induces with its displacement and not the total of the forces applied at the tip of the tool. One of the downfalls of this approach is that, since the feedback is not done on real force measurements, it might not be adapted to applications where the forces have to be strictly limited to some bounds.

Conclusion

A priori, explicit force specification within the impedance control framework is only possible when the environment stiffness and position are known. Among all the control architectures found in the literature, the idea of using a pseudo-force feedback built from the position error and the desired stiffness imposed by a low-level impedance controller has been only rapidly disclosed [Stolt et al., 2012; Borghesan et al., 2012], without any robustness analysis.

The observed behavior is very robust, although the approach is straightforward in practical implementation. With the KUKA robot and its inner impedance controller, we only had to implement Equation (3.28) and tune two scalar parameters: the proportional gain λ, and the saturation velocity $v_{\max}$.

By observing the experimental results again, one may understand that the fundamental reason for the proposed approach is robustness. For experiments with a low stiffness environment, the force signal mostly contained low-frequency components, leading to a very similar behavior between the measured force feedback and the pseudo-force feedback. Indeed, in this case, $\tilde{f}_e$ can be seen as a reasonable approximation of f_e. For high stiffness experiments, when the high-frequency components of the force signal f_e became high, our approach had the advantage of not feeding them back. The signal $\tilde{f}_e$ excludes the high-frequency components. Interestingly, this is not obtained through low-pass filtering, which would add poles within the closed-loop bandwidth and induce more stability issues. It is instead obtained from the unfiltered measured and desired position signals.

The advantages of the proposed approach could also be helpful for other applications involving contact tasks such as deburring or grinding or any other application that requires applying an approximate force while also rejecting undesirable high-frequency disturbances.

Chapter 4

Automatic bone breach detection

The previous chapter has presented and evaluated a cooperative robotic system and controller for bone drilling. The following sections focus on using a bio-electrical impedance sensor embedded in the drilling instruments to detect bone breakthroughs in real-time. The intended goal of this work is to make spine surgery safer by preventing the instrument from reaching dangerous areas. This safety feature idea is tested in this chapter to stop autonomously bone drillings right at the interface between bone and surrounding tissues. A large amount of data has been collected from *ex-vivo* and *in-vivo* experiments to finally create an algorithm able to account for the variability of the anatomical model.

4.1 Using a drill bit embedding conductivity sensing

In this section, a first bone breach detection algorithm is built from anatomical knowledge and a conductivity signature analysis. Data collected from an in-vivo experiment, with a prototyped drill bit instrument embedding an electrical conductivity sensor, challenges the initial expectations.

4.1.1 Expected conductivity pattern

The two trajectories considered in this thesis, *i.e.,* pedicle and spinous process drillings, have been detailed in Section 2.2.3. Figure 4.1 compiles all the possible breaches for these desired trajectories. A correct pedicle trajectory (A) can lead only to a breach of the vertebral body, but misplaced pedicle trajectories can also induce lateral (C) or medial (B) breaches. The breach can only happen inside the vertebral canal (D) when drilling in the spinous process.

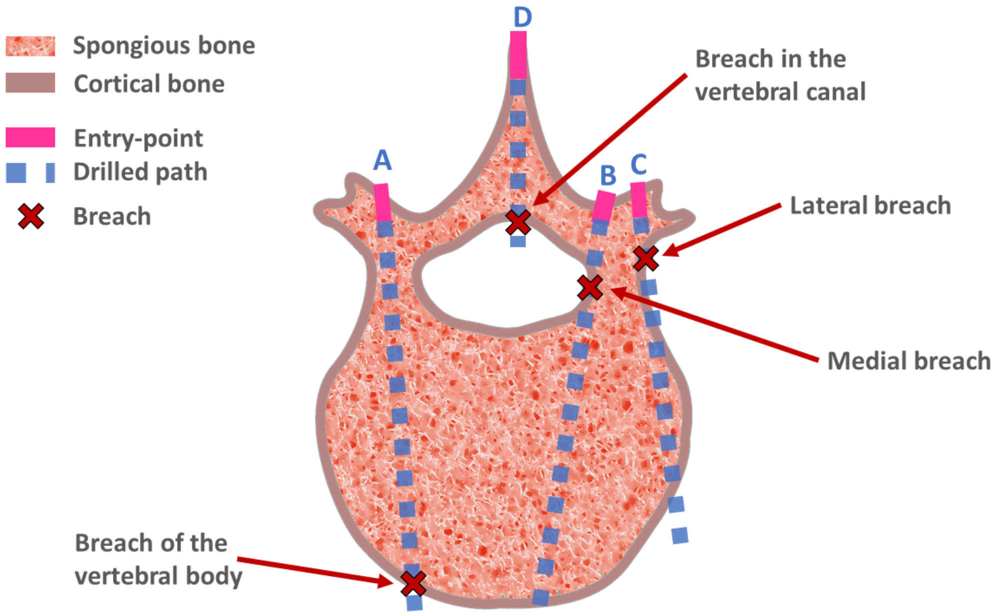

FIGURE 4.1: Possible breaches for the considered trajectories: (A) of the vertebral body, (B) medial, (C) lateral, (D) in the spinous canal.

For all the experimental drillings presented in this chapter, the first cortical bone was (partially or entirely) removed with a bone awl, as is usually done during free-handed spine surgery procedures. This manual preparation of the entry-point avoids skiving (meaning slippage of the tool on the bone) or deflection of the tool's tip when entering the bone [Crawford et al., 2020].

According to Figure 4.1, whatever the instrument's path, the instrument's tip will always pass through the same series of bone layers (see Section 1.1.1). Indeed, once the tool is positioned inside the bone, it first travels through spongious bone and finally reaches a cortical layer at some point. This is true for all considered trajectories, but the instrument might enter soft tissues either in the vertebral canal (like on trajectories (B) and (D)), or outside the vertebra(on trajectories (A) and (C)). One of the advantages of drilling in the spinous process is that a breach can only happen in the inner cortical layer that protects the spinal cord, *i.e.*, in the spinal canal, leading to more reproducible breaches.

The bone conductivity is directly related to the amount of fluid in the bone, and the signal is somehow linked to the bone density. Thus, conductivity measurements are expected to be lower in cortical layers than in spongious ones and very high when reaching soft tissues. Considering these anatomical facts and the desired paths, the conductivity signal should always draw the same specific pattern during drillings. Hence, the corresponding signature was expected to be close to Figure 4.2.

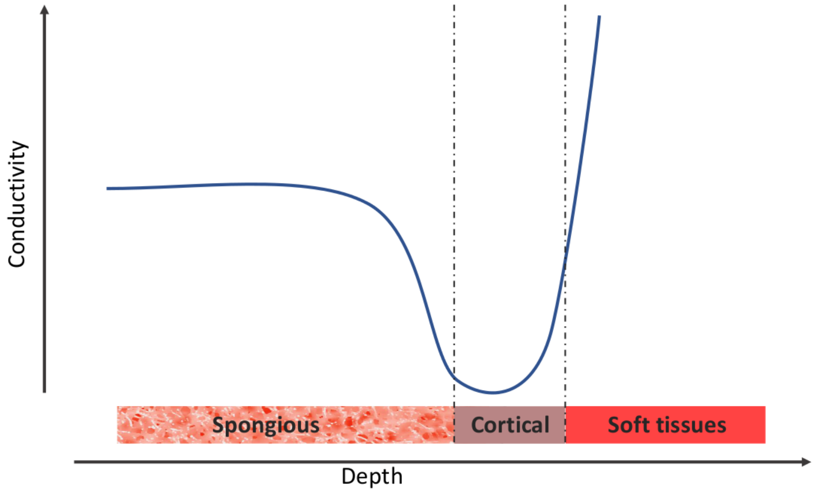

FIGURE 4.2: Expected electrical conductivity signature during bone drillings.

After the entry-point, measured conductivity values should be medium while the instrument stays in cancellous bone, then low when reaching a cortical layer, and relatively higher when breaching the outer bone layer. Interestingly, the sensor measures the conductivity a few tenths of millimeters ahead of the physical sensor tip. Indeed, as depicted in Figure 4.3, when the bone is in contact with the electrodes (inner and outer), then the current flows from the inner electrode to the outer one [Bolger and Bourlion, 2005]. The sensor, thus, will measure the conductivity of a volume of bone material that is ahead of the tip, which can allow for anticipating highly conductive soft tissues getting closer to the pyramidal shape.

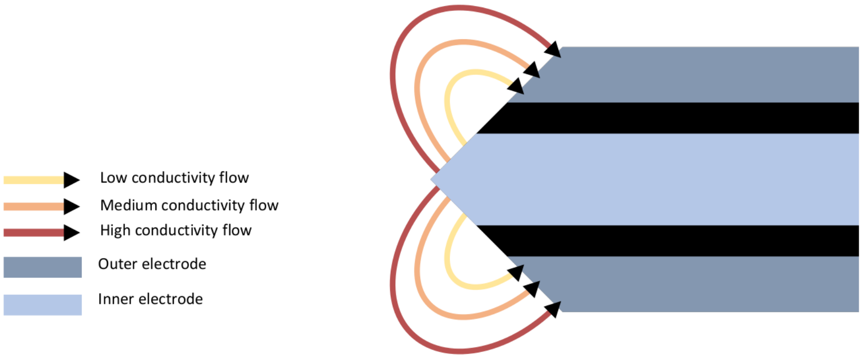

FIGURE 4.3: Electrical flow at the tip of the instrument.

4.1.2 First detection algorithm

The first version of a detection algorithm was developed from the expected conductivity signature associated with bone drilling, as depicted in Figure 4.2. The idea was to first wait for low conductivity values – describing an approach to a cortical layer – and then watch for a significant increase.

Algorithm 1 details the implementation of this detection method. It requires only the live conductivity measurements σ, and two parameters: σ_c is the low threshold value designating the instrument entering a cortical layer; $\Delta\sigma$ is the maximum allowed conductivity variations from the lowest recorded value.

Algorithm 1 First breach detection algorithm

```
    Input: $\sigma$, conductivity measurement
    Parameters: $\sigma_c$, cortical bone conductivity threshold
    $\Delta\sigma > 0$, maximal conductivity variation once $\sigma_c$ is reached
    Output: Alert, alert flag used to stop the drilling

    Cortical ← false
    Alert ← false
    $\sigma_{min} \leftarrow +\infty$
    while not Alert do
        $\sigma_{min} \leftarrow \min(\sigma_{min}, \sigma)$
        if not Cortical and $(\sigma < \sigma_c)$ then
            Cortical ← true
        end if
        if Cortical and $(\sigma > \sigma_{min} + \Delta\sigma)$ then
            Alert ← true
        end if
    end while
```

The frequency of the conductivity acquisition cadences the algorithm loop and so runs here also at 5Hz.

4.1.3 First *in-vivo* measurements

With the will to automatize the breach detection for a real-case scenario, conductivity measurements have been acquired *in-vivo* to verify if it would be possible to automatically stop bone drillings by monitoring only electrical conductivity variations. To do so, the expected conductivity signature has been compared to data collected on anesthetized pigs at the veterinary school (see details about the *in-vivo* setup in Section 2.2.2) with the preliminary robotic setup (shown in Appendix A).

Figure 4.4 shows the collected conductivity and robot displacement signals during a spinous process drilling (see Section 2.2.3), with a standard drill bit prototype (presented in Figure 2.3), at 5Hz. We can see much resemblance to the expected signature in the conductivity signal. Indeed, the signal is steady between t=5s and t=30s, corresponding to the spongious bone, then drops to low values and finally increases drastically. But we can also observe some differences: the first seconds of drilling exhibit high conductivity values due to the presence of some blood in the pre-hole; secondly, even if the tendency is relatively steady, we can observe many variations within the cancellous bone due to the inhomogeneity of bone material.

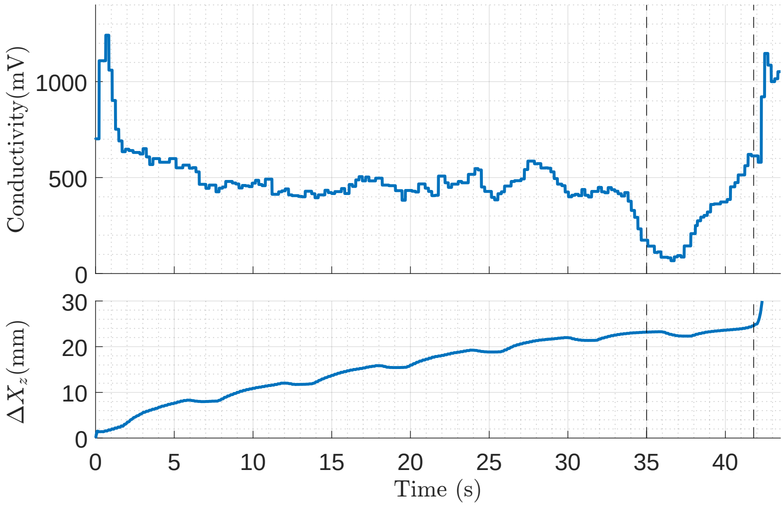

FIGURE 4.4: *In-vivo* conductivity and tool displacement measurements collected during a spinous process drilling of a pig's lumbar vertebra. This recording is pretty close to the expectations.

The tool's displacement on the z-axis, ΔX_z, shows that the insertion speed is relatively steady for the first 35 seconds, then decreases due to a more rigid bone structure. Around t=42s, a high acceleration indicates that the instrument is done piercing the bone and starts diving in the spinal canal. The oscillations observed in this plot are due to breathing. The robot follows the motion induced by breathing thanks to the proposed force control (presented in Chapter 3). The force was regulated at 10N during this experiment.

Unfortunately, some conductivity signals present fewer similarities to the presumed pattern, like those shown in Figure 4.5. For instance, in Figure 4.5A, the conductivity decrease is perturbed by an upwards oscillation around t=60s. In Figures 4.5C and 4.5D, the decrease in conductivity is less distinct than in Figure 4.4. Furthermore, Figure 4.5B is even more complicated to interpret, as the conductivity never exceeds 200 mV.

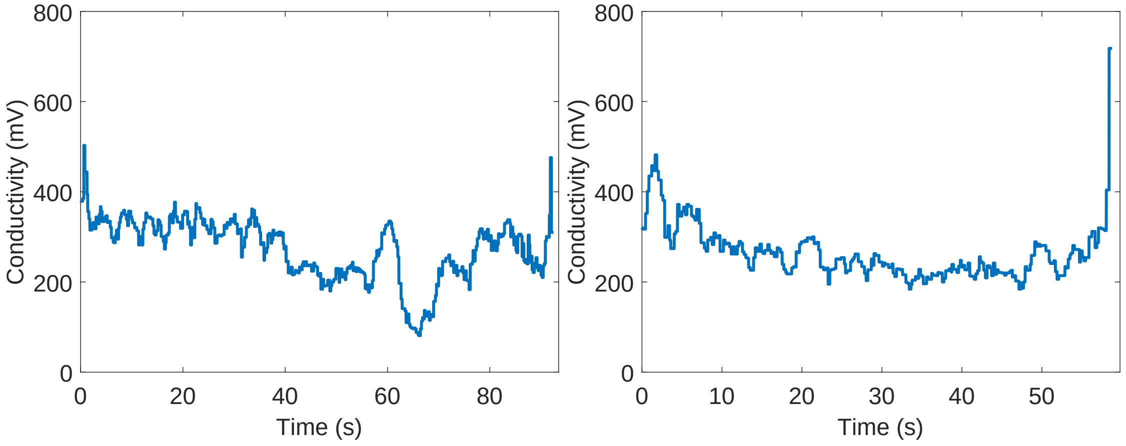

(A) L1

(B) L2

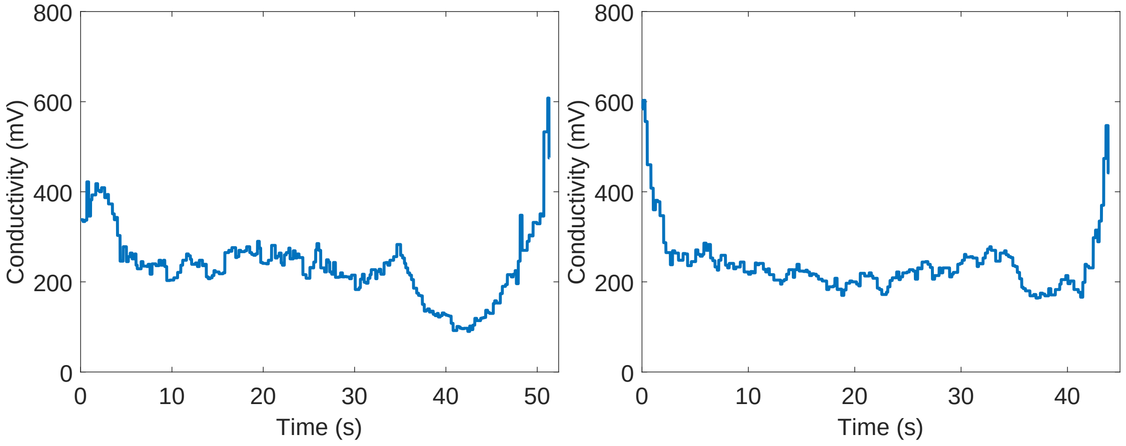

(C) L3

(D) L4

FIGURE 4.5: Variability of the electrical conductivity signals measured during spinous process drillings with the same instrument as the one used in Figure 4.4 and on different lumbar levels of the same pig.

Algorithm 1 was tested retrospectively on the data of 11 *in-vivo* drillings with different values for σ_c and $\Delta\sigma$ but led to unsatisfactory results. Indeed, the best-estimated score was 54% (6/11) of success (with $\sigma_c = 300\text{mV}$ and $\Delta\sigma = 300\text{mV}$).

This first guess algorithm was a good start but is too simplistic. In order to cope with the variability, incoming with bone porosity or patient morphology, and achieve high success rates, we need a more extensive collection of data and a more adapted algorithm.

4.2 Ex-vivo data collection

The first *in-vivo* experiments presented in the previous section could not allow for collecting a large amount of spine bone drilling data – since a pig only has 5 to 7 lumbar vertebrae, and we wanted to limit animal sacrifice to the bare minimum. An *ex-vivo* experimental setup has thus been developed to more easily gather meaningful signals in higher quantities. Then, the collected data permitted improving the breach detection capabilities by taking account of the insertion depth.

4.2.1 More data collected

The *ex-vivo* setup based on lamb vertebrae from the butcher's shop has been presented in Section 2.2.1. It allowed for executing numerous drillings without the cumbersomeness of *in-vivo* animal experimentations.

A few drillings have been performed on lamb vertebrae without the breathing machine to evaluate the lamb model individually and compare it to the porcine *in-vivo* model. Figure 4.6 shows two drillings along the spinous process path. Overall, we observed similar conductivity variations to those collected on the *in-vivo* setup. Still, the lamb bones are smaller and harder than those of pigs, leading to lower conductivity values in general.

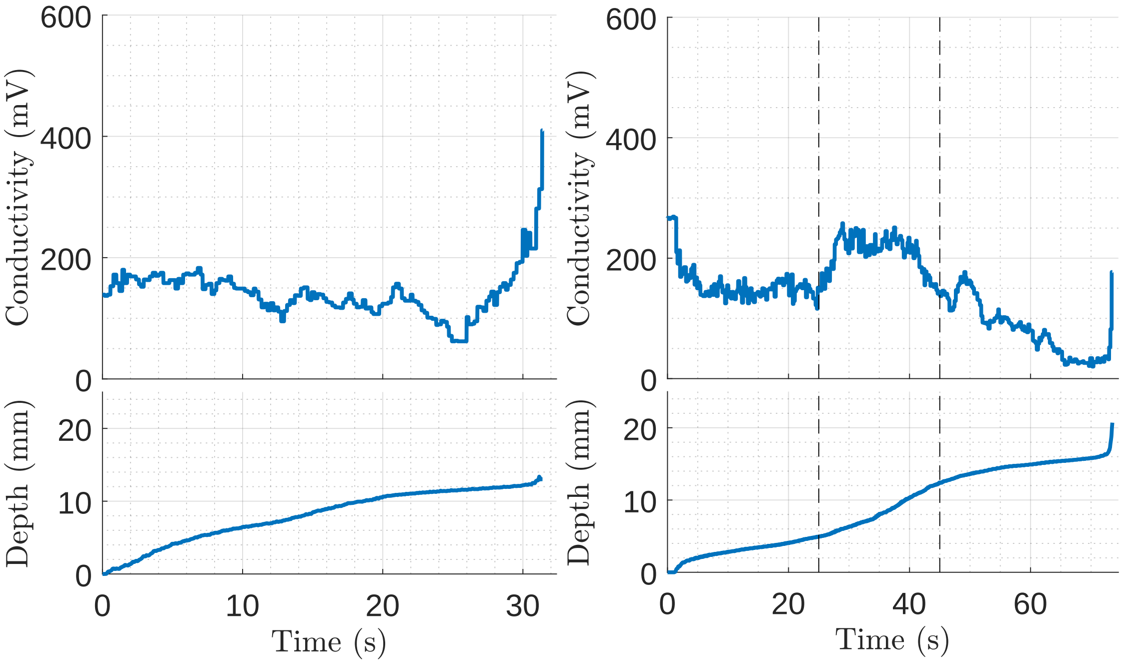

FIGURE 4.6: Sample of data collected on the ex-vivo model without the breathing simulation system.

Here, without the breathing motion or environment deformation, the robot displacement on the z-axis, ΔX_z, corresponds to the insertion depth of the tool inside the vertebra. We can see that the depth derivative can also indicate the mechanical impedance variations since the insertion speed lowers down at the end of the drillings. Moreover, we even see a correlation between the depth slope and the conductivity signal increase on this second drilling, between t=25s and t=45s.

Similar experiments have been conducted with simulated breathing to make the model more realistic. Figure 4.7 shows the resulting conductivity and robot displacement signals for 4 different drillings with vertebrae positioned on top of a machine inducing periodic displacement of a few millimeters (presented in Section 2.2.1.3).

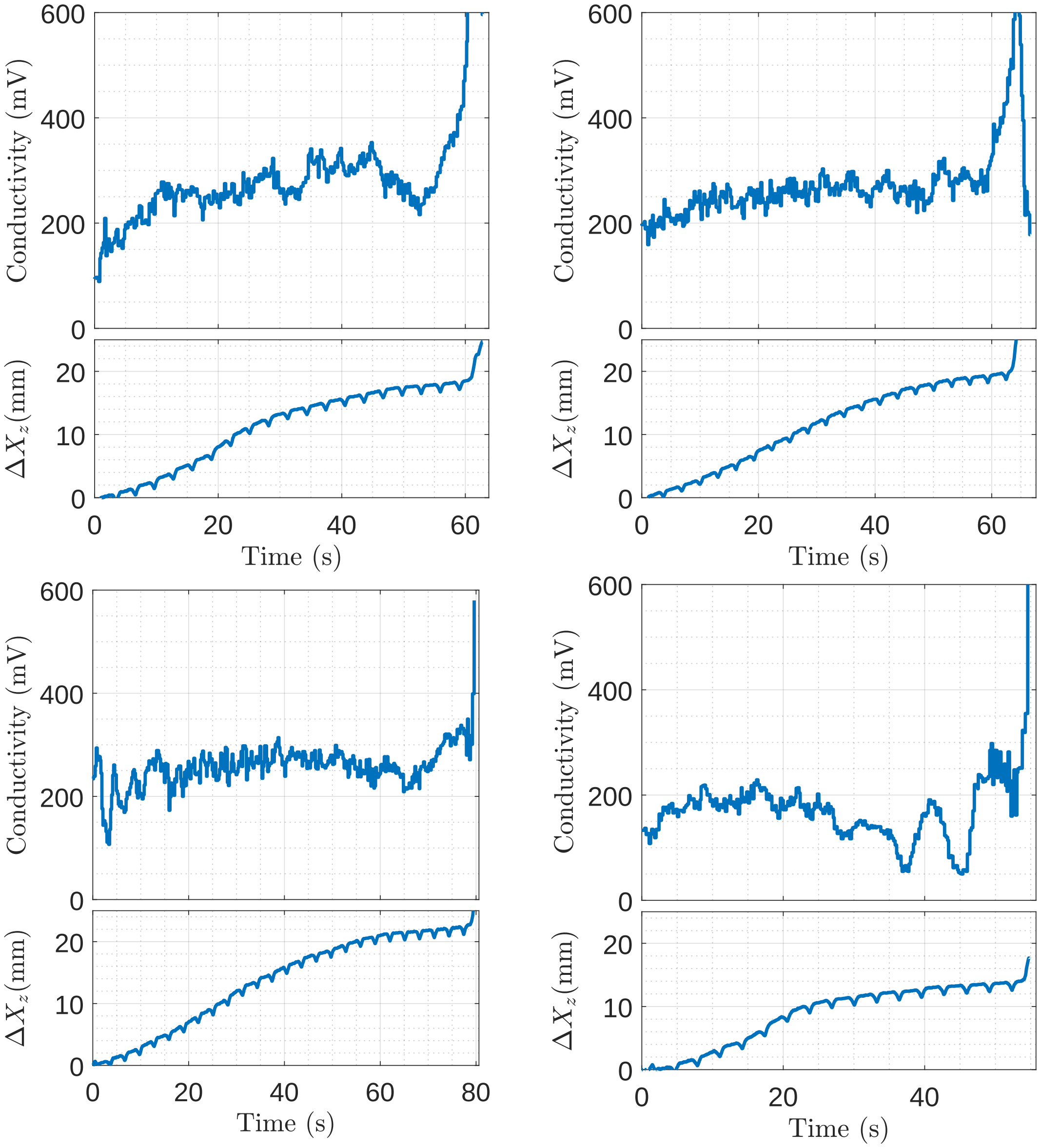

FIGURE 4.7: Sample of data collected on the ex-vivo model with simulated breathing.

Again, we get quite a lot of variability in the conductivity signals. The induced periodic displacement of the vertebra does not seem to disturb the conductivity measurements since the breathing frequency does not appear in the sensor's signal. This can be interpreted as an advantage of using a force controller that maintains constant contact conditions between the instrument's tip and the bone tissues.

4.2.2 Insertion depth estimation

In order to extract the depth information from the robot displacement, we filtered the ΔX_z signal to estimate the tool's insertion inside the vertebra. We used a moving average with a 3s-window to get a simple estimation, as shown in Figure 4.8.

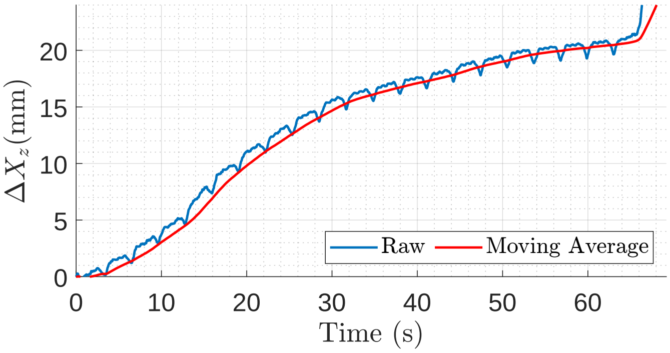

FIGURE 4.8: Estimation of the insertion depth with a moving average function.

This filtering induces delay, which is problematic, especially if we want to stop the robot by monitoring high accelerations. Since we are, in this work, focusing on the conductivity signal, this delayed depth signal was enough to improve the breach detection algorithm. Still, a work presented in Appendix D shows the premises of a proper method taking advantage of the force controller to extract the breathing motion from the tool's displacement.

4.2.3 New algorithm using the insertion depth measurements

The breach detection processing has been modified to be more versatile to cope with the variability of the measured conductivity signal. The first idea was to compute signal variations w.r.t. the depth rather than w.r.t time. This aims at amplifying signal variations when the instrument drills the cortical bone. Indeed: $\frac{\partial\sigma}{\partial t} = \frac{\partial\sigma}{\partial z}\frac{\partial z}{\partial t} \simeq \dot{z}\frac{\partial\sigma}{\partial z}$, where z is the depth. In other words, at low velocities, $\frac{\partial\sigma}{\partial z}$ is amplified w.r.t $\frac{\partial\sigma}{\partial t}$. So, the signal variations will be lowered in the spongious bone and amplified in the cortical bone where the alert is to be produced since the drilling is slowed down in this area (via the force controller).

To do so, new variables representing the maximum increase and decrease of conductivity over a depth-related window have been introduced. Moreover, the output detection flag *Alert* is now a combination of three criteria to monitor several possible scenarios simultaneously. Algorithm 2 details the implementation of each criterion:

- A_1, allows to stop if the conductivity value goes over the conductivity values usually measured on bone tissues σ_{max}.
- A_2, monitors local fast increases of conductivity $\Delta\sigma_{i2}$ over the last Δz millimeters.
- A_3, reimplements the logic of Algorithm 1 by watching decreases of $\Delta\sigma_d$ (penetrating cortical bone) followed by increases of $\Delta\sigma_{i1}$ (reaching soft tissues) on the last Δz millimeters.

Algorithm 2 Second breach detection algorithm

```
    **Inputs:** $\sigma_k$, $k$-th conductivity measurement; $z_k$, $k$-th depth measurement
    **Parameters:** $\sigma_{max}$, maximum conductivity threshold
    $d_{min}$, minimum depth to drill before detection starts
    $\Delta z$, millimeters to take into account for gradient computation
    $\Delta\sigma_{i1}$, small conductivity increase threshold
    $\Delta\sigma_{i2}$, high conductivity increase threshold
    $\Delta\sigma_d$, small conductivity decrease threshold
    **Output:** $Alert$, alert flag used to stop the drilling
    $\Sigma \leftarrow [\Sigma\ \sigma_k]$, $Z \leftarrow [Z\ z_k]$                ▷ Constructing lists
    if $z_k > d_{min}$ then
        $A_1 \leftarrow \sigma_k > \sigma_{max}$
        $m \leftarrow \underset{i \in \{1 \cdots k\}}{\operatorname{argmin}} |Z(i) - (z_k - \Delta z)|$
        $n \leftarrow \underset{i \in \{m \cdots k\}}{\operatorname{argmin}} \Sigma(i)$
        $A_2 \leftarrow \left( \left( \max_{i \in \{n \cdots k\}} \Sigma(i) \right) - \Sigma(n) \right) > \Delta\sigma_{i2}$
        $A_3 \leftarrow \left( \left( \max_{i \in \{m \cdots n\}} \Sigma(i) \right) - \Sigma(n) \right) > \Delta\sigma_d$ and $\left( \left( \max_{i \in \{n \cdots k\}} \Sigma(i) \right) - \Sigma(n) \right) > \Delta\sigma_{i1}$
        $Alert \leftarrow Alert$ or $A_1$ or $A_2$ or $A_3$
    end if
```

To try Algorithm 2 in real difficult conditions, the algorithm was tested on data collected on the ex-vivo setup with the simulated breathing (an approximative breathing period of 3s). The retrospective application of this algorithm on 17 drillings, with many sets of parameters, returned a maximum success rate of 94% (16 successes and 1 false-positive) with the parameters of Table 4.1.

One inconvenience of this new implementation of the breach detection algorithm is that there are six different parameters to tune. Moreover, this method showed to be highly sensitive to the tuning of its parameters, as adjusting slightly one of the parameters

σ_{max}	500 mV	d_{min}	5 mm
Δz	1.5 mm	$\Delta\sigma_{i2}$	160 mV
$\Delta\sigma_{i1}$	140 mV	$\Delta\sigma_d$	120 mV

TABLE 4.1: Best selection of parameters for Algorithm 2 on the ex-vivo model with the standard drill bit prototype, leading to a 94% success rate on 17 lamb vertebrae.

can create more false positives (too early: stops more than 2mm before the interface) or false negatives (too late: stops more than 2mm after the interface).

Furthermore, even with these optimized parameters, we have observed that sometimes the detection was triggered after the robot had started cracking the cortical bone. Algorithm 2 thus tended to actuate the security stop a bit late after the tool started accelerating its course towards the spinal canal. For instance, in Figure 4.9, we can see with the ΔX_z signal that the robot starts accelerating around t=78.7s and would be stopped by the breach detection algorithm at t=79.2s. In that short lapse of time, the robot would have had the time to move by 1.3mm.

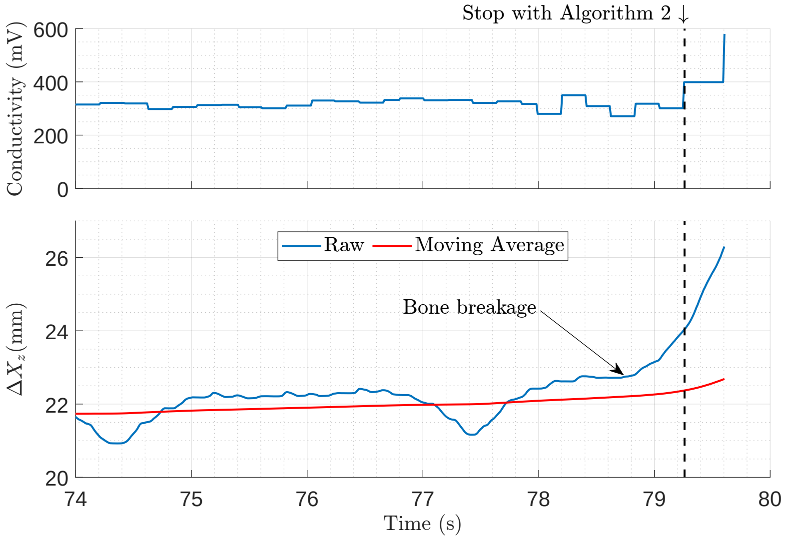

FIGURE 4.9: Example of a late stop with Algorithm 2 showing the tool can quickly accelerates after bone breakage.

In the following, in order to prevent accelerations once the cortical bone starts breaking, we will try to:

1. Get more frequent measurements to increase the reactivity of the breach detection. Indeed, since the sensor returns the conductivity signal at only 5Hz, then the worst reaction time so far was 0.2s.

2. Modify the instrument to make it mechanically safer, by preventing it from diving into the spinal canal when the bone is fractured, and the detection is late.

4.3 Adapting the instrument to robotic breach avoidance

From now we will be using the improved experimental setup presented in Chapter 2, and switching from the standard drill bit to the threaded instrument; Which presents the following mechanical advantages for the automation of pedicle screws placement:

1. The helical link between the bone and the drill created by the threads allows to completely control the insertion speed with the rotation speed. Thus, the robot will not dive if the bone is breached. In other words, the axial force needed to compensate for breaking the bone is not a danger anymore w.r.t. breaching.
2. Once the first thread is attached to the bone, the insertion depth of the tool can be directly computed from the number of rotations of the instrument.
3. The contact between the sensor at the tip of the instrument and the bone is guaranteed as the instrument is screwed into the bone.

From then, with the new threaded instrument, the conductivity image in milli-volts will be measured at 25Hz, which impacts the measurements. Thus, the following conductivity signals can not be directly compared to the previous measurements at 5Hz due to changes in electronics and instrument shape.

Data over a hundred drillings using this threaded instrument was collected with the same experimental conditions to create a representative database. Furthermore, all the following experiments used the improved robotic setup presented in Chapter 2. From this data, a newer breach detection algorithm was deduced that could have stopped all drillings in proximity to the bone limits.

4.3.1 Qualitative breach data

In order to collect more qualitative data on bone breaches, several improvements to the *ex-vivo* setup have been made. The complete setup, shown in Figure 4.10, comprises several components that were detailed in Chapter 2:

1. A robotic arm pre-certified for medical applications.
2. A self-made velocity-controlled power drill allows to measure simultaneously the cutting torque during drillings.
3. A threaded cutting instrument embedded with a conductivity sensor at 25Hz.
4. A transparent box with a clamping device allows fixing the vertebra while immerging the vertebral canal with a saline conductive solution.
5. A camera recording the interior of the vertebral foramen.

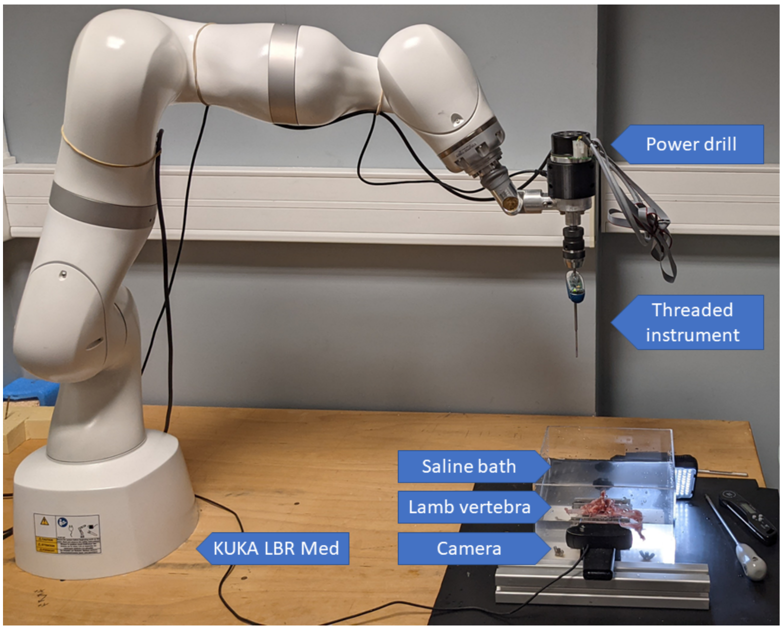

FIGURE 4.10: *Ex-vivo* experimental setup comprising a medically certified robotic arm, a velocity-controlled power drill, a threaded instrument with conductivity sensing, a camera, and a lamb vertebra in a saline bath.

With this setup, we were able to synchronously measure the robot's displacement, bone conductivity, and cutting torque while recording a video of the instrument breaching out from the bone.

The videos were then watched frame by frame to determine precisely when the instrument started breaking the bone surface. As explained in Figure 4.11, we considered the first visible deformation inside the vertebral canal to be the beginning of the bone breakage. Since the recordings were at 30 FPS (frames per second), the time precision

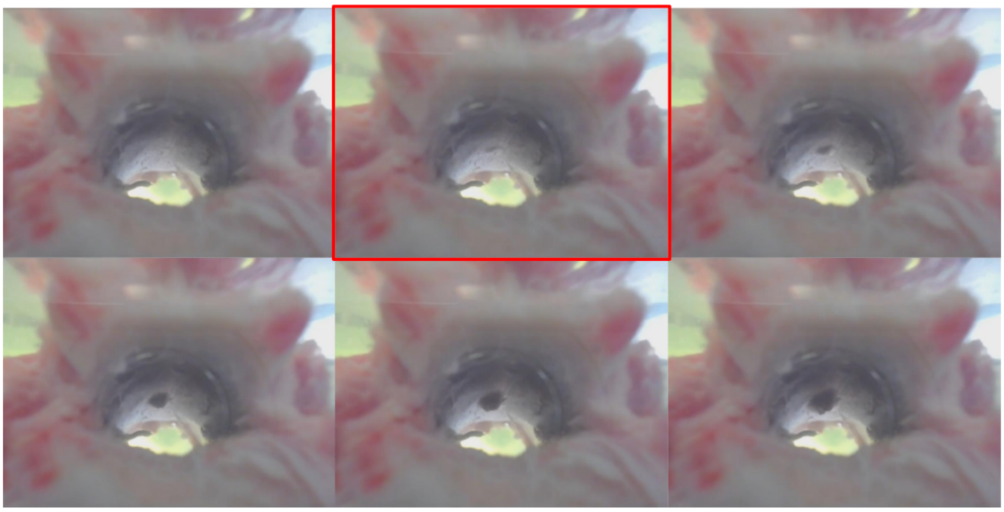

FIGURE 4.11: Visualization of the bone deformation and breach inside the vertebral when using the threaded instrument. The image framed in red corresponds to the timestamp when we consider that the tool starts leaving the bone.

of this instant is 33 ms. The associated timestamp was then used to report the ideal stopping time for the breach detection algorithm on the sensors' plots. From that timestamp, and thanks to the insertion depth signal, an acceptable stopping zone of ±2 mm around the breach instant was constructed. This limit was chosen to allow only grades A and B of the Gertzbein-Robbins classification [Gertzbein et al., 1990] for pedicle screw placement and to ensure that we stop close to the interface.

Figure 4.12 shows an example of data collected from one drilling. This time, we can see that the robot's velocity, *i.e.,* the insertion speed within the bone is controlled and steady after a few seconds, thanks to the threads on the instrument. The electrical conductivity variations are similar to those collected with the drill bit prototype in Section 4.2. The reported timestamp – indicating the instant when the inner cortical bone starts being deformed – corresponds most of the time to a local minimum of the conductivity signal. Also, the cutting torque, which is derived from the power drill's electrical current signal, is informative as well since the breach instant seems to correspond to the maximum of the torque signal. However, we decided not to use this information in order to check if conductivity alone could be sufficient.

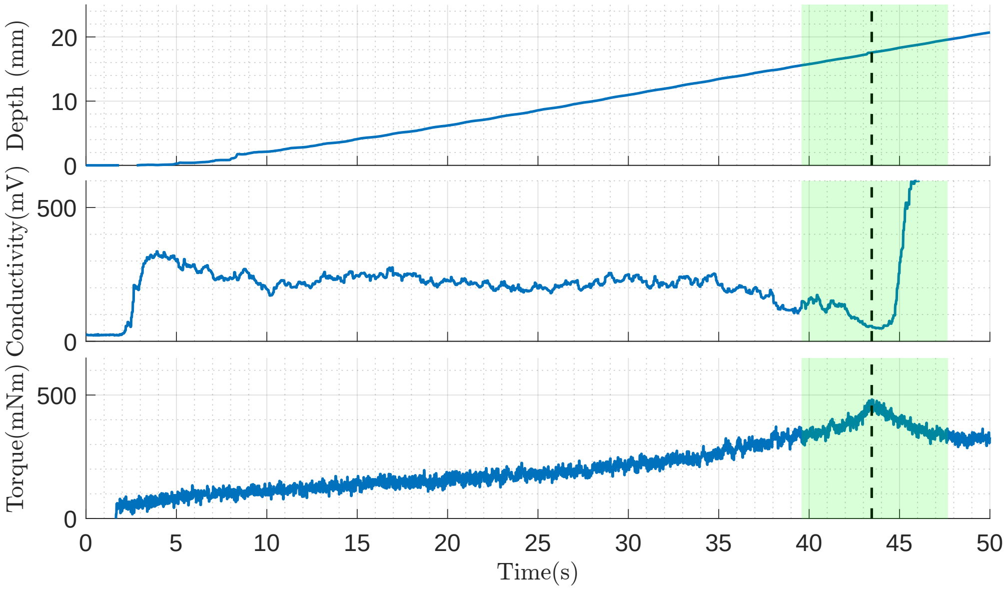

FIGURE 4.12: Example of data collected with the improved setup. The dashed line indicates the time instant when the bone starts to break. The green area represents the safe stopping zone of ±2mm constructed around this timestamp.

4.3.2 Quantitative drill-through data collection

In order to generate a quantitative database of these qualitative breaching signals in the spinal canal, the *ex-vivo* setup mentioned above was used for the continuous drilling of 100 lamb lumbar vertebrae with the same instrument. The rotation speed of the motor was servoed to $\omega = 30$rpm, leading to an insertion speed of 0.5 mm/s. The force controller of Chapter 2 was used with a desired control force $F_d = 10N$. In practice, thus, force control is useful for breath compensation in an *in-vivo* setup, but also for the initial penetration of the threaded drill: until a few threads are anchored in the bone.

Figure 4.13 shows a sample of the collected data. Like with the first experiments using the standard drill bit prototype (Figure 4.7), the conductivity signals show a lot

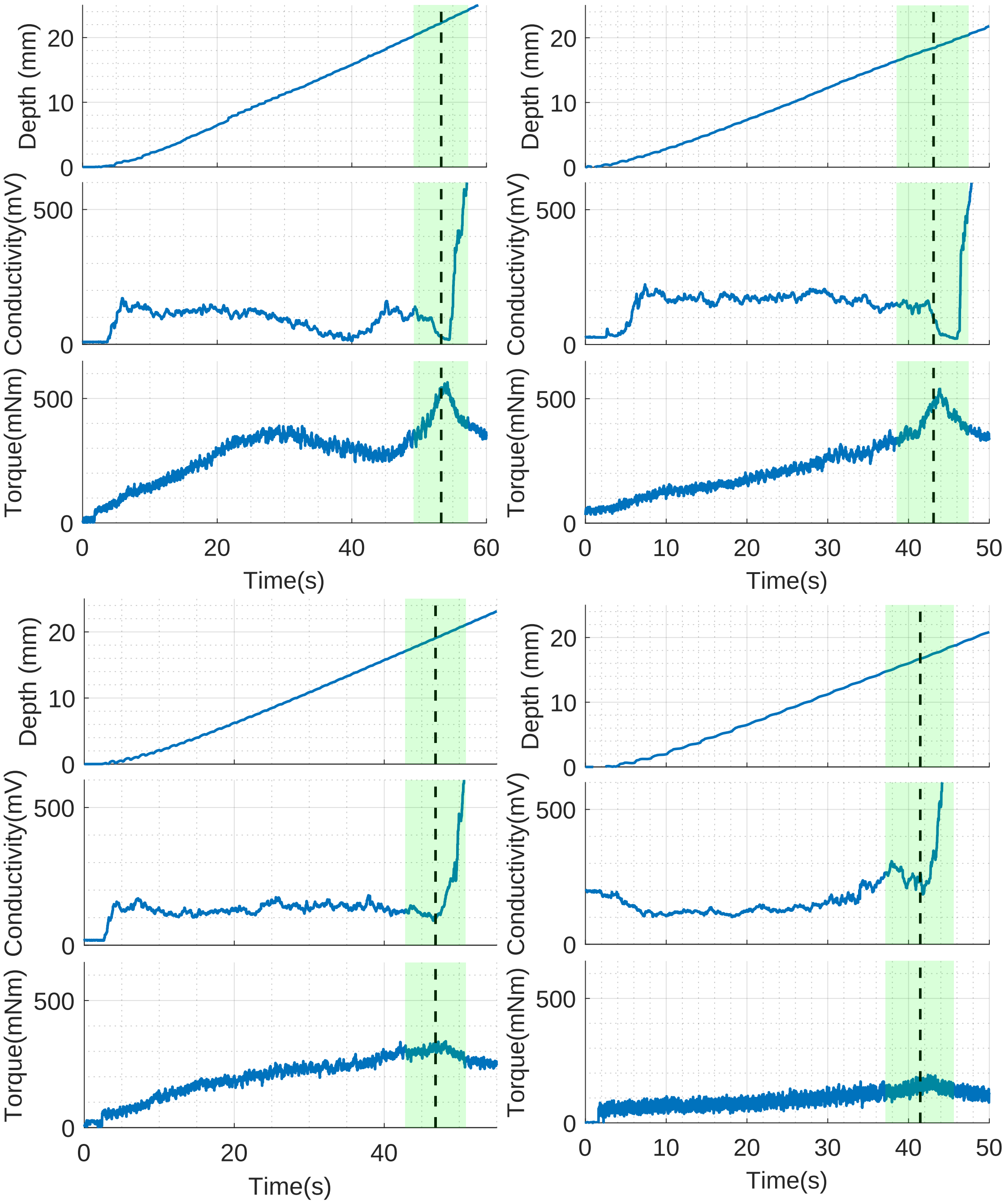

Figure 4.13: Sample of drill-through data collected with the threaded instrument on the ex-vivo model. The conductivity and cutting torque signals still show a lot of variability from one vertebra to the other.

of variability between drillings. This also appears to be the case for the torque measurements.

4.3.3 Improved detection algorithm

The detection algorithm was modified from observations made on the newly collected data and the behavior of the previous Algorithm 2.

First of all, we realized that the conductivity would not decrease when approaching the inner cortical bone for half of the recordings. So we decided to remove the criterion (alert A3) that watched decreases in conductivity, as it mainly created false positives.

Secondly, right after the breach, the conductivity values are pretty high and usually higher than the values measured near the entry-point. To reflect this fact in the breach detection, we kept the idea of the high threshold parameter introduced for Algorithm 2 (alert A1) but made it self-tuned (with the α parameter) from the conductivity measurements collected after the entry-point (when $z \in [d_{min} - \Delta z, d_{min}]$).

Moreover, the increases in the conductivity are even more explicit than the high values themselves. Most of the time, the transition from the cortical bone to the outer tissues is abrupt and easy to interpret visually. That's why the A_2 criterion was kept from Algorithm 2 to 3.

The resulting breach detection function is based on two independent criteria whose computations are detailed in Algorithm 3. The algorithm only requires an estimation of the insertion depth and the conductivity measurement.

The parameter σ_{max} value was chosen as small as possible while not creating any false-positive in cancellous bone. Then, the α parameter was selected with the same process. Overall, they allowed the criteria A_1 to stop in the ±2mm zone in 97% of the cases with $\sigma_{max} = 500$mV and $\alpha = 2.4$.

The parameters Δz and $\Delta \sigma_i$ were optimized together to stop the closest to the -2mm limit. The best result was obtained *a posteriori* with $\Delta z = 2$mm and $\Delta \sigma_i = 230$mV, which gave a 99% success rate.

Together, with the optimized parameters for each criterion, the two flags could have stopped the 99% of the drillings in the safe zone, with a 0.70mm mean around the exact bone limit and a standard deviation of 0.52 mm.

Algorithm 3 Third breach detection algorithm

```
**Inputs:** $\sigma_k$, $k$-th conductivity measurement
$z_k$, $k$-th depth measurement
**Parameters:** $\sigma_{max}$, maximum conductivity threshold
$\alpha$, gain for the adaptable conductivity threshold
$d_{min}$, minimum depth to drill before detection starts
$\Delta z$, millimeters to take into account for gradient computation
$\Delta\sigma_i$, small conductivity increase threshold
**Output:** Alert, flag used to stop the drilling

$\Sigma \leftarrow [\Sigma\ \sigma_k]$, $Z \leftarrow [Z\ z_k]$                ▷ Constructing lists

if $z_k < d_{min}$ then
    $Alert \leftarrow$ false
    if $z_k < d_{min} - \Delta z$ then
        $j \leftarrow k$
    else
        $\sigma_r \leftarrow \frac{(k-j-1)\sigma_r + \sigma_k}{k-j}$
    end if
else
    $A_1 \leftarrow \sigma_k > \min(\sigma_{max}, \alpha\ \sigma_r)$
    $m \leftarrow \underset{i\in\{1\cdots k\}}{\operatorname{argmin}} |Z(i) - (z_k - \Delta z)|$
    $n \leftarrow \underset{i\in\{m\cdots k\}}{\operatorname{argmin}}\ \Sigma(i)$
    $A_2 \leftarrow \left(\left(\max_{i\in\{n\cdots k\}} \Sigma(i)\right) - \Sigma(n)\right) > \Delta\sigma_i$
    $Alert \leftarrow Alert$ or $A_1$ or $A_2$
end if
```

4.4 Final experimental results

To validate experimentally the efficacy of Algorithm 3 to prevent bone breaches in real-time, the new breach detection algorithm was tested both in *ex-vivo* and *in-vivo* active experiments.

The robot control, materials, and methods were the same in both scenarios. A pre-hole was manually made with the bone awl in the vertebra's spinous process. Then, at the beginning of the procedure, the hybrid position/force controller was used to allow cooperation between the surgeon and the robot to position and orient the instrument properly at the entry-point. To do so, all Cartesian axes were force-controlled to null forces/torques ($\boldsymbol{S}_f$ = diag(1,1,1,1,1,1) and $\boldsymbol{F}_d = 0$) with deadzones, in a first phase. Once positioned in the entry-point, the controller was then used with a constant tip position and zero desired moment ($\boldsymbol{S}_f$ = diag(0,0,0,1,1,1)), allowing only to orient the instrument towards the spinal canal. Next, with a simple click on a GUI, the deadzones are removed and the force controller is used to apply a constant force of F_d=10N along the tool's axis ($\boldsymbol{S}_f = \text{diag}(0,0,1,0,0,0)$). Finally, another click started the drilling algorithm at a constant rotation speed ($\omega = 30$rpm) leading to an equivalent feed rate of $v_{des} = 0.5$mm/s, along with the breach detection process.

4.4.1 Ex-vivo (lamb)

The same setup as the one used for data collection of breaches was employed to test Algorithm 3 in action on 104 *ex-vivo* lamb vertebrae (see Figure 4.14). The parameters chosen for the breach detection were the same as those identified from the *ex-vivo* data collection (see Table 4.2).

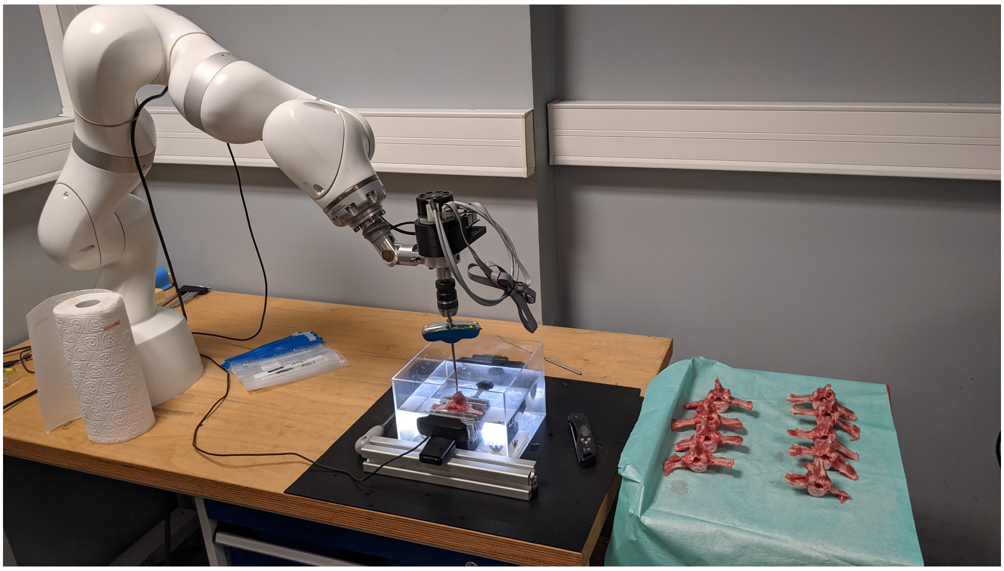

FIGURE 4.14: Setup used for the *ex-vivo* experimentations to validate Algorithm 3.

The 104 drillings were all automatically stopped. More importantly, after each drilling, a surgeon has verified via palpation with a ball-tip feeler that the instrument did not fully breach outside the bone. Moreover, the video feed recorded from the camera allowed us to visually verify that the instrument did not entirely pass the vertebral wall (see Figure 4.15B). This confirmed that they were no false negatives and that none of the drillings were breached entirely.

σ_{max}	500 mV	α	2.4
Δz	2 mm	$\Delta\sigma_i$	230 mV
d_{min}	5 mm		

TABLE 4.2: Parameters of Algorithm 3 optimized and used for the final *ex-vivo* drilling study on 104 vertebrae that were all stopped in a ±2mm zone around the interface separating the bone from the spinal canal.

Additionally, a post-operative CT scan analysis confirmed that all drillings were stopped within less than 2mm from the bone interface – so they were no false positives. Moreover, a few vertebrae were passed through a micro-CT scanner to better visualize the resulting hole drilled inside the spinous processes (see Figure 4.15C).

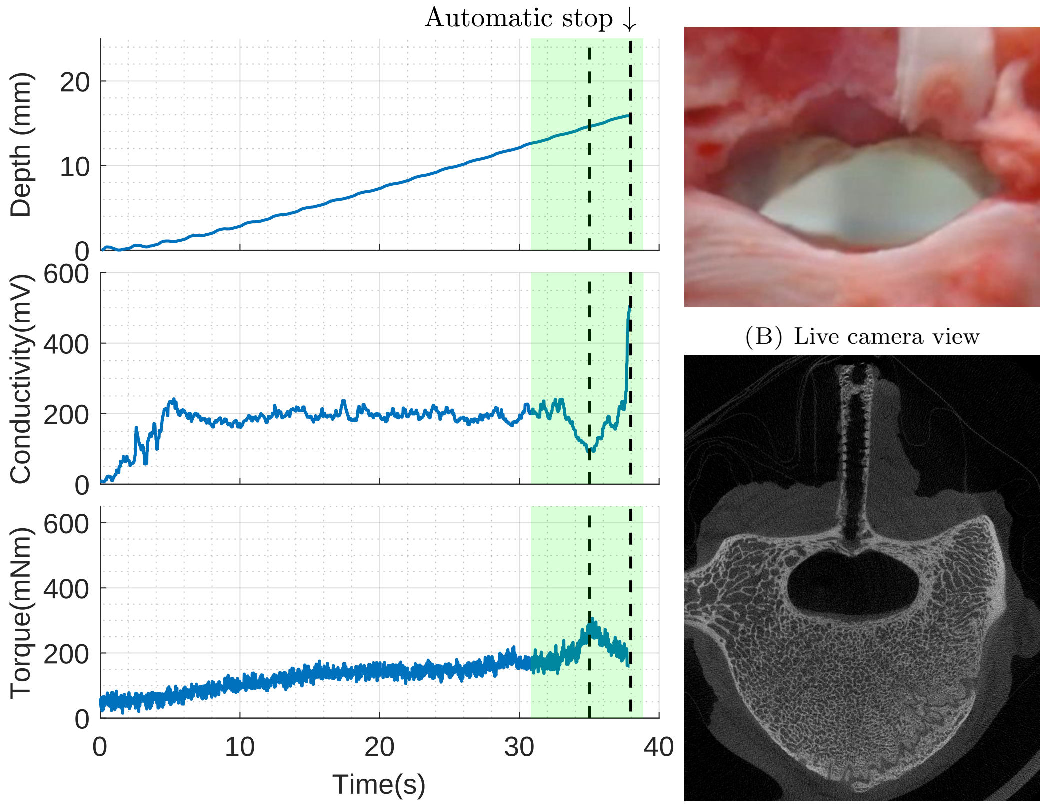

(A) Collected signals in function of time

(B) Live camera view

(C) Post-op micro-CT scan

Figure 4.15: Data collected from one autonomously drilled lamb vertebra. (A) Depth, conductivity, and cutting torque live signals in function of time. The green area represents the acceptable stopping zone. (B) Image captured at the end of the drilling, showing that the bone is pushed inside the vertebral canal. (C) Post-operative micro-CT scan of the vertebra illustrating a small crack of cortical bone, but no actual breach.

The post-processing of the synchronized robot logs and webcam videos permitted to position, again, a safe stopping zone on the graphs (shown in green in Figure 4.15A). This allowed quantifying the displacement made once the bone was pushed inside the vertebral canal. A CT scan measurement was used instead for some drillings where no bumps were visible on camera. In those rare cases, the distance from the interface appeared to be really small and was considered null. The results for the 104 vertebrae are condensed in a histogram in Figure 4.16. On average, the stopped drillings pushed 0.65 mm of bone in the vertebral canal, with a standard deviation of 0.4 mm.

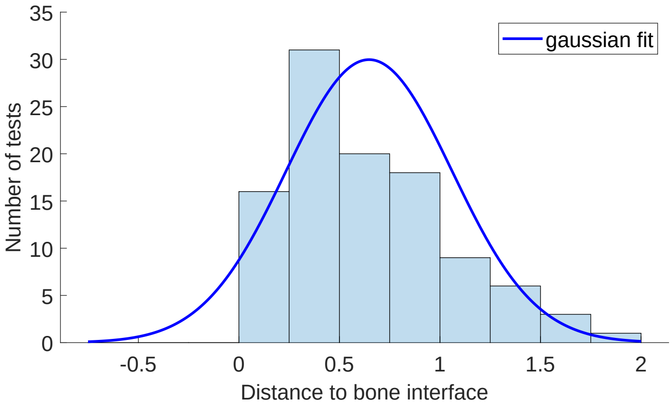

FIGURE 4.16: Histogram of the resulting distances to the bone interface for the 104 automatic stops of the quantitative study using Algorithm 3 and the threaded drill bit.

4.4.2 In-vivo (pig)

Finally, the breach detection Algorithm 3 was also tested *in-vivo* on the lumbar vertebrae of a living pig (Figure 4.17). Please note that the insertion depth was here estimated from the rotation of the threaded instrument since the ΔX_z signal here includes the breathing motion.

FIGURE 4.17: Experimental setup at the veterinary school to test automatic drillings with Algorithm 3 and the threaded drill bit on a living pig.

Two initialization trials (manually stopped) were performed in L5 and L6 in order to measure breaches with the new setup and adapt the parameters of Algorithm 3 to this new anatomical model. Indeed, thanks to the previous *in-vivo* experiments, we expected living pig bones to behave differently from ex-vivo lamb bones. α, being hard to tune without numerous trials, was not used on the *in-vivo* conditions (so $\alpha \to \infty$). d_{min} was not changed, and Δz rounded to 2mm. σ_{max} and $\Delta \sigma_i$ were then tuned so that they would have both triggered their associated Alert criterion (A_1 or A_2) on the two trials. The parameters used for the *in-vivo* experiments are displayed in Table 4.3.

σ_{max}	400 mV	d_{min}	5 mm
Δz	2 mm	$\Delta \sigma_i$	200 mV

TABLE 4.3: Parameters used for the final *in-vivo* experiments with Algorithm 3.

Then, 4 drillings were performed in the spinous process of the pig (from level L4 to L1), for which the robot stopped automatically. In these 4 experiments, 2 were stopped thanks to the A_1 criterion, and the other 2 with A_2. After each drilling, the integrity of the drilled path was checked with a ball-tip feeler, revealing that there was still some cortical bone left. A post-operative scan of the four vertebrae confirmed that the instrument's tip did not penetrate the spinal canal fully. Leading again to a 100% success rate, but only with 4 drillings.

Figure 4.18 shows the signals measured when drilling the L1 vertebra, and the associated CT image of the resulting hole in the spinous process. Data for the four *in-vivo* drillings are shown in Appendix E.

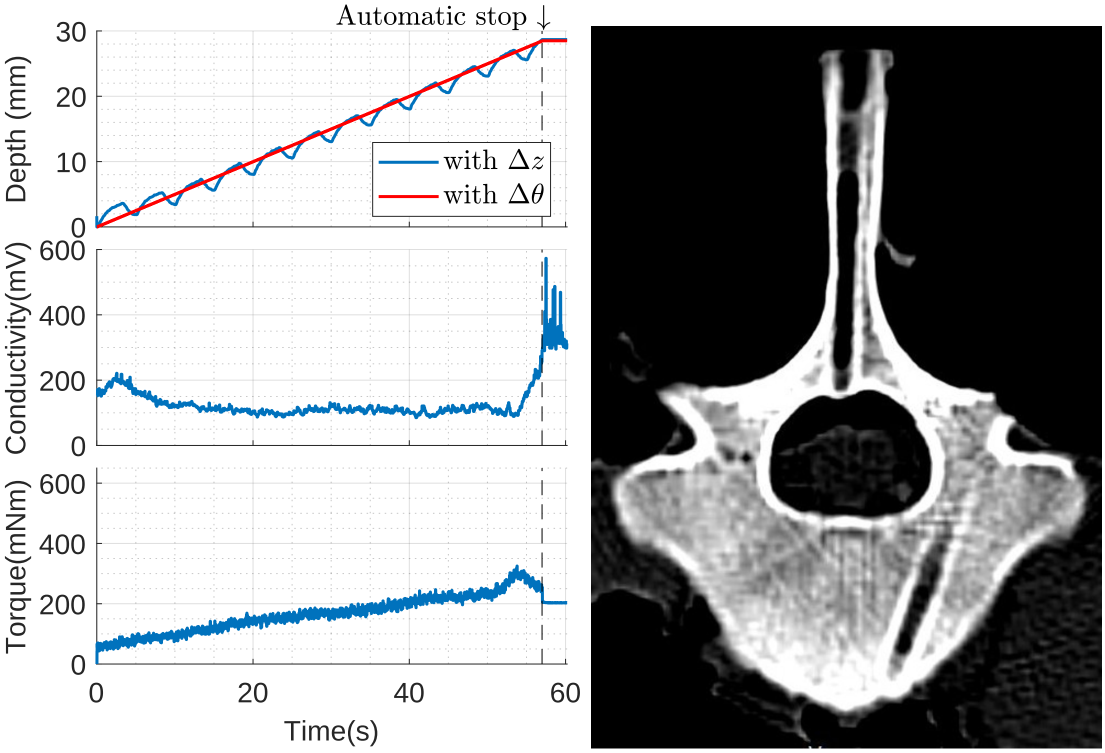

(A) Real-time measured data (B) Post-operative CT scan

FIGURE 4.18: Automatic stop performed *in-vivo* with Algorithm 3 (with parameters of Table 4.3) and the threaded drill bit prototype in the spinous process of a lumbar pig vertebra. (A) Depth, conductivity, and cutting torque live signals in function of time. (B) Post-operative CT scan shows no actual breach.

The displacement induced by the pig's breathing is similar to the ones seen in the first *in-vivo* experiments. But this time, the overall insertion speed is constant due to the nature of the new instrument. The breathing does not affect the conductivity signal since no low-frequency oscillations appear in the conductivity measurements. On average, the required cutting torque was lower than for the *ex-vivo* lamb experiments but showed the same dynamics in this model.

This quick experiment showed that even with very little data, the parameters for Algorithm 3 could be adapted for *in-vivo* and allow for stopping on time in real operating conditions.

4.4.3 Conclusion on experiments

The CT scans and the recorded videos *ex-vivo* showed that the detection happens when the cortical bone starts to crack, i.e., before the hole is thoroughly drilled. The videos of the preliminary experiment also allowed us to visualize the bone deformation (bump) happening in the vertebral canal before bone perforation.

All the drillings of the *ex-vivo* and the *in-vivo* experiments were graded A or B with the Gertzbein-Robbins classification, which is clinically acceptable. In comparison to articles in the literature evaluating the performances of current robotic systems, they can only give the ratio of wrongly placed pedicle screws during actual surgeries, or the precision of placement with respect to a pre-operative plan. This is not the same as when intending to voluntarily target the spinal canal and stop. Moreover, notice that in our experiments, the trajectory (via the spinous process) used was perpendicular to the spinal canal, which corresponds to a worst-case scenario in terms of penetration – compared to medial or lateral breaches happening during pedicles drillings.

These preliminary results are very encouraging but still need to be reproduced on a quantitative in-vivo setup to ensure the transferability to a living model. Moreover, future work will need to be validated on actual pedicle trajectories, not spinous processes. Furthermore, the method needs to be confronted with a human model for validation. To that end, a non-robotized study was performed at the Trousseau hospital to collect conductivity signals associated with human pedicle preparations. Dr. Raphaël Vialle, Elie Saghbiny, and Célia Chaimi used the medical pedicle probes commercialized by SpineGuard (PediGuard DSG Connect), to collect conductivity measurements during scoliosis corrections [Saghbiny et al., 2022].

Conclusion

With the idea to provide an additional online safety check for robotized spine surgery, a breach detection algorithm using electrical conductivity and an estimated insertion depth measurement was developed from hundreds of *ex-vivo* measurements on lamb lumbar vertebrae drillings.

A quantitative study of 104 experimental drillings was performed on *ex-vivo* lamb vertebrae and got a 100% success rate. All the drillings were autonomously stopped at the interface (± 2mm) between the bone and the spinal canal. This success was confirmed *in-vivo* in a veterinary operating room on a living pig on 4 lumbar vertebrae.

These results are really promising and are of great interest for the future of robotic spine surgery. Furthermore, we believe that electrical conductivity could also prove helpful for other types of orthopedic surgeries.

Chapter 5

Conclusion

The interest in new solutions for surgical robotics is still high after three decades of research and innovation. Research laboratories and companies worldwide team up to develop new robotics tools to improve surgical workflows. But, to be further accepted by the medical community, surgical robots need to prove that they bring additional features, compared to the classical tools currently used in the operating room. A crucial issue is to improve the surgical outcomes for the patients.

In spine surgery, accuracy and safety are the key elements. Because of the proximity to the spinal cord, errors of a millimeter could lead to irreparable neural damage, paraplegia, or even death. For this reason, many patients suffering from back problems will never be operated on, as some surgeries are considered too risky relative to the potential benefits for the patient.

We consider the contributions in this thesis as steps towards safer spine surgery and future automation of pedicle screw placement.

5.1 Summary of the contributions

The mid-term goal of this research was to develop a robotic system able to automatically and safely insert pedicle screws in a vertebra without the use of X-ray imaging devices but by monitoring the bio-electrical conductivity of the bone tissues along the trajectory. Indeed, safety checks in spine surgery are often associated with methods relying on X-ray radiation which can cause long-term effects on both the patient and the clinical staff.

To remove the need for imaging techniques, this work's main objective consisted of stopping autonomously bone drillings when reaching the bone interface thanks to real-time conductivity measurements embedded in the surgical instruments. A bone breach detection algorithm has been developed to detect a change of bone medium during a pedicle preparation. The stopping criteria and parameters were identified from conductivity and robot measurements gathered during bone breaches performed on *ex-vivo* lamb vertebrae. The tuned algorithm then allowed the drilling instrument to stop close to the bone interface (with an average of 0.65mm and a standard deviation of 0.4mm) on a set of 104 lamb vertebrae. The same algorithm was then tested *in-vivo* on pig surgery to validate the setup in actual operative conditions. Two drillings were used to adapt the tuning parameters, then the algorithm allowed to stop successfully the four other drillings performed on the lumbar vertebrae of the animal.

To reach this goal, a cooperative robotic setup comprising a medically graded robotic manipulator (KUKA LBR Med 7) has been developed throughout the thesis. A home-made velocity-controlled power drill was conceived at the ISIR laboratory to be able to perform drilling and screwing tasks while measuring the required motor torque. Moreover, drill bits embedding a bipolar conductivity sensor were especially prototyped at the SpineGuard company for the purpose of this work.

Moreover, to cope with the motion induced by the breathing of the patient and the deformability of the human body, a lot of effort has been put into creating a robust force controller that could be safe to use in surgical robotics applications. An innovative approach has been proposed by using pseudo-force feedback (induced by an internal impedance controller) instead of the classical method seen in literature consisting in using the feedback from a force sensor. Experiments with various conditions (including *in-vivo* setup) demonstrate the method's robustness compared to the state-of-the-art.

5.2 Perspectives

Future work is required to turn this project into an actual medical product that could operate on human patients.

First of all, during this thesis, most of the drillings have been performed on the spinous process instead of on the pedicles to avoid potential growth cartilage (which is also very conductive) present in the *in-vivo* pig model. To come back to the real operative conditions, the breach detection algorithm would have to handle the high measurements at the growth cartilage to avoid false positive detection. Moreover, the algorithm has only been tested on animal models so far and will have to be adapted for application to human patients. The passive human bone conductivity data collection during scoliosis surgeries presented in [Saghbiny et al., 2022] needs to be continued to generate a significant database to reinforce the bone breach detection. Also, the FAROS European project will probably conduct some tests on cadavers during the scope of the project.

Many possibilities for improving the breach detection have been raised from the cooperative work with the FAROS consortium. To begin with, a multi-modal approach by using several different types of sensors could increase even more the robustness and accuracy of the detection. Primarily, we have seen in our work that the use of the cutting torque measurement seems promising and should be investigated further. Once several sensors have been considered individually, intelligent combinations of the sensors' signals through data fusion algorithms could combine the forces of each sensor type and reduce the number of false detections. In particular, state-of-the-art machine learning techniques could simplify associating the different sensor measurements.

Furthermore, we believe that the proposed breach detection based on electrical conductivity could be transferable to other surgeries, such as knee replacement or dental implantology, with proper adjustments to the robotics setup and tools.

Finally, we would like to investigate further the use of our hybrid position-force control architecture. One aspect that could be explored is the control of forces applied on an environment that deforms non-isotropically. This is a typical difficulty encountered by surgeons: due to the large drilling force, vertebrae are displaced, and their orientation change. The drilling direction is to be adapted accordingly in real-time. We could also explore other robotics applications. In the context of this project, the force controller could also be used to perform palpations or contact ultrasound scanning of the spine to register the model of the spine w.r.t to the robot's base. In industrial applications, our approach could also be used to perform polishing, sanding, or grinding tasks.

Appendices

Appendix A

Preliminary robotic setup

In the early stages of the thesis, a different robotic setup was used to collect the first *in-vivo* measurements and create the initial proof of concept. We used an AEG manual power drill off the shelf and a KUKA LWR IV+ robotic arm. Figure A.1 shows preliminary *in-vivo* setup used to collect the data of Figures 4.4 and 4.5 during our first pig lab. All the other drillings presented in this document were using the setup presented in Chapter 2.

FIGURE A.1: Setup used during the first pig lab to collect the data of Figure 4.5.

To control the commercial power drill from a computer, an Arduino board was used to regulate the power delivered to the drill's motor via a MOSFET. Moreover, a relay and a 25W dissipating resistor allowed to quickly stop the rotation of the motor. The circuit is shown on Figure A.2.

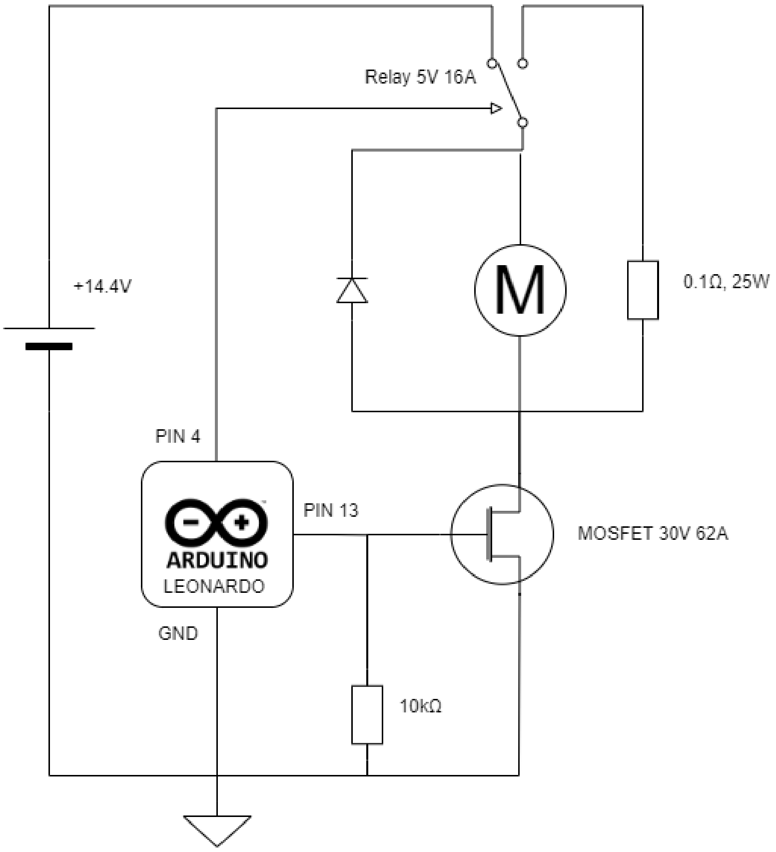

FIGURE A.2: Arduino-based electronic circuit used to control the power delivered to the power drill and its fast braking.

Appendix B

Power drill conception

Here we show the sketches and components' references necessary to reproduce entirely the power drill used in our robotic setup. Figure B.1 shows an exploded view of all the parts composing the power drill. Figures B.2, B.3, and B.4 present the sketches of the three plastic parts made with fast prototyping to protect the motor and its controller. Figures B.5, B.6, and B.7 show the sketches of the three aluminum parts created by Laurent FABRE, with the five-axis milling machine of the lab, to fix the instrument *w.r.t.* the robot's flange.

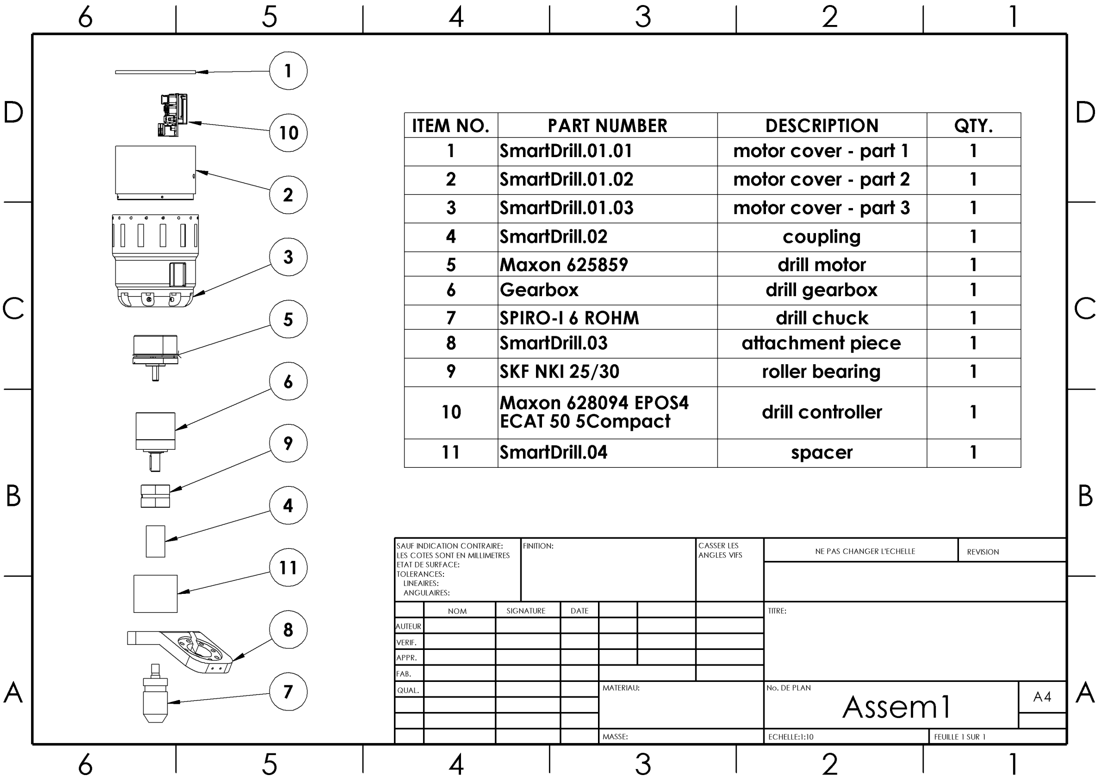

ITEM NO.	PART NUMBER	DESCRIPTION	QTY.
1	SmartDrill.01.01	motor cover - part 1	1
2	SmartDrill.01.02	motor cover - part 2	1
3	SmartDrill.01.03	motor cover - part 3	1
4	SmartDrill.02	coupling	1
5	Maxon 625859	drill motor	1
6	Gearbox	drill gearbox	1
7	SPIRO-I 6 ROHM	drill chuck	1
8	SmartDrill.03	attachment piece	1
9	SKF NKI 25/30	roller bearing	1
10	Maxon 628094 EPOS4 ECAT 50 5Compact	drill controller	1
11	SmartDrill.04	spacer	1

FIGURE B.1: Exploded view of the homemade power drill.

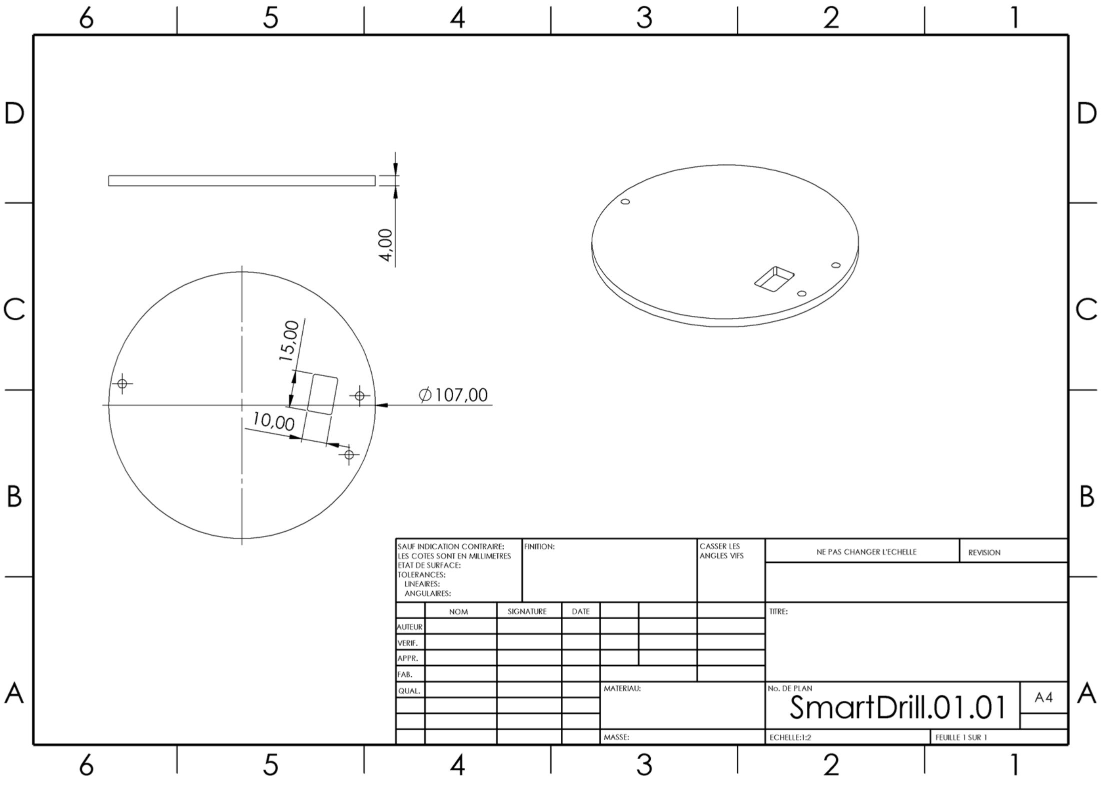

Figure B.2: Motor cover, part 1.

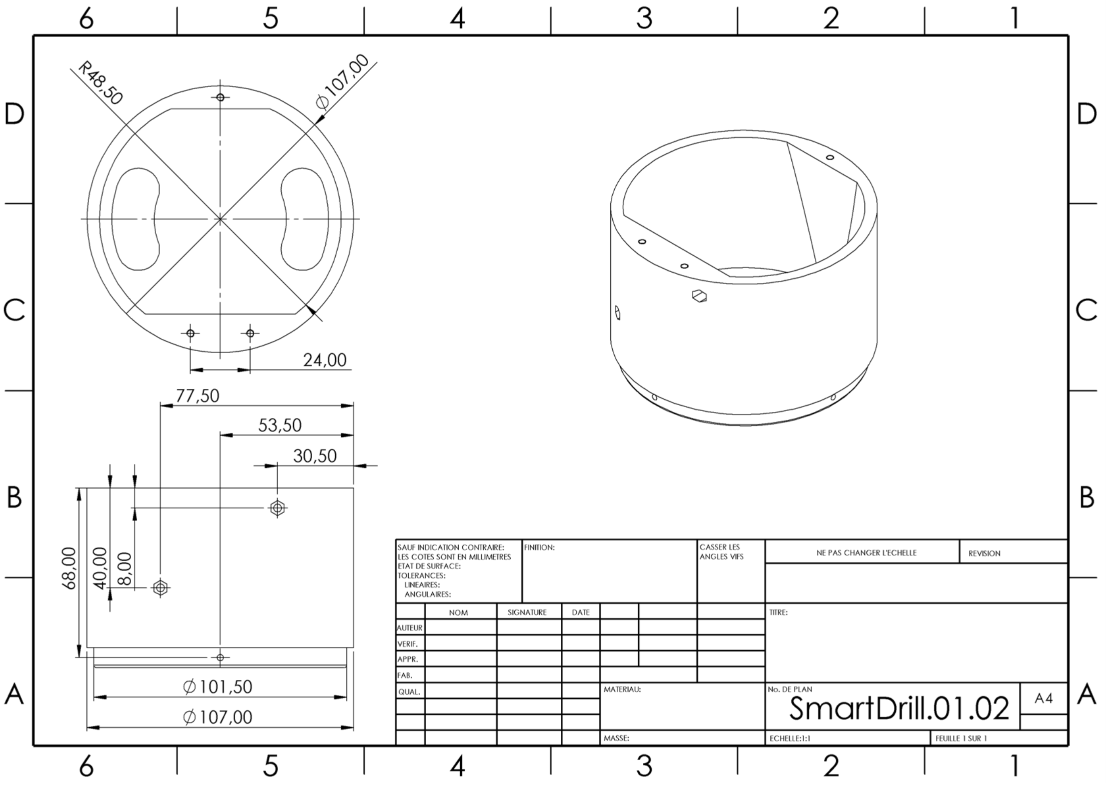

Figure B.3: Motor cover, part 2.

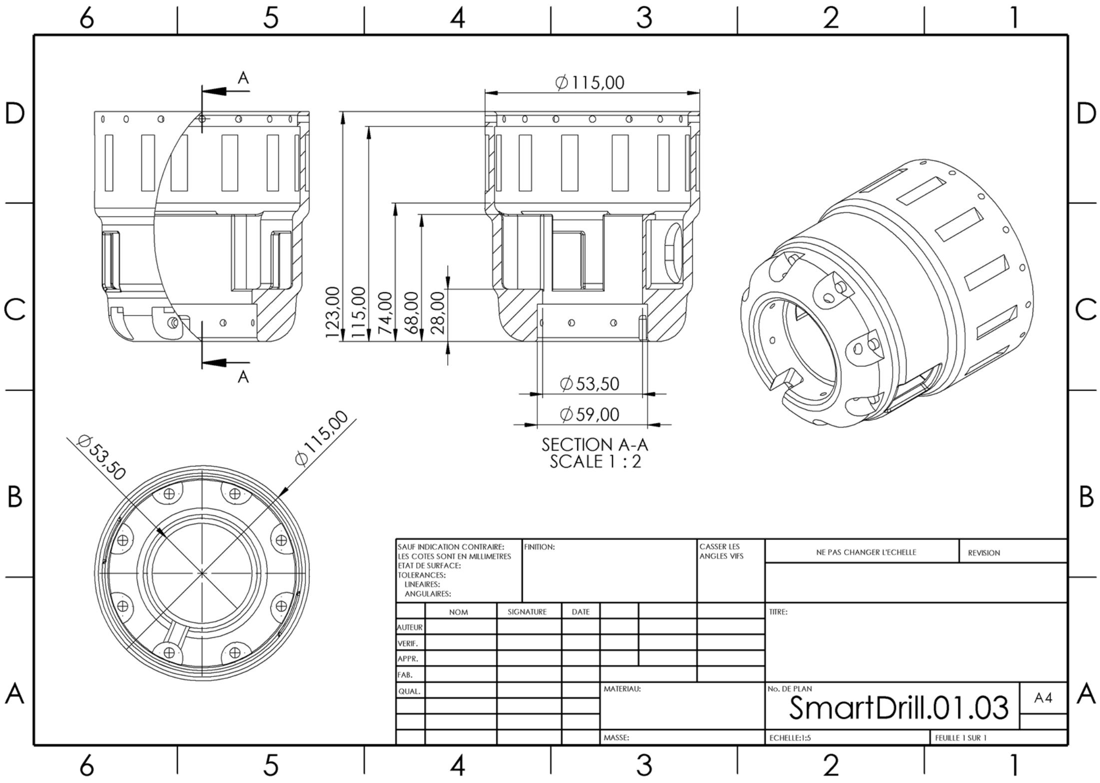

Figure B.4: Motor cover, part 3.

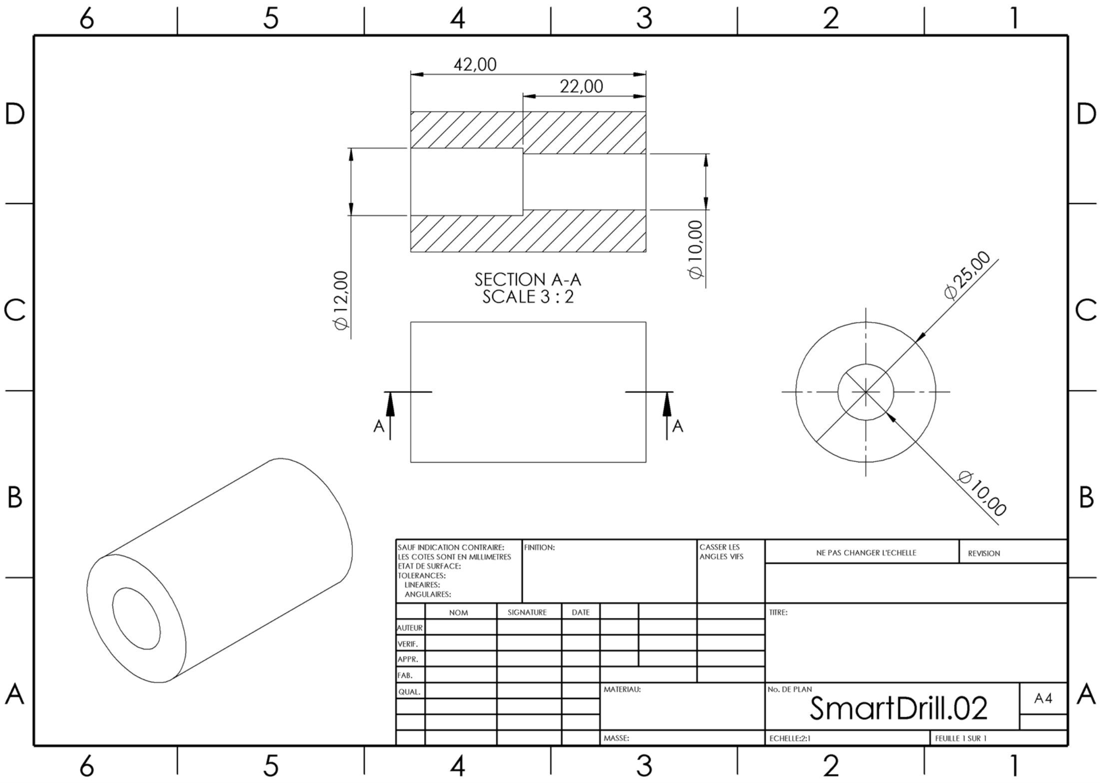

Figure B.5: Coupling of the gearbox's and the chuck's axes.

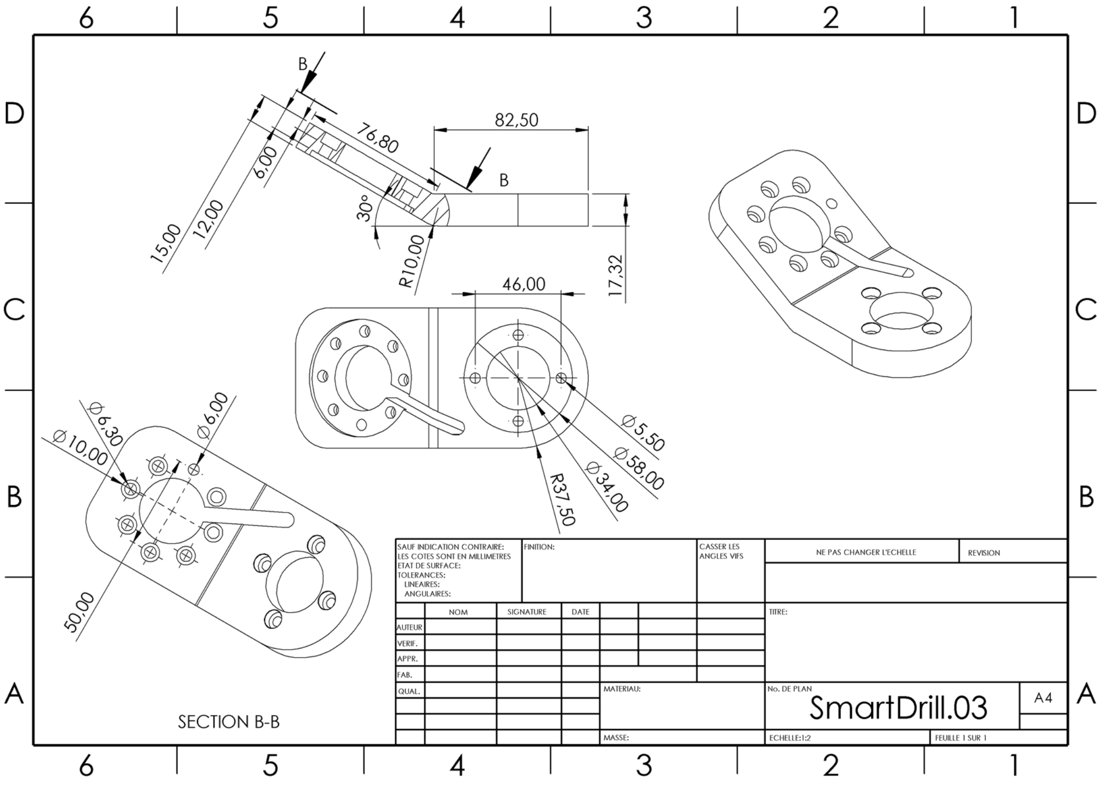

Figure B.6: Attachment piece to the KUKA robot's flange.

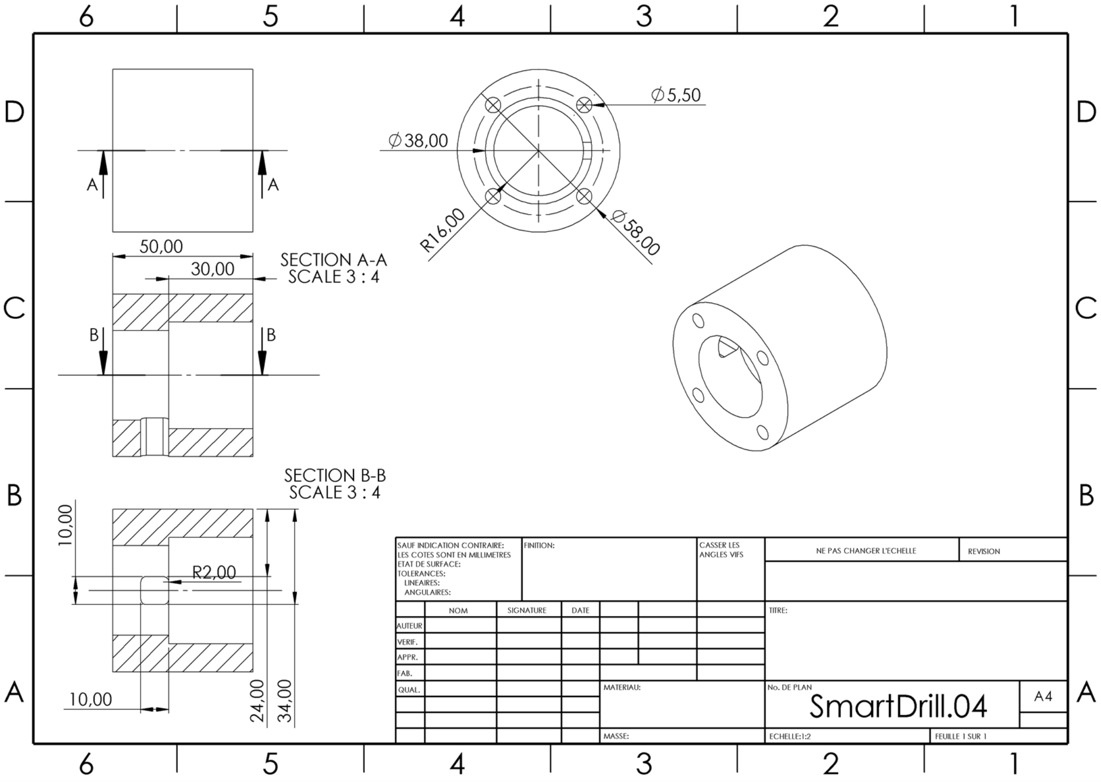

Figure B.7: Vertical spacer.

Appendix C

Ethical approval

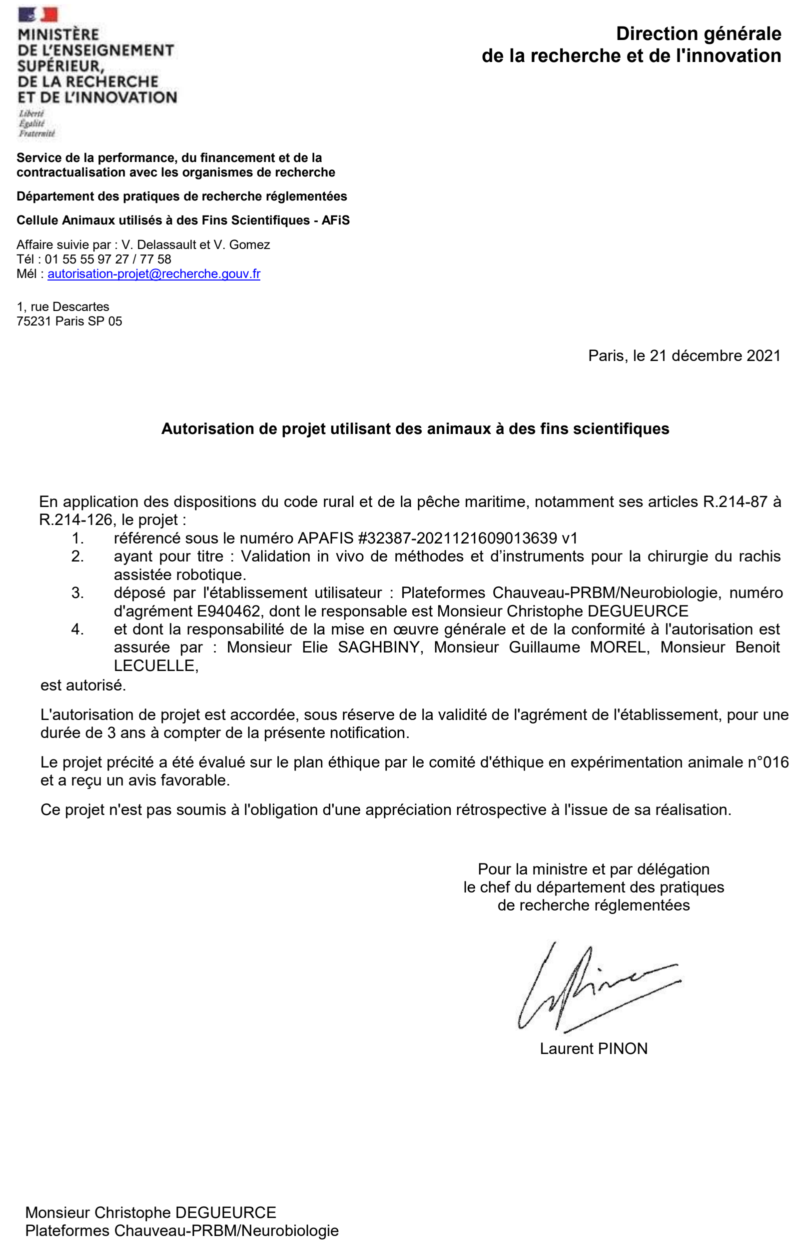

MINISTÈRE
DE L'ENSEIGNEMENT
SUPÉRIEUR,
DE LA RECHERCHE
ET DE L'INNOVATION
Liberté
Égalité
Fraternité

Direction générale
de la recherche et de l'innovation

Service de la performance, du financement et de la contractualisation avec les organismes de recherche

Département des pratiques de recherche réglementées

Cellule Animaux utilisés à des Fins Scientifiques - AFiS

Affaire suivie par : V. Delassault et V. Gomez
Tél : 01 55 55 97 27 / 77 58
Mél : autorisation-projet@recherche.gouv.fr

1, rue Descartes
75231 Paris SP 05

Paris, le 21 décembre 2021

Autorisation de projet utilisant des animaux à des fins scientifiques

En application des dispositions du code rural et de la pêche maritime, notamment ses articles R.214-87 à R.214-126, le projet :

1. référencé sous le numéro APAFIS #32387-2021121609013639 v1
2. ayant pour titre : Validation in vivo de méthodes et d'instruments pour la chirurgie du rachis assistée robotique.
3. déposé par l'établissement utilisateur : Plateformes Chauveau-PRBM/Neurobiologie, numéro d'agrément E940462, dont le responsable est Monsieur Christophe DEGUEURCE
4. et dont la responsabilité de la mise en œuvre générale et de la conformité à l'autorisation est assurée par : Monsieur Elie SAGHBINY, Monsieur Guillaume MOREL, Monsieur Benoit LECUELLE,

est autorisé.

L'autorisation de projet est accordée, sous réserve de la validité de l'agrément de l'établissement, pour une durée de 3 ans à compter de la présente notification.

Le projet précité a été évalué sur le plan éthique par le comité d'éthique en expérimentation animale n°016 et a reçu un avis favorable.

Ce projet n'est pas soumis à l'obligation d'une appréciation rétrospective à l'issue de sa réalisation.

Pour le ministre et par délégation
le chef du département des pratiques
de recherche réglementées

Laurent PINON

Monsieur Christophe DEGUEURCE
Plateformes Chauveau-PRBM/Neurobiologie

Appendix D

Breathing registration

We have seen in Chapter 4 that the measurement of the insertion depth in the bone can be helpful in the breach detection algorithm. The difficulty of getting this measurement relies on the fact that, except for bones, the patient's anatomy can be deformed during the drilling process. By applying a constant force on the patient, *e.g.* with our pseudo-force controller, most of the deformation is induced by the breathing of the patient, and almost periodic. This breathing profile can be identified in order to retrieve an estimation of the depth of insertion in the bone.

The breathing time period can, for instance, be identified thanks to a Fast Fourier Transform or auto-correlation functions, or simply recovered from the configuration of the breathing machine used in the OR. A quick calibration phase, where the robot applies a constant force at the entry-point, can then allow to identify the mean breathing profile before performing the drilling, like shown in Figure D.1.

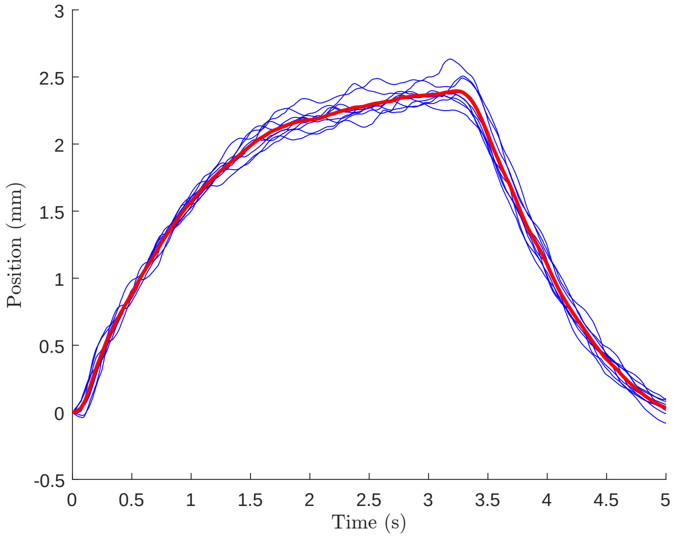

FIGURE D.1: Mean (in red) of ten breathing motions (in blue) measured by applying a constant 10N force on an *in-vivo* pig model on level L1.

Then, during the drilling procedure, this profile can be subtracted from the robot's displacement to estimate the insertion depth in real-time. Figure D.2 shows the results on one of the validation *in-vivo* experiments (cf. Figure 4.18). The breathing profile and the current robot measurements can be re-synchronized in live thanks with cross-correlation in case of drifting.

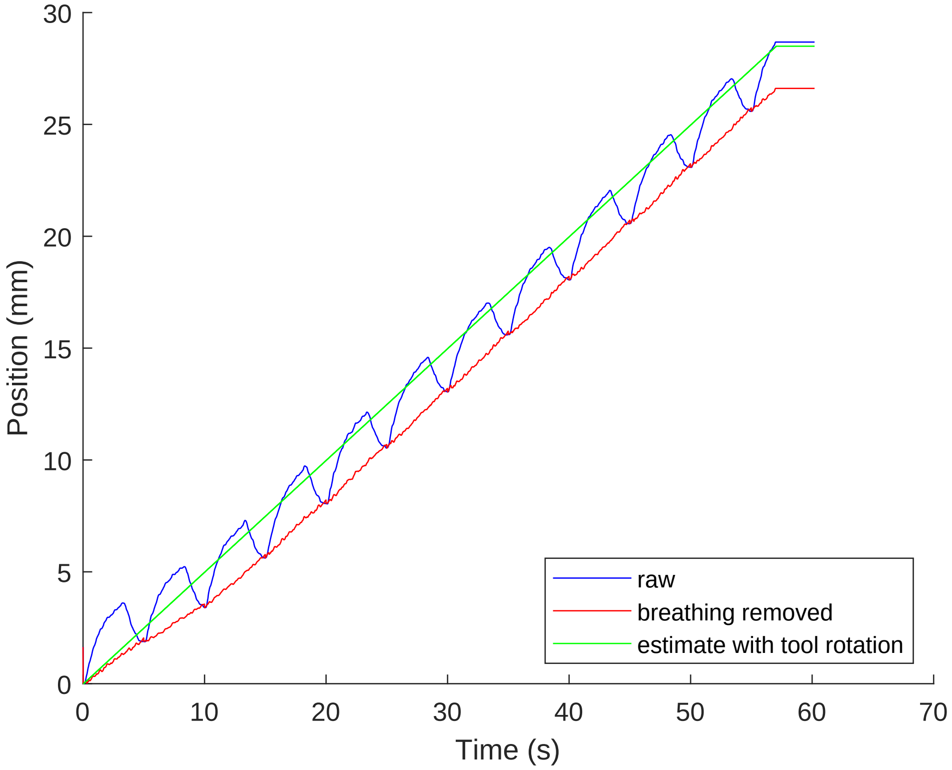

FIGURE D.2: Estimation of the depth of insertion in the bone from the robot's displacement with two different methods on the plots of Figure 4.18. In green, with the rotation of the threaded instrument. In red, with the calibration of the breathing motion profile.

This method provides a better estimate than by using the rotation speed of the drill. Moreover, by comparing the two approaches, we can detect when the threads of the drilling instrument are correctly anchored in the vertebra.

Appendix E

Final *in-vivo* results

Figures E.1 and E.2 show respectively the CT scans and the data collected during the final *in-vivo* tests of Algorithm 3, similarly to Figure 4.18. On the scans of L2 and L3, a screw is visible in one of the pedicle; this was part of a later experiment for the FAROS project.

(A) L1

(B) L2

(C) L3

(D) L4

FIGURE E.1: Post-operative CT scans of the pig vertebrae drilled *in-vivo* with the threaded drill bit and automatically stopped thanks to Algorithm 3.

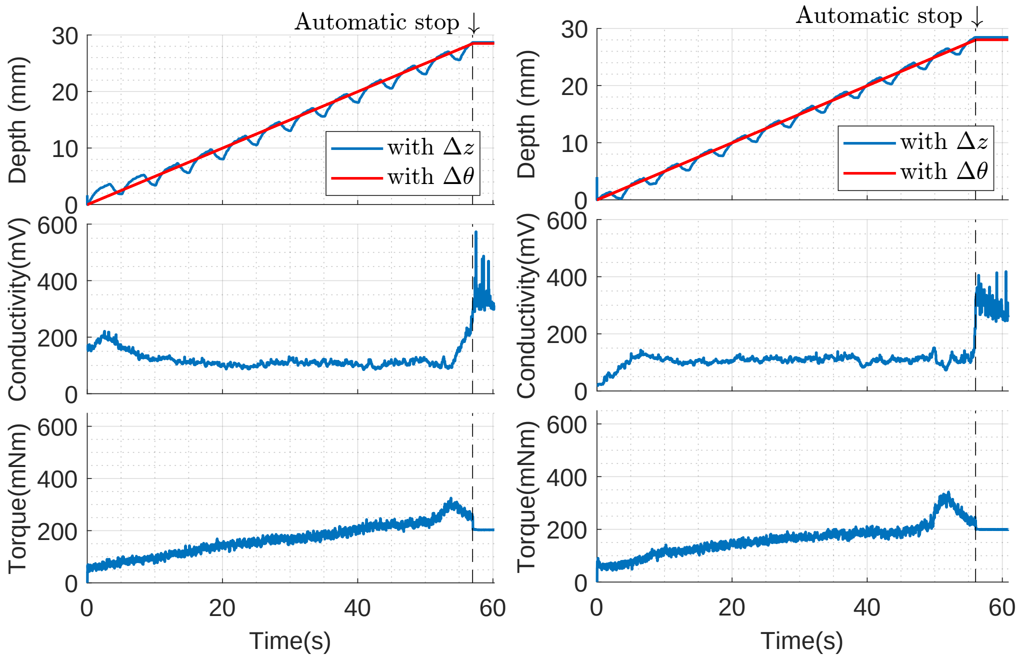

(A) L1 (B) L2

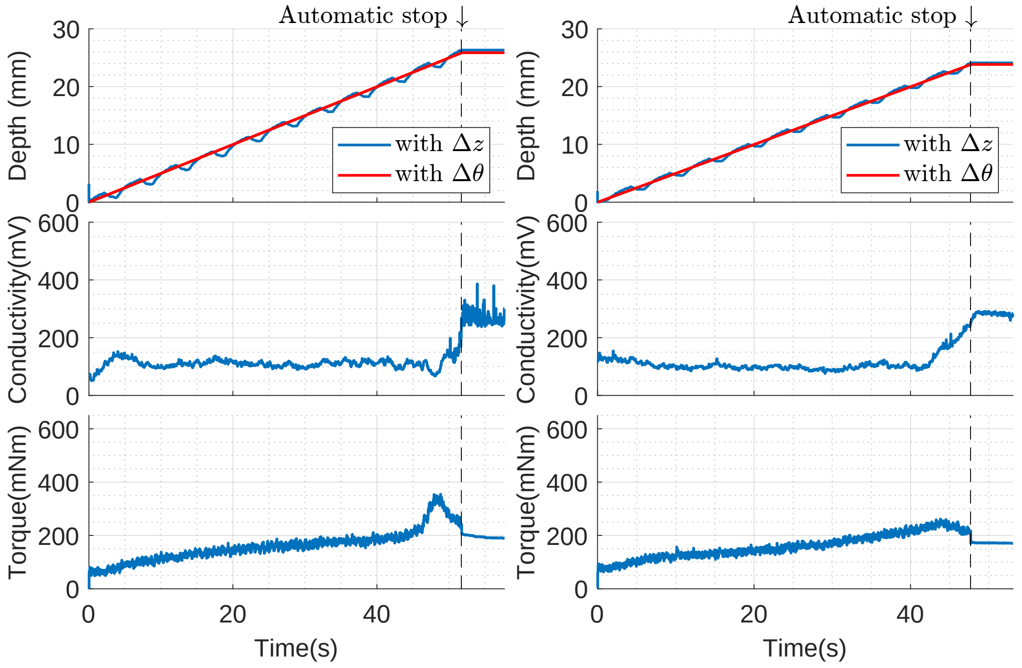

(C) L3 (D) L4

FIGURE E.2: Real-time measured *in-vivo* pig data during drillings performed with the threaded drill bit prototype and automatically stopped with Algorithm 3.

References

Abul-Kasim, K. and Ohlin, A. (2011). The rate of screw misplacement in segmental pedicle screw fixation in adolescent idiopathic scoliosis. *Acta Orthop.*, 82(1):50–55. *Cited page 7*

Accini, F., Díaz, I., and Gil, J. J. (2016). Using an admittance algorithm for bone drilling procedures. *Comput. Methods Programs Biomed.*, 123:150–158. *Cited page 12*

Ahmed, A. S., Ramakrishnan, R., Ramachandran, V., Ramachandran, S. S., Phan, K., and Antonsen, E. L. (2018). Ultrasound diagnosis and therapeutic intervention in the spine. *J. Spine Surg.*, 4(2):423–432. *Cited page 8*

Albu-Schäffer, A., Haddadin, S., Ott, C., Stemmer, A., Wimböck, T., and Hirzinger, G. (2007). The DLR lightweight robot: design and control concepts for robots in human environments. *Ind. Robot*, 34:376–385. *2 citations page 23 and 35*

Alcocer, A., Robertsson, A., Valera, A., and Johansson, R. (2003). Force estimation and control in robot manipulators. *IFAC Proceedings Volumes*, 36(17):55–60. 7th IFAC Symposium on Robot Control (SYROCO 2003), Wroclaw, Poland, 1-3 September, 2003. *Cited page 43*

Allaoui, M., Zairi, F., Tétard, M.-C., Gaughan, J., Chopin, D., and Assaker, R. (2018). Contribution of Dynamic Surgical Guidance to the Accurate Placement of Pedicle Screws in Deformity Surgery: A Retrospective Case Series. *World Neurosurg.*, 120:e466–e471. *Cited page 17*

Allotta, B., Belmonte, F., Bosio, L., and Dario, P. (1996). Study on a mechatronic tool for drilling in the osteosynthesis of long bones: Tool/bone interaction, modeling and experiments. *Mechatronics*, 6(4):447–459. *Cited page 12*

Almeida, F., Lopes, A., and Abreu, P. (1999). Force-impedance control: a new control strategy of robotic manipulators. *Recent advances in Mechatronics*, 1:126–137. *3 citations page 37, 38, and 40*

An, C. H. and Hollerbach, J. M. (1987). Dynamic stability issues in force control of manipulators. In *1987 American Control Conference*, pages 821–827. IEEE. *Cited page 41*

Arico, M. (2020). *Robotic Comanipulation as a Tangible Interface for Assistance to Laparoscopic Surgery*. PhD thesis, Sorbonne université. *Cited page 11*

Balmer, T. W., Vesztergom, S., Broekmann, P., Stahel, A., and Büchler, P. (2018). Characterization of the electrical conductivity of bone and its correlation to osseous structure. *Sci. Rep.*, 8(1):8601. *Cited page 15*

Betz, R., Bolger, C., and George, K. (2010). PediGuard®: for safer pedicle screw placement. *ArgoSpine News J.*, 22(4):149–152. *Cited page 15*

Bolger, C. and Bourlion, M. (2005). Pedicle navigation in spondylolisthesis. In *Spondylolysis, spondylolisthesis, and degenerative spondylolisthesis*, pages 227–237. Lippincott Williams & Wilkins Philadelphia. *Cited page 75*

Bolger, C., Kelleher, M. O., McEvoy, L., Brayda-Bruno, M., Kaelin, A., Lazennec, J. Y., Le Huec, J. C., Logroscino, C., Mata, P., Moreta, P., Saillant, G., and Zeller, R. (2007). Electrical conductivity measurement: a new technique to detect iatrogenic initial pedicle perforation. *Eur. Spine J.*, 16(11):1919–1924. *2 citations page 15 and 17*

Borghesan, G., Willaert, B., and De Schutter, J. (2012). A constraint-based programming approach to physical human-robot interaction. In *2012 IEEE International Conference on Robotics and Automation*, pages 3890–3896. *2 citations page 43 and 71*

Bourlion, M., Frezal, O., Morel, G., Bette, S., Chandanson, T., Richer, F., and Kerspern, V. (2021). Robotic surgical system. U.S. Patent 20210282862, May 28, 2021. *Cited page 18*

Bourlion, M. and Vanquaethem, A. (2003). Device for monitoring the penetration of an instrument into an anatomical structure. U.S. Patent 20050119660, Feb 11, 2003. *Cited page 15*

Bratschitsch, G., Leitner, L., Stücklschweiger, G., Guss, H., Sadoghi, P., Puchwein, P., Leithner, A., and Radl, R. (2019). Radiation Exposure of Patient and Operating Room Personnel by Fluoroscopy and Navigation during Spinal Surgery. *Sci. Rep.*, 9(1):17652. *Cited page 8*

Burström, G., Swamy, A., Spliethoff, J. W., Reich, C., Babic, D., Hendriks, B. H. W., Skulason, H., Persson, O., Elmi Terander, A., and Edström, E. (2019). Diffuse reflectance spectroscopy accurately identifies the pre-cortical zone to avoid impending pedicle screw breach in spinal fixation surgery. *Biomed. Opt. Express*, 10(11):5905. *2 citations page 14 and 17*

Busscher, I., Ploegmakers, J. J. W., Verkerke, G. J., and Veldhuizen, A. G. (2010). Comparative anatomical dimensions of the complete human and porcine spine. *Eur. Spine J.*, 19(7):1104–1114. *Cited page 29*

Chaput, C. D., George, K., Samdani, A. F., Williams, J. I., Gaughan, J., and Betz, R. R. (2013). Reduction in radiation (fluoroscopy) while maintaining safe placement of pedicle screws during lumbar spine fusion. *Coluna/Columna*, 12(2):138–141. *Cited page 17*

Chen, S.-F. (2003). The 6×6 stiffness formulation and transformation of serial manipulators via the cct theory. In *2003 IEEE International Conference on Robotics and Automation (Cat. No. 03CH37422)*, volume 3, pages 4042–4047. IEEE. *Cited page 56*

Chen, S.-F. and Kao, I. (2000). Conservative congruence transformation for joint and cartesian stiffness matrices of robotic hands and fingers. *The International Journal of Robotics Research*, 19(9):835–847. *Cited page 56*

Crawford, N., Johnson, N., and Theodore, N. (2020). Ensuring navigation integrity using robotics in spine surgery. *J. Robot. Surg.*, 14(1):177–183. *Cited page 74*

Da Silva, J., Chandanson, T., and Morel, G. (2019). Robot-assisted spine surgery guided by conductivity sensing: first preclinical experiments demonstrate X-ray free breach detection. In *Hamlyn Symp. Med. Robot.*, pages 75–76. The Hamlyn Centre, Faculty of Engineering, Imperial College London. *Cited page 21*

Da Silva, J., Saghbiny, E., Chandanson, T., Bette, S., Bourlion, M., Assaker, R., Betz, R., Bolger, C., Defino, H., Kaelin, A., Khoo, L. T., Williams, J., Wong, H. K., and Morel, G. (2021). Using electrical conductivity for breach prevention during automatic bone drilling. In *Annual Forum '21 – Society for Minimally Invasive Spine Surgery (SMISS)*. *Cited page 21*

Da Silva, J., Saghbiny, E., Chandanson, T., Bette, S., Bourlion, M., and Morel, G. (2022a). Automatic bone breach detection for spine surgery based on bio-electrical conductivity sensing : Ex-vivo experimental validation. In *11th Conference on New Technologies for Computer and Robot Assisted Surgery (CRAS)*, pages 86–87. *Cited page 21*

Da Silva, J., Vafadar, S., Chandanson, T., and Morel, G. (2022b). Force control of the KUKA LBR Med without external force sensor. In *11th Conference on New Technologies for Computer and Robot Assisted Surgery (CRAS)*, pages 88–89. *Cited page 21*

Erickson, D., Weber, M., and Sharf, I. (2003). Contact stiffness and damping estimation for robotic systems. *The International Journal of Robotics Research*, 22(1):41–57. *Cited page 37*

Espejo, M. P. (2006). Free Hand Pedicle Screw Placement in the Thoracic Spine: Is It Safe? *Yearb. Neurol. Neurosurg.*, 2006(3):295–296. *Cited page 5*

F. McLain, R., Yerby, S. A., and Moseley, T. A. (2002). Comparative Morphometry of L4 Vertebrae. *Spine (Phila. Pa. 1976).*, 27(8):E200–E206. *Cited page 29*

Farber, S. H., Pacult, M. A., Godzik, J., Walker, C. T., Turner, J. D., Porter, R. W., and Uribe, J. S. (2021). Robotics in spine surgery: A technical overview and review of key concepts. *Frontiers in Surgery*, 8:24. *2 citations page ix and 10*

Feng, W., Wang, W., Chen, S., Wu, K., and Wang, H. (2020). O-arm navigation versus C-arm guidance for pedicle screw placement in spine surgery: a systematic review and meta-analysis. *Int. Orthop.*, 44(5):919–926. *Cited page 7*

Ferraguti, F., Secchi, C., and Fantuzzi, C. (2013). A tank-based approach to impedance control with variable stiffness. In *2013 IEEE Int. Conf. Robot. Autom.*, pages 4948–4953. IEEE. *Cited page 38*

Galetta, M. S., Leider, J. D., Divi, S. N., Goyal, D. K. C., and Schroeder, G. D. (2019). Robotics in spinal surgery. *Ann. Transl. Med.*, 7(S5):S165–S165. *Cited page 18*

Gertzbein, S. D. et al. (1990). Accuracy of Pedicular Screw Placement In Vivo. *Spine (Phila. Pa. 1976).*, 15(1):11–14. *Cited page 86*

Hacksel, P. and Salcudean, S. (1994). Estimation of environment forces and rigid-body velocities using observers. In *Proceedings of the 1994 IEEE International Conference on Robotics and Automation*, pages 931–936 vol.2. *Cited page 43*

Haddadin, S. and Croft, E. (2016). Physical Human–Robot Interaction. In *Springer Handb. Robot.*, pages 1835–1874. Springer International Publishing, Cham. *Cited page 34*

Ho, D., Li, T., and Meng, Q. H. (2018). Bone drilling breakthrough detection via energy-based signal. In *2018 40th Annual International Conference of the IEEE Engineering in Medicine and Biology Society (EMBC)*, pages 1809–1812. *Cited page 13*

Hogan, N. (1984). Impedance Control: An Approach to Manipulation. In *1984 Am. Control Conf.*, pages 304–313. IEEE. *Cited page 35*

Hogan, N. (1985). Impedance Control: An Approach to Manipulation: Part II—Implementation. *J. Dyn. Syst. Meas. Control*, 107(1):8–16. *Cited page 37*

Jung, S., Hsia, T., and Bonitz, R. (2004). Force Tracking Impedance Control of Robot Manipulators Under Unknown Environment. *IEEE Trans. Control Syst. Technol.*, 12(3):474–483. *Cited page 38*

Kalidindi, K. K. V., kumar Sharma, J., Jagadeesh, N. H., Sath, S., and Chhabra, H. S. (2020). Robotic spine surgery: a review of the present status. *J. Med. Eng. Technol.*, 44(7):431–437. *Cited page 18*

Kantelhardt, S., Amr, N., and Giese, A. (2014). Navigation and robot-aided surgery in the spine: historical review and state of the art. *Robot. Surg. Res. Rev.*, page 19. *2 citations page ix and 9*

Karami, K. J., Buckenmeyer, L. E., Kiapour, A. M., Kelkar, P. S., Goel, V. K., Demetropoulos, C. K., and Soo, T. M. (2015). Biomechanical evaluation of the pedicle screw insertion depth effect on screw stability under cyclic loading and subsequent pullout. *Clinical Spine Surgery*, 28(3):E133–E139. *Cited page 4*

Kelley, B. V., Hsiue, P. P., Upfill-Brown, A. M., Chen, C. J., Villalpando, C., Lord, E. L., Shamie, A. N., Stavrakis, A. I., and Park, D. Y. (2021). Utilization trends and outcomes of computer-assisted navigation in spine fusion in the united states. *The Spine Journal*, 21(8):1246–1255. *Cited page 9*

Khalsa, S. S. S., Mummaneni, P. V., Chou, D., and Park, P. (2021). Present and Future Spinal Robotic and Enabling Technologies. *Oper. Neurosurg. (Hagerstown, Md.)*, 21:undefined–undefined. *Cited page 7*

Khatib, O. (1987). A unified approach for motion and force control of robot manipulators: The operational space formulation. *IEEE J. Robot. Autom.*, 3(1):43–53. *Cited page 36*

Kochanski, R. B., Lombardi, J. M., Laratta, J. L., Lehman, R. A., and O'Toole, J. E. (2019). Image-Guided Navigation and Robotics in Spine Surgery. *Neurosurgery*, 84(6):1179–1189. *2 citations page ix and 9*

Komati, B., Clévy, C., and Lutz, P. (2014). Force tracking impedance control with unknown environment at the microscale. In *2014 IEEE International Conference on Robotics and Automation (ICRA)*, pages 5203–5208. IEEE. *Cited page 37*

Kronander, K. and Billard, A. (2016). Stability Considerations for Variable Impedance Control. *IEEE Trans. Robot.*, 32(5):1298–1305. *Cited page 38*

Kuo, Y.-L., Huang, S.-Y., and Lan, C.-C. (2019). Sensorless force control of automated grinding/deburring using an adjustable force regulation mechanism. In *2019 International Conference on Robotics and Automation (ICRA)*, pages 9489–9495. IEEE. *Cited page 38*

Lasky, T. A. and Hsia, T. C. (1991). On force-tracking impedance control of robot manipulators. *Proc. - IEEE Int. Conf. Robot. Autom.*, 1(April):274–280. *3 citations page 37, 38, and 40*

Li, R., Cai, Y., Niu, K., and Vander Poorten, E. (2021). Comparative quantitative analysis of robotic ultrasound image calibration methods. In *20th International Conference on Advanced Robotics (ICAR)*. *Cited page 8*

Lien, S.-B., Liou, N.-H., and Wu, S.-S. (2007). Analysis of anatomic morphometry of the pedicles and the safe zone for through-pedicle procedures in the thoracic and lumbar spine. *Eur. Spine J.*, 16(8):1215–1222. *Cited page 4*

Liu, D. and Michel, A. N. (1992). Asymptotic stability of discrete-time systems with saturation nonlinearities with applications to digital filters. *IEEE Transactions on Circuits and Systems I: Fundamental Theory and Applications*, 39(10):798–807. *Cited page 52*

Liu, H., Wang, Y., Pi, B., Qian, Z., Zhu, X., and Yang, H. (2017). Comparison of intraoperative o-arm- and conventional fluoroscopy (c-arm)-assisted insertion of pedicle screws in the treatment of fracture of thoracic vertebrae. *Journal of Orthopaedic Surgery*, 25(1):2309499016684090. *Cited page 7*

Liu, Y., Zeng, C., Fan, M., Hu, L., Ma, C., and Tian, W. (2016). Assessment of respiration-induced vertebral motion in prone-positioned patients during general anaesthesia. *Int. J. Med. Robot. Comput. Assist. Surg.*, 12(2):214–218. *Cited page 11*

Liégois, A. (1977). Automatic supervisory control of the configuration and behavior of multibody mechanisms. *IEEE Transactions on Systems, Man, and Cybernetics*, 7(12):868–871. *Cited page 48*

Lonstein, J. E., Denis, F., Perra, J. H., Pinto, M. R., Smith, M. D., and Winter, R. B. (1999). Complications associated with pedicle screws. *J. Bone Joint Surg. Am.*, 81(11):1519–28. *Cited page 4*

Mageed, M., Berner, D., Jülke, H., Hohaus, C., Brehm, W., and Gerlach, K. (2013). Is sheep lumbar spine a suitable alternative model for human spinal researches? Morphometrical comparison study. *Lab. Anim. Res.*, 29(4):183. *Cited page 29*

Mason, M. T. (1981). Compliance and force control for computer controlled manipulators. *IEEE Transactions on Systems, Man, and Cybernetics*, 11(6):418–432. *Cited page 47*

Müller, F., Roner, S., Liebmann, F., Spirig, J. M., Fürnstahl, P., and Farshad, M. (2020). Augmented reality navigation for spinal pedicle screw instrumentation using intraoperative 3d imaging. *The Spine Journal*, 20(4):621–628. *Cited page 8*

Ott, C. (2012). Cartesian Impedance Control: The Rigid Body Case. In *Cartes. Impedance Control Redundant Flexible-Joint Robot.*, volume 83 STAR, pages 29–44. Springer Berlin Heidelberg, Berlin, Heidelberg. *2 citations page 36 and 37*

Penrose, R. (1955). A generalized inverse for matrices. *Mathematical Proceedings of the Cambridge Philosophical Society*, 51(3):406–413. *Cited page 46*

Perdereau, V. and Drouin, M. (1993). A new scheme for hybrid force-position control. *Robotica*, 11(5):453–464. *Cited page 47*

Pithwa, Y. K. and Venkatesh, K. (2014). Prospective comparative study between straight and curved probe for pedicle screw insertion. *Eur. Spine J.*, 23(10):2161–2165. *Cited page 5*

Raibert, M. H. and Craig, J. J. (1981). Hybrid position/force control of manipulators. *J. Dyn. Syst. Meas. Control. Trans. ASME.* *Cited page 47*

Rawicki, N., Dowdell, J. E., and Sandhu, H. S. (2021). Current state of navigation in spine surgery. *Ann. Transl. Med.*, 9(1):85–85. *Cited page 9*

Roveda, L. and Piga, D. (2021). Sensorless environment stiffness and interaction force estimation for impedance control tuning in robotized interaction tasks. *Autonomous Robots*, 45(3):371–388. *Cited page 38*

Saghbiny, E., Da Silva, J., Chaimi, C., Chandanson, T., Morel, G., and Vialle, R. (2022). Toward automatic bone breach detection for spine surgery using tissue bio-electrical conductivity sensing. In *11th Conference on New Technologies for Computer and Robot Assisted Surgery (CRAS)*, pages 94–95. *3 citations page 21, 94, and 99*

Sans Merce, M., Pitteloud, N., and Savoye, F. (2020). Dose comparative study between two different 3d mobile intra-operative systems. *Radioprotection*, 55(3):179–185. *Cited page 7*

Sautot, P., Cinquin, P., Lavallée, S., and Troccaz, J. (1992). Computer assisted spine surgery: A first step toward clinical, application in orthopaedics. In *1992 14th Annual International Conference of the IEEE Engineering in Medicine and Biology Society*, volume 3, pages 1071–1072. *Cited page 1*

Seibold, M., Maurer, S., Hoch, A., Zingg, P., Farshad, M., Navab, N., and Fürnstahl, P. (2021). Real-time acoustic sensing and artificial intelligence for error prevention in orthopedic surgery. *Sci. Rep.*, 11(1):3993. *2 citations page 14 and 17*

Seraji, H. and Colbaugh, R. (1997). Force tracking in impedance control. *The International Journal of Robotics Research*, 16(1):97–117. *2 citations page 37 and 41*

Sheng, S.-R., Wang, X.-Y., Xu, H.-Z., Zhu, G.-Q., and Zhou, Y.-F. (2010). Anatomy of large animal spines and its comparison to the human spine: a systematic review. *Eur. Spine J.*, 19(1):46–56. *Cited page 29*

Shweikeh, F., Amadio, J. P., Arnell, M., Barnard, Z. R., Kim, T. T., Johnson, J. P., and Drazin, D. (2014). Robotics and the spine: a review of current and ongoing applications. *Neurosurg. Focus FOC*, 36(3):E10. *Cited page 7*

Siciliano, B. and Khatib, O., editors (2008). *Springer Handbook of Robotics*. Springer Berlin Heidelberg, Berlin, Heidelberg. *Cited page 34*

Solitro, G. F., Whitlock, K., Amirouche, F., Mehta, A. I., and McDonnell, A. (2019). Currently adopted criteria for pedicle screw diameter selection. *International Journal of Spine Surgery*, 13(2):132–145. *Cited page 4*

Song, P., Yu, Y., and Zhang, X. (2019). A Tutorial Survey and Comparison of Impedance Control on Robotic Manipulation. *Robotica*, 37(5):801–836. *Cited page 37*

Staartjes, V. E., Seevinck, P. R., Vandertop, W. P., van Stralen, M., and Schröder, M. L. (2021). Magnetic resonance imaging–based synthetic computed tomography of the lumbar spine for surgical planning: a clinical proof-of-concept. *Neurosurg. Focus*, 50(1):E13. *Cited page 8*

Stolt, A., Linderoth, M., Robertsson, A., and Johansson, R. (2012). Force controlled robotic assembly without a force sensor. In *2012 IEEE International Conference on Robotics and Automation*, pages 1538–1543. IEEE. *3 citations page 38, 43, and 71*

Suess, O. and Schomacher, M. (2016). Control of Pedicle Screw Placement with an Electrical Conductivity Measurement Device: Initial Evaluation in the Thoracic and Lumbar Spine. *Adv. Med.*, 2016:1–7. *Cited page 17*

Sui, J., Sugita, N., Ishii, K., Harada, K., and Mitsuishi, M. (2014). Mechanistic modeling of bone-drilling process with experimental validation. *J. Mater. Process. Technol.*, 214(4):1018–1026. *Cited page 12*

Sun, Y., Jin, H., Hu, Y., Zhang, P., and Zhang, J. (2014). State recognition of bone drilling with audio signal in Robotic Orthopedics Surgery System. *IEEE Int. Conf. Intell. Robot. Syst.*, pages 3503–3508. *Cited page 13*

Swamy, A., Spliethoff, J. W., Burström, G., Babic, D., Reich, C., Groen, J., Edström, E., Elmi-Terander, A., Racadio, J. M., Dankelman, J., and Hendriks, B. H. W. (2020). Diffuse reflectance spectroscopy for breach detection during pedicle screw placement: a first in vivo investigation in a porcine model. *Biomed. Eng. Online*, 19(1):47. *Cited page 14*

Thompson, J. C. (2010). *Netter's Concise Orthopaedic Anatomy, 2nd Ed.* Elsevier. *2 citations page ix and 3*

Tian, W., Han, X., Liu, B., Liu, Y., Hu, Y., Han, X., Xu, Y., Fan, M., and Jin, H. (2014). A robot-assisted surgical system using a force-image control method for pedicle screw insertion. *PLOS ONE*, 9(1):1–9. *2 citations page 12 and 18*

Torun, Y. and Öztürk, A. (2020). A New Breakthrough Detection Method for Bone Drilling in Robotic Orthopedic Surgery with Closed-Loop Control Approach. *Ann. Biomed. Eng.*, 48(4):1218–1229. *3 citations page ix, 13, and 17*

Torun, Y., Öztürk, A., HatİpoĞlu, N., and Öztemür, Z. (2018). Breakthrough detection for orthopedic bone drilling via power spectral density estimation of acoustic emission. In *2018 Electric Electronics, Computer Science, Biomedical Engineerings' Meeting (EBBT)*, pages 1–5. *Cited page 14*

Troccaz, J. (2013). *Medical Robotics*. John Wiley & Sons, Inc., Hoboken, NJ USA. *Cited page 2*

Vadalà, G., Ambrosio, L., Portaccio, I., Accoto, D., Russo, F., De Salvatore, S., Papalia, R., and Denaro, V. (2020). Validation of a novel smart drilling system to monitor bone impedance during transpedicular screw placement: a pilot study. In *Congress of the Italian Orthopaedic Research Society 2019 Guest Editors: F. Castoldi, GM Peretti, A. Marmotti, L. Mangiavini*, volume 34, page 251. *Cited page 12*

Vasudeva, V. S., Abd-El-Barr, M., Pompeu, Y. A., Karhade, A., Groff, M. W., and Lu, Y. (2017). Use of intraoperative ultrasound during spinal surgery. *Global Spine Journal*, 7(7):648–656. PMID: 28989844. *Cited page 8*

Villani, L. and De Schutter, J. (2016). Force Control. In *Springer Handb. Robot.*, pages 195–220. Springer International Publishing, Cham. *Cited page 34*

Wijayarathne, L. and Hammond, F. L. (2020). Identification of compliant contact parameters and admittance force modulation on a non-stationary compliant surface. In *2020 IEEE Int. Conf. Robot. Autom.*, pages 6826–6832. IEEE. *Cited page 34*

Wilfinger, L. S., Wen, J., and Murphy, S. H. (1994). Integral force control with robustness enhancement. *IEEE Control Systems Magazine*, 14(1):31–40. *Cited page 41*

Wilke, H.-J., Kettler, A., Wenger, K. H., and Claes, L. E. (1997). Anatomy of the sheep spine and its comparison to the human spine. *Anat. Rec.*, 247(4):542–555. *Cited page 29*

Williams, J., Samdani, A., Defino, H. L. A., George, K., Gaughan, J., and Betz, R. (2014). Anticipation of vertebral pedicle breach through dynamic surgical guidance. *Coluna/Columna*, 13(3):210–213. *Cited page 17*

Xu, W., Cai, C., Yin, M., and Zou, Y. (2012). Time-varying force tracking in impedance control. In *2012 IEEE 51st IEEE Conference on Decision and Control (CDC)*, pages 344–349. IEEE. *Cited page 37*

Zaffino, P., Moccia, S., De Momi, E., and Spadea, M. F. (2020). A review on advances in intra-operative imaging for surgery and therapy: Imagining the operating room of the future. *Annals of Biomedical Engineering*, pages 1–21. *Cited page 11*

Zakeri, V. and Hodgson, A. J. (2017). Classifying hard and soft bone tissues using drilling sounds. In *2017 39th Annual International Conference of the IEEE Engineering in Medicine and Biology Society (EMBC)*, pages 2855–2858. *Cited page 14*

Zettinig, O., Frisch, B., Virga, S., Esposito, M., Rienmüller, A., Meyer, B., Hennersperger, C., Ryang, Y.-M., and Navab, N. (2017). 3D ultrasound registration-based visual servoing for neurosurgical navigation. *Int. J. Comput. Assist. Radiol. Surg.*, 12(9):1607–1619. *Cited page 9*

Zhang, J., Wang, Y., Liu, T., Yang, K., and Jin, H. (2021). A Flexible Ultrasound Scanning System for Minimally Invasive Spinal Surgery Navigation. *IEEE Trans. Med. Robot. Bionics*, 3(2):426–435. *Cited page 11*

Zhou, G.-Q., Li, D.-S., Zhou, P., Jiang, W.-W., and Zheng, Y.-P. (2020). Automating spine curvature measurement in volumetric ultrasound via adaptive phase features. *Ultrasound in Medicine & Biology*, 46(3):828–841. *Cited page 8*